Indian Institute of Technology Guwahati

Optical Imaging Laboratory
Department of Physics
Indian Institute of Technology Guwahati

Effect of Aberrations on Tightly Focused Cylindrical Vector Beams

Md Gaffar

Thesis submitted in partial fulfilment of the requirements for the degree of Doctor of Philosophy of the Indian Institute of Technology Guwahati, Guwahati, India.

February 2016

TH-1501_10612103

Dedicated To My Beloved Parents

TH-1501_10612103

TH-1501_10612103

Declaration

Md Gaffar
Roll No. 10612103
Department of Physics
Indian Institute of Technology Guwahati
Guwahati, India

I hereby declare that the results embodied in this thesis is the result of theory and experiment carried out by me at the Department of Physics, Indian Institute of Technology Guwahati, Guwahati, India under the supervision of **Dr. Bosanta R. Boruah**. This thesis has not been submitted to any university/ institute or elsewhere for the award of any degree, diploma or associateship.

Md Gaffar

Date

TH-1501_10612103

TH-1501_10612103

Certificate

Dr. Bosanta R. Boruah
Associate Professor
Department of Physics
Indian Institute of Technology Guwahati
Guwahati, India
email:brboruah@iitg.ernet.in

This is to certify that the work contained in the thesis entitled **'Effect of aberrations on tightly focused cylindrical vector beams'** by **Mr. Md Gaffar** (Roll No. 10612103), a student of Department of Physics, Indian Institute of Technology Guwahati, for the award of degree of Doctor of Philosophy, has been carried out under my supervision.

The present thesis or any part thereof has not been submitted elsewhere for award of any other degree, diploma or associateship.

Dr. Bosanta R. Boruah

Date

TH-1501_10612103

TH-1501_10612103

Acknowledgements

I would like to thank my thesis supervisor Dr. Bosanta R. Boruah for his continuous support and help throughout my Ph.D. work. This work would have not been possible without his guidance, support and encouragement.

Then I would like to thank the rest of my doctoral committee members: Prof. Malay Kumar Nandy, Dr. Ashwini Kumar Sharma, Dr. Karuna Kalita for their encouragement, insightful comments, and suggestions.

My sincere thanks also goes to the former and present HoDs of Physics, Prof. Seenipandian Ravi and Prof. Saurabh Basu and Prof. Poulose Poulose for providing me the opportunity to utilize different resources of the department for my Ph.D. work.

Thanks to all the faculty members and entire staff of the department of Physics, who supported me in several situations during my research period.

I thank my lab mates and friends: Abhijit Das, Biswajit Pathak, Ranjan Kalita, Santanu Konwar, Goutam, Partha Pratim Dey, Zaheer Abbas Ahmed, Obaidulla for the inspiring and encouraging discussions during the Ph.D. work. I would also like to thank my hostel mates Vipin Kumar, Bappaditya Roy, Pankaj, Sukhamoy for making the moments joyful and happiness in the hostel.

I take this opportunity to sincerely acknowledge the financial support from Ministry of Human Resource and Development (MHRD), Government of India during my Ph.D.

The experimental results presented in this thesis are performed in an in-house developed setup. I hereby gratefully acknowledge the major contribution of Ranjan Kalita in developing the setup and his help later in performing the experiments.

Last but not the least, I would like to thank my family: my parents for their support and inspiration throughout my research work. Their infallible love and support has always been my strength. Their patience and sacrifice will remain my inspiration throughout my life.

TH-1501_10612103

TH-1501_10612103

Abstract

Since the last decade there has been a growing interest in cylindrical vector beams, owing to their interesting properties especially under tight focusing conditions. Cylindrical vector beams have axially symmetric polarization profiles or electric field orientations in the pupil plane. Two important members of cylindrical vector beams are the radially polarized and the azimuthally polarized beams. For an azimuthally polarized beam the electric field vector at each location in the pupil plane of the beam points in the direction perpendicular to radius vector, while for a radially polarized beam it points in the radial direction. When a linearly polarized beam (polarized along X) is focused by an aplanatic lens system, in the low numerical aperture (NA) case, the focal volume is primarily X polarized and there is only a negligible amount of Z polarized component. Thus it had appeared to be almost impossible to generate longitudinally polarized light in free space for many years. However, if the same X polarized beam is focused by a high NA lens, the focal volume will also contain a significant amount of Z polarized light where Z is the optical axis of the lens system. Consequently a radially polarized beam when focused gives rise to pure longitudinal polarization at the focal point as the transversely polarized fields interfere destructively. With the increase in the NA of the focusing lens the strength of the longitudinal field at the focus becomes greater than the maximum of the transverse field in the focal volume. The longitudinal field at the focus has certain unique properties, for instance, the corresponding field has non propagating power since it corresponds to a null Poynting vector. An azimuthally polarized beam on the other hand when focused gives rise to a doughnut like intensity distribution both under low NA and high NA conditions.

The unique properties of cylindrical vector beams make them important in many applications. For example the radially polarized beam is used in confocal microscopy for super-resolution, in optical trapping and particle manipulation, in electron acceleration, in laser cutting, to map the orientation of single molecules, while the azimuthally polarized beam is used in optical trapping, in material processing, in dark field imaging, and also in scanning optical microscopy.

All the above applications assume a perfect unaberrated radially polarized or azimuthally polarized beam. However any optical system essentially suffers from aberrations with a degree that may vary from one system to other. Therefore from

TH-1501_10612103

the applications point of view it is imperative to ascertain the effect on the focal volume properties of the cylindrical vector beams due to the aberrations present in the beam. There have already been a few investigations on the effect of aberrations on cylindrical vector beams. However, most of such studies investigated only focal plane properties due to the presence of primary aberrations. Many applications of the cylindrical vector beam, in contrast, depend on the properties of the entire focal volume and not just the focal plane. Besides an optical system may contain a combination of both primary and secondary aberrations. In this thesis we provide a comprehensive study on the effect of both primary and secondary aberrations on the entire focal volume properties of cylindrical vector beams.

The energy density in the focal volume of a linearly polarized beam in the low NA case can be calculated using Scalar Diffraction theory. However, the same can not predict the focal volume in the high NA case. In such cases a vectorial version of the diffraction theory needs to be used. In our work we used the vectorial diffraction theory elaborated in the work of Richards and Wolf. However the integral form of the diffraction theory of Richards and Wolf are not very convenient for beams with a complex pupil function. In such a situation often the Fourier Transform form of the Vectorial diffraction theory becomes more useful. We employ the Fourier Transform form of the vectorial diffraction theory to compute the parameters such as Cartesian field components, energy density, Poynting vector and resultant polarization in the focal volume of aberrated cylindrical vector beams. Our theoretical investigation revealed several important phenomena involving the cylindrical vector beams. Some of the observations include generation of a boat-shaped intensity distribution near the focus of the coma aberrated azimuthally polarized beam, astigmatism resilience of Gaussian like beam derived from an azimuthally polarized beam, appearance of propagating field on the optical axis of a coma aberrated radially polarized beam and so on. We also made use of an experimental arrangement to verify the numerically obtained results in the low NA case.

TH-1501_10612103

Acronyms

NA	-	Numerical Aperture
LPB (XPB)	-	Linearly Polarized Beam
APB	-	Azimuthally Polarized Beam
RPB	-	Radially Polarized Beam
CCD	-	Charge Coupled Device
CGH	-	Computer Generated Holography
H	-	Helical Phase Mask
APBH	-	Azimuthally Polarized Beam With a Helical Phase Mask
DFT	-	Discrete Fourier Transform
FFT	-	Fast Fourier Transform
ID	-	Iris Diaphragm
LCSLM	-	Liquid Crystal Spatial Light Modulator
PBS	-	Polarizing Beam Splitter
P	-	Prism
PH	-	Pinhole
Pol	-	Polarizer
PA	-	Primary Astigmatism
SA	-	Secondary Astigmatism
PC	-	Primary Coma
SC	-	Secondary Coma
PSA	-	Primary Spherical Aberration
SSA	-	Secondary Spherical Aberration
80ER	-	80 % Energy Radius
RMS	-	Root Mean Square

TH-1501_10612103

TH-1501_10612103

Contents

TH-1501_10612103

TH-1501_10612103

TH-1501_10612103

List of Figures

TH-1501_10612103

TH-1501_10612103

TH-1501_10612103

TH-1501_10612103

TH-1501_10612103

TH-1501_10612103

TH-1501_10612103

TH-1501_10612103

TH-1501_10612103

List of Tables

TH-1501_10612103

Chapter 1

General introduction and thesis overview

The properties of light in the focal volume is important in most of the applications where a focused light beam is used. An important property of the focusing lens is the numerical aperture (NA). The Numerical Aperture is a measure of how much light can be collected or emitted by the lens system. It is described by the angle, called the semi-angle of aperture, made by the marginal ray with the optical axis of the lens system. The semi-angle of aperture is also defined as the ratio of the aperture radius and focal length of the focusing the lens. Therefore

$$NA = n \sin \alpha \approx n \frac{D}{2f} \tag{1.1}$$

where n is the refractive index of the medium, α is the semi angle of aperture, D is the diameter of aperture and f is the focal length of lens.

Figures 1.1 (a) and (b) show the schematic of a low and a high NA lens system, respectively. For a low NA lens system, the diameter(D) is small while the focal length(f) is large and the converse is true for the high NA lens system. A larger NA lens will be able to visualize finer details than a lens with a smaller NA. For diffraction limited optics, lenses with larger NA collect more light and hence will give rise to a higher resolution images. However the same will provide shallower depth of field.

When a linearly polarized beam polarized along X is focused by an aplanatic lens system, in the low numerical aperture (NA) condition the focal volume comprises primarily X polarized light as there is only a negligible amount of Z polarized com-

TH-1501_10612103

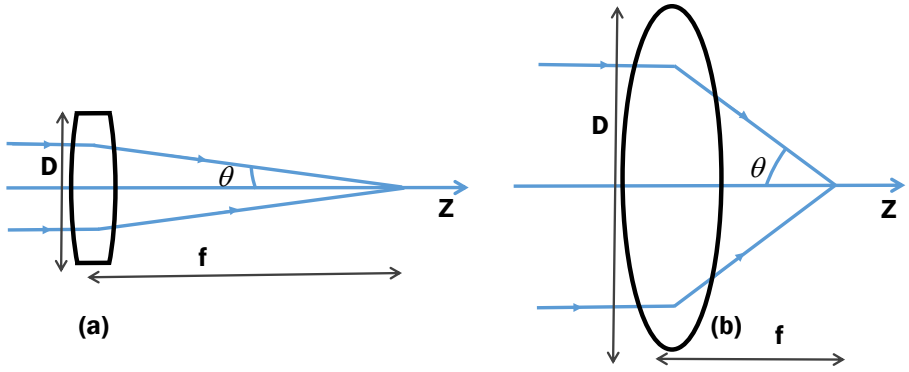

Figure 1.1: (a) A Low numerical aperture focusing lens system and (b) a high numerical aperture focusing lens system. The maximum value of the angle θ is the semi angle of aperture, α.

ponent. Thus in low numerical aperture case the vectorial properties of the beam near the focus is not important. However, later it was shown that any beam of finite diameter has a longitudinal field component, even in a free space [1]. When focused by a high NA lens it is seen that the focal volume due to an X polarized beam also has Z polarized intensity which goes upto about 15% of the maximum of the net intensity in the focal volume for a lens with NA=0.9 . Thus in high numerical aperture focusing condition the vectorial nature of the light near the focus becomes important.

In the recent times there has been a growing interest in cylindrical vector beams, owing to their interesting properties. Cylindrical vector beams are light beams with cylindrically symmetric polarization profiles. Two important members of cylindrical vector beams are the radially polarized beam and the azimuthally polarized beam. For an azimuthally polarized beam the electric field vector at each location in the pupil plane of the beam points in the direction perpendicular to the radius vector, while for a radially polarized beam it points in the radial direction. The radially oriented electric fields in the pupil plane give rise to zero lateral field at the focal point such that only longitudinal component of the electric field can exist there. The strength of the longitudinal component increases as the NA of the focusing lens increases. Beyond a certain numerical aperture the axial component of the radially polarized beam dominates the total intensity near the focus [2] resulting in a sharper focal spot when compared to a linearly polarized beam. This axial field near the focus has non-propagating power and localized in space. The azimuthally polarized beam on the other hand has null intensity at the center of the focal volume for lens

TH-1501_10612103

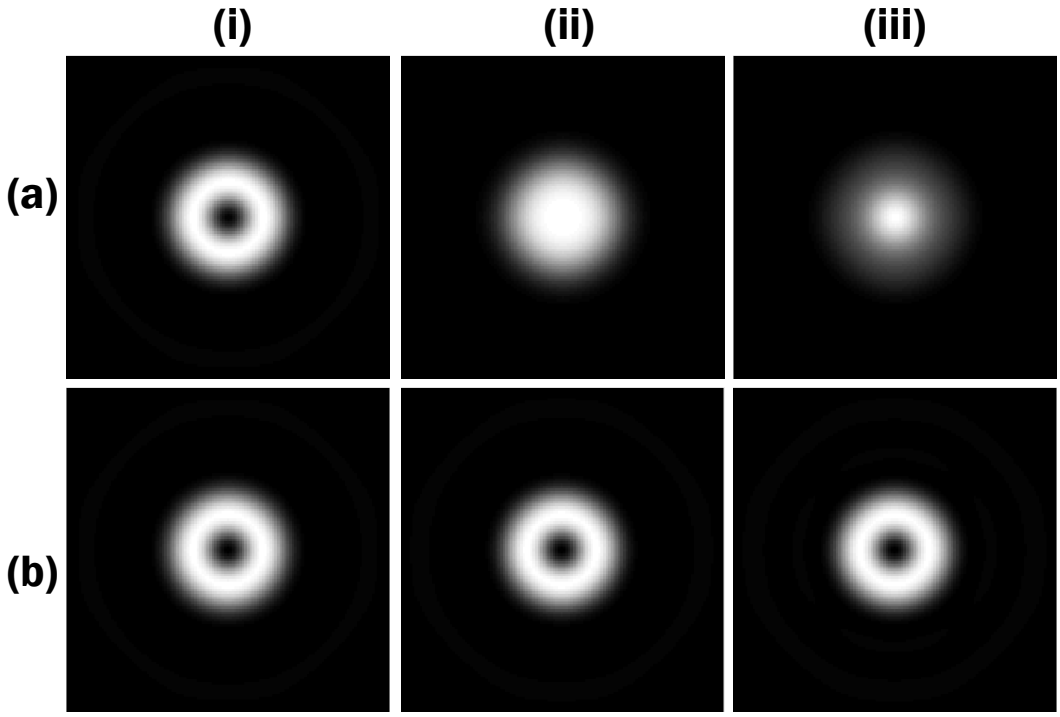

Figure 1.2: Computer simulated focal spots of (a) radially polarized and (b) azimuthally polarized beams using focusing lenses of three different numerical apertures, (i) NA=0.1, (ii) NA=0.74, and (iii) NA=0.9

systems having NA from low to high. Figure 1.2 shows the numerically simulated focal spots (or intensity point spread functions) of (a) radially polarized and (b) azimuthally polarized beams under three different numerical apertures, (i) NA=0.1, (ii) NA=0.74, and (iii) NA=0.9.

The unique properties of the tightly focused cylindrical vector beams make them important in many applications. The radially polarized beam, for example, is used in optical trapping [3, 4, 5, 6], in super-resolution optical microscopy [7], in laser cutting [8], in non-linear microscopy [9], in the study of molecular orientations [10], in the creation of a long needle of axially polarized light [11, 12, 13] and so on. The azimuthally polarized beam, on the other hand, is used in optical trapping [14, 15, 16], in material processing [17], in dark field imaging [18], in the waveguide as a pump beam [19] and also in scanning optical microscopy [20].

Aberration in a light beam focused by a lens is the deviation of the phase profile in the image region from the Gaussian reference sphere. The aberrations present in an optical system leads to significant modifications in the focal volume properties of the beam being focused. An optical system may suffer from various types of

TH-1501_10612103

aberrations. Thus the applications involving the cylindrical vector beam essentially get affected by aberrations to a degree that may vary from case to case. Aberrations present in an optical system can be divided into two groups, namely lower order (such as primary) aberrations and higher order (such as secondary) aberrations. Both the aberrations can be conveniently represented by Zernike polynomials, which are orthogonal polynomials [21] forming a complete set of basis functions to represent classical aberrations. There are published works on the effect of primary aberrations on different types of beams, such as, linearly polarized beam [22, 23], radially polarized vortex beam [24], singular beam [25, 26] and on Gaussian beam [27] etc. However most of the published works dealing with the cylindrical vector beam emphasize the properties of the beam in the focal plane only and thus the properties of the cylindrical vector beams over the entire focal volume is not well investigated. Moreover the effect of secondary aberrations on the focal volume properties of cylindrical vector beams is also not well known.

In this thesis we have taken up a comprehensive study on the effect of various Zernike mode aberrations on the focal volume properties of the two most important members of the cylindrical vector beam. We have used the Fourier transform form of the vectorial diffraction theory [1, 28] to compute the Cartesian component of the electric and magnetic fields near the focus, which are then used to obtain various parameters in the entire focal volume. We have investigated the effect of the most common aberrations, such as primary aberrations on the azimuthally polarized beam. Since many applications of the azimuthally polarized beam exploit the azimuthally oriented electric field vectors in the focal volume, in our study, we also discuss the aberration effect on the polarization profile near the focus of the azimuthally polarized beam. As the effect of primary aberration on the focal plane of a radially polarized has already been studied [24], in this thesis, we present a more complete study of the radially polarized beam by including the effects of both primary and secondary aberrations over the entire focal volume. The numerically obtained focal intensity distributions with a low NA lens are also experimentally verified using a division of wavefront based vector beam forming setup.

The Poynting vector is an important parameter of light beams, which is defined as the energy flow per unit time through unit area [29] of the beam. Poynting vector plays a crucial role in trapping applications as it essentially decides the magnitude of the radian pressure on the trapped particle. The longitudinal field of the radially polarized beam at the focal point corresponds to a zero Poynting vector and hence

TH-1501_10612103

there is no radiation pressure. Thus an unaberrated radially polarized beam may provide an efficient optical trap. In this thesis we also investigate how the Poynting vector profile in the focal volume of a radially polarized beam gets modified due to the presence of various aberrations.

Below we provide a chapter wise overview of the entire thesis work.

The numerical investigations presented in this thesis are based on the vectorial diffraction theory. which can be derived starting from the well known scalar diffraction theory. In **chapter***2* we have briefly discussed the history of scalar diffraction theory, starting with Maxwell's equations. It is followed by a discussion on the integral form of the vectorial diffraction theory of Richards and Wolf [1]. The integral form provides the focal field components near the focus of a lens system, which is illuminated by an X polarized incident beam. This theory can be extended for a Y polarized incident beam and thus for an arbitrarily polarized incident beam by taking the vector sum of two orthogonally polarized pupil functions. However, for discrete and complicated pupil functions and in the presence of aberrations, the integral form is often difficult to use. In such cases the Fourier transform form of the vectorial diffraction theory in Cartesian coordinate system [28], which is also taken up in this thesis, provides a more convenient way. The **chapter***2* discusses the Fast Fourier Transform (FFT) form of the vectorial diffraction theory for an X polarized beam and its extension for a Y polarized beam and eventually for an arbitrarily polarized beam. Further we have also discussed the discrete Fourier transform (DFT) form of the vectorial diffraction theory which provides a computationally less intensive way to compute focal field components with a superior spatial resolution.

In **chapter***3* we have investigated the effect of all the primary aberrations such as astigmatism, coma, trefoil and spherical aberration on an azimuthally polarized beam by using the theory developed in **chapter***2*. In this investigation we have noticed that in the presence of coma the total intensity distribution of an azimuthally polarized beam in the focal volume takes an interesting shape of a boat-like structure. Here we have also investigated how the primary aberrations distort the axially symmetric polarization profile of the azimuthally polarized beam. In this chapter we describe an in-house developed and division of wavefront based vector beam forming setup which will be used to verify some of the numerical results in the low NA case obtained in this thesis work.

In **chapter***4* we have discussed the effect of primary aberrations on an azimuthally polarized beam with a helical phase mask (referred to as APBH). The

TH-1501_10612103

focal intensity distribution of the azimuthally polarized beam with a helical phase mask is very similar to the focal spot of a plane wavefront beam in the low NA case as both the beams have circularly symmetric focal intensity distributions. In this chapter we have investigated the effect of primary aberrations on the APBH and an X polarized beam (XPB) and the relative performance of the two against primary aberrations. We have observed that the effect of astigmatism is less prominent on the APBH as compared to the XPB, thus the APBH is more resistant to astigmatism. Hence the APBH is a better beam for optical systems known to suffer from astigmatism.

In **chapter** *5* we have discussed the effect of both primary and secondary aberrations on a radially polarized beam. Primary aberrations such as astigmatism (Z_6), coma (Z_8), trefoil (Z_{10}) and spherical aberration (Z_{11}) have their counter parts in secondary aberrations such as second astigmatism (Z_{12}), coma (Z_{16}), trefoil (Z_{18}) and spherical aberration (Z_{22}) with a negative sign. In this chapter we have made a comparative investigation on the effect of primary aberrations and their secondary aberration counter parts on the radially polarized beam.

Poynting vector profile of a radially polarized beam plays important role in optical trapping and related applications. In optical trapping, on a trapped particle there exists two forces, (1) the gradient force, and (2) the scattering force such as radiation pressure. Gradient force depends on the intensity value of the laser beam at the focus and the radiation pressure depends on the Poynting vector on the optical axis. In the case of an ideal, unaberrated radially polarized beam, the Poynting vector along the optical axis is zero resulting in zero radiation pressure. Therefore in the case of the radially polarized beam there exists only gradient force towards the focus which helps to trap a particle stably. In **chapter** *6* we have discussed the effect of primary aberrations on the Poynting vector profile near the focus of a radially polarized beam. In this chapter we have investigated the effect of various aberrations on the time average value and time evolution of the Poynting vector. Here we have observed that in the case of coma there appears non zero Poynting vectors along the optical axis. Thus the Poynting vector profile near the focus of a radially polarized beam is maximally effected by coma.

The thesis work is concluded in **chapter** *7* by highlighting the important findings of the thesis work. The same chapter also includes a brief discussion on future prospects.

TH-1501_10612103

Chapter 2

Vectorial diffraction theory

2.1 Introduction

The primary objective of this thesis is the investigation of the effect of aberrations on the various focal volume properties of a tightly focused cylindrical vector beam. The investigation will involve calculation of electric and magnetic field vectors near the focus of the beam. Thus there is a need of a suitable theory to be able to compute the focal field components. In this chapter we start with a brief description on the basic developments in the field of scalar diffraction theory and then discuss their extension to vectorial diffraction theory. We will describe different forms of the vectorial diffraction theory that can be employed to numerically compute the Cartesian components of the electric and the magnetic fields. This chapter will also describe computation of some important physical parameters in the focal volume and the modification in the theory to take into account the effect of aberrations in the beam.

2.2 Maxwell's equations and scalar diffraction theory

Diffraction is one of the phenomena in the realm of physical optics that relates to a propagating electromagnetic wave. It is defined as the deviation of light ray from the rectilinear path and is caused by the confinement of lateral extent of the incident wave. Diffraction effects are more prominent when the size of the confinement is comparable to the wavelength of the light. It plays an important role in all the

TH-1501_10612103

applications involving propagation of light and is the limiting factor on the performance of an imaging system. According to Huygens each point on the wavefront of a disturbance is considered to be a new source of secondary spherical disturbance. Thus the wavefront at later instant can be found by constructing the envelop of the secondary wavelet.

We begin our discussion by stating the Maxwell's equations in electrodynamics. In free space the charge density (ρ) and current density (J) are zero, and hence the Maxwell's equations have the following form

$$\nabla \cdot \vec{E} = 0$$

$$\nabla \cdot \vec{H} = 0$$

$$\nabla \times \vec{E} = -\mu_0 \frac{\partial \vec{H}}{\partial t}$$

$$\nabla \times \vec{H} = \epsilon_0 \frac{\partial \vec{E}}{\partial t}$$

where $\vec{E}$ and $\vec{H}$ represents the electric field and magnetic field vectors.

If the propagation medium is linear, isotropic, homogeneous (i.e. with uniform permittivity ϵ), and non dispersive, then we get wave equations for $\vec{E}$ and $\vec{H}$ from Maxwell's equations as

$$\nabla^2 \vec{E} - \frac{n^2}{c^2} \frac{\partial^2 \vec{E}}{\partial^2 t} = 0 \tag{2.1}$$

$$\nabla^2 \vec{H} - \frac{n^2}{c^2} \frac{\partial^2 \vec{H}}{\partial^2 t} = 0 \tag{2.2}$$

where, $n = \sqrt{\frac{\epsilon}{\epsilon_0}}$ is the refractive index of the medium, $c = \frac{1}{\sqrt{\mu_0 \epsilon_0}}$ is the velocity of light in free space. The two vector wave equations obeyed by $\vec{E}$ and $\vec{H}$, can be replaced by an identical scalar wave equation, as given below, which will be obeyed by any components $u(P,t)$, of these two vectors,

$$\nabla^2 u(P,t) - \frac{n^2}{c^2} \frac{\partial^2 u(P,t)}{\partial^2 t} = 0 \tag{2.3}$$

Considering harmonic time dependence, we may write $u(P,t) = \Re\{U(P)\, e^{-i2\pi\nu t}\}$. Substituting $u(P,t)$ in the above time dependent wave equation, we obtain

TH-1501_10612103

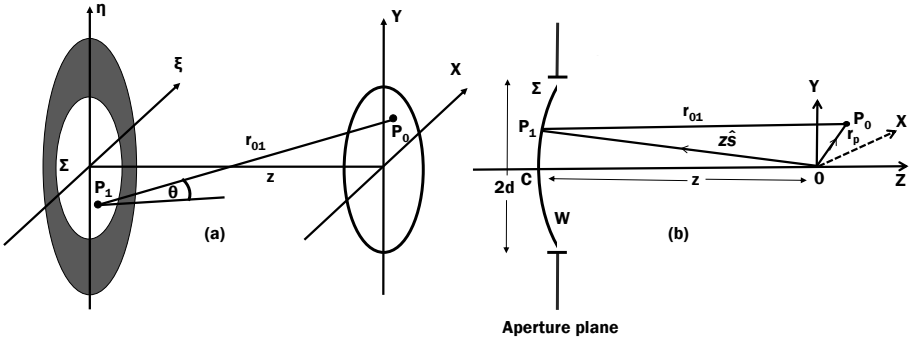

Figure 2.1: (a) Schematic of an aperture Σ illuminated by monochromatic light, and (b) a spherical wave incident on a circular aperture.

$$(\nabla^2 + k_0^2)U = 0 \tag{2.4}$$

where $k_0 = 2\pi n\frac{\nu}{c}$ is the wave number. The time independent wave equation 2.4 is known as the Helmholtz equation. The complex amplitude of any monochromatic wave propagating in vacuum or in a homogeneous medium must obey such a relation.

Scalar diffraction theory relates to the conversion of the scalar wave equation, which is a partial differential equation, into an integral equation. It can be used to study and to analyze most types of diffraction phenomena and imaging systems subjected to the approximations. The first important attempt to solve the Helmholtz equation to develop an integral theorem is by Kirchhoff and it is the basis for the mathematical formulation of scalar diffraction theory [30, 31]. The results of scalar diffraction theory holds when the wavelength of light is much smaller than the aperture size of the diffracting device used to control the wave. The Kirchhoff formulation of diffraction can be made use to obtain the complex amplitude at a point P_0 behind an aperture Σ as shown in Fig. 2.1 (a), where complex amplitude at each point P_1 inside the aperture is known, considering monochromatic illumination at wave number k_0. This is known as Huygens-Fresnel principle, given by

$$U(P_0) = \frac{1}{i\lambda}\iint_{\Sigma} U(P_1)\frac{e^{ik_0 r_{01}}}{r_{01}}\cos\theta\, ds \tag{2.5}$$

Here $\vec{r_{01}}$ is the vector joining P_0 and P_1, ds is the area element, and θ is the angle between $\vec{r_{01}}$ and the normal to the aperture plane.

We then consider a spherical monochromatic wave W incident on a circular aperture Σ of radius d and converging towards the axial point O as shown in Fig.

TH-1501_10612103

2.1 (b). P_0 is a point in the neighbourhood of O with $\vec{r_p}$ as the position vector. Assuming that r_p and d of the aperture are small compared to the radius z=CO of the wave-front W and $\frac{a}{z}$ as the amplitude at point P_1 of the incident wave, according to Huygens-Fresnel principle we can write

$$U(P_0) = \frac{1}{i\lambda}\frac{ae^{ik_0 z}}{z}\iint_{\Omega}\frac{e^{ik_0 r_{01}}}{r_{01}}\,ds \tag{2.6}$$

Here $U(P_0)$ is the field at point P_0 and r_{01} is the distance between point P_0 and point P_1 on the Wave-front. Further assuming the variation of the inclination factor over the wave-front as negligible and taking r_{01}=z, the Eq. 2.6, takes the form [30]

$$U(P_0) = \frac{1}{i\lambda}a\iint_{\Omega} e^{ik_0\hat{s}.\vec{r}_p}\,d\Omega \tag{2.7}$$

where we have taken ds=$z^2 d\Omega$ and $d\Omega$ as the solid angle subtended by ds at O. The Eq. 2.7 is known as the Debye diffraction formula that provides the scalar field near the focus as the superposition of plane waves traveling in different directions. To be noted that in this derivation a is taken as a scalar constant and hence was kept outside the integral.

However the scalar nature of the above kind of beam propagation model does not take into account the interdependence of the different components of the electromagnetic fields. Therefore to accurately model the propagation of light which does not conform to the usual thin lens and paraxial approximations, one requires a more rigorous approach that incorporates the full-vector nature of electromagnetic radiation.

2.3 Vectorial diffraction theory

Beginning with the work of Ignatowsky [32] there are a number of different methods available, which discuss the vectorial nature of the diffracted light [33, 34]. One of the most important and successful approximation was introduced by Richards and Wolf in 1959 [1, 35]. Their work may be regarded as the vectorial generalization of the Debye diffraction formula which is discussed in the previous section. In this vectorial generalization the amplitude is taken as vector quantity which need not necessarily be a constant throughout the aperture. In this theory, the electric (and magnetic) field near the focus is taken as the superposition of plane waves weighed

TH-1501_10612103

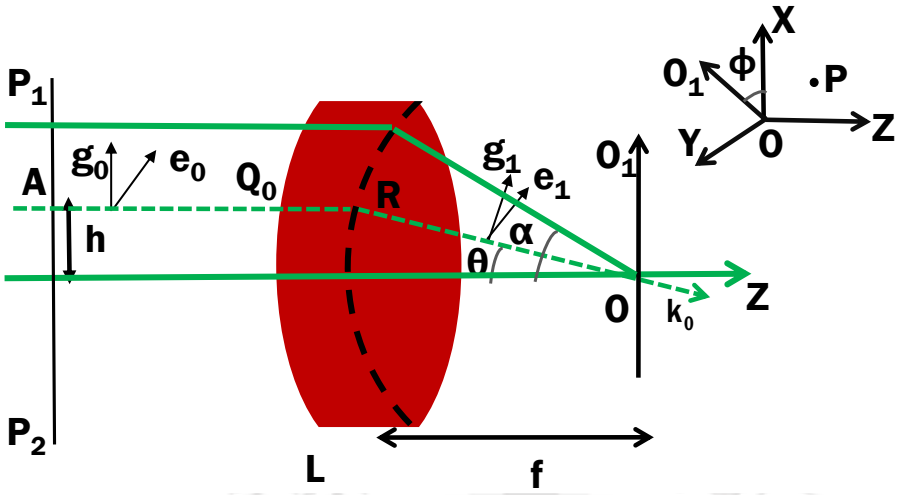

Figure 2.2: Focusing of an incident beam by an aplanatic lens system. $\hat{g_O}$ and $\hat{g_1}$ are the unit vectors normal to the ray and away from the optical axis. The incident rays are assumed to suffer refraction at a single surface called the focal sphere indicted by dashed lines

by a strength factor, which is the electric (or magnetic) field associated with each ray forming the image.

The model by Richards and Wolf assumes a monochromatic point source emitting electromagnetic wave of angular frequency ω which is situated in the object space of a system of revolution as shown in Fig. 2.2. Also

$$\vec{E}(P,t) = \Re(\vec{e}(P)e^{-iwt}), \quad \vec{H}(P,t) = \Re(\vec{h}(P)e^{-iwt}) \tag{2.8}$$

represent the electric and magnetic vectors, at a point P in the image space, at time t. The vectors $\vec{e}$ and $\vec{h}$ are complex numbers, and the symbol $\Re$ denotes the real part.

The integral expressions for electric and magnetic field components at the point $P(x_P, y_P, z_P)$ in the image space, which is not too close to the exit pupil, are given as

$$\vec{e}(x_P, y_P, z_P) = -\frac{ik_0}{2\pi}\iint_\Omega \frac{\vec{a}(s_x, s_y)}{s_z} e^{ik_0(\Phi(s_x,s_y)+s_x x_P+s_y y_P+s_z z_P)} ds_x\, ds_y \tag{2.9}$$

$$\vec{h}(x_P, y_P, z_P) = -\frac{ik_0}{2\pi}\iint_\Omega \frac{\vec{b}(s_x, s_y)}{s_z} e^{ik_0(\Phi(s_x,s_y)+s_x x_P+s_y y_P+s_z z_P)}\, ds_x\, ds_y \tag{2.10}$$

In the above equations $\vec{a}$ and $\vec{b}$ are the strength factors of the unperturbed electric and magnetic fields which are incident on the exit pupil. Here $k_0 = \frac{w}{c} = \frac{2\pi}{\lambda}$ is the

TH-1501_10612103

vacuum wave number and λ is the vacuum wave length. Further, Φ is the aberration function present in the system, and s_x, s_y, s_z are the components of the unit vector $\hat{s}$ (indicating the direction of the propagation of the light) along a typical ray in the image space. Ω is the solid angle formed by all the geometrical rays which pass through the exit pupil of the system. The strength factors are related by formula $\vec{b} = \hat{s} \times \vec{a}$. In the problem under consideration, the imaging is aplanatic so that the wavefront in the image space is spherical, with a common centre at the Gaussian image point. Hence, for all vectors $\hat{s}$ in the solid angle Ω,

$$\Phi(s_x, s_y) = 0 \tag{2.11}$$

2.3.1 Integral expressions for an X polarized beam

We consider an aplanatic lens L of focal length f which is shown in Fig. 2.2. A point source (such as a small Hertzian dipole oriented parallel to the X axis) at infinity along the optical axis gives rise to an X polarized monochromatic wave in the entrance pupil P_1P_2 of the focusing lens. Let AQ_0 be a typical ray parallel to the optical axis in the object space, incident on P_1P_2 at a height h from the optical axis and the corresponding ray RO in the image space is making an angle θ with it. The maximum value of θ is α, defined as the semi angle of aperture of the lens L, when AQ_0 corresponds to the marginal ray. $\vec{l_0}$ is the amplitude vector at A in the entrance pupil, and $\vec{l_1}$ is the amplitude vector at R in the exit pupil which is taken as a sphere of radius f (called the focal sphere indicated by dashed lines). The electric field vectors corresponding to AQ_0 and RO are $\vec{e_0}$ and $\vec{e_1}$, respectively, such that $\hat{e_0} = \hat{x}$ and

$$\vec{e_0} = l_0\, \hat{e_0}\, e^{ik\xi_0}$$

and

$$\vec{e_1} = l_1\, \hat{e_1}\, e^{ik\xi_1}$$

where ξ_0 and ξ_1 are the corresponding eikonal functions.

Now according to the sine condition

$$h = f \sin\theta. \tag{2.12}$$

The losses of energy due to reflection and absorption within the system are negligible. Hence from considering annular areas δs_0 and δs_1 in the entrance pupil and in the

TH-1501_10612103

focal sphere we have

$$\delta s_0 = \delta s_1 cos\theta, \tag{2.13}$$

such that

$$l_1 = l_0 \cos^{\frac{1}{2}} \theta. \tag{2.14}$$

The expression of $\vec{a}$ in Eq. 2.9 can eventually be written as

$$\vec{a} = f l_0 \cos^{\frac{1}{2}} \theta \hat{\mathbf{e}}_1. \tag{2.15}$$

The components (s_x, s_y, s_z) of the unit vector $\hat{s}$ along a ray in the image space and the co-ordinates (x_P, y_P, z_P) of the field point P in the image region are expressed in the spherical co-ordinates. Therefore

$$s_x x + s_y y + s_z z = r_P \cos\epsilon, \tag{2.16}$$

where

$$\cos\epsilon = \cos\theta\cos\theta_P + \sin\theta\sin\theta_P\cos(\phi - \phi_P). \tag{2.17}$$

and

$$\frac{ds_x ds_y}{s_z} = d\Omega = sin\theta d\theta d\phi. \tag{2.18}$$

Under the assumption that the angle of incidence on each refracting surface is small such that the orientation between the electric field and magnetic field vectors and the meridional plane remains constant, one can derive the Cartesian components of $\hat{e_1}$. Thus for the point P in the focal volume and for the X polarized incident beam, the Cartesian components of the electric field E_{XX}, E_{XY} and E_{XZ} are written as

$$\begin{aligned}
E_{XX} &= -\frac{iA}{\pi}\iint_V \sqrt{\cos\theta}(\cos\theta + (1 - cos\theta)\sin^2\phi))e^{ik_0 r_P \cos\epsilon}\sin\theta d\theta\ d\phi. \\
E_{XY} &= \frac{iA}{\pi}\int_0^{\alpha}\int_0^{2\pi} (1-\cos\theta)\cos\phi\sin\phi\sqrt{\cos\theta}e^{ik_0 r_P\cos\epsilon}\sin\theta d\theta\, d\phi. \\
E_{XZ} &= \frac{iA}{\pi}\int_0^{\alpha}\int_0^{2\pi} \sin\theta\cos\phi\sqrt{\cos\theta}e^{ik_0 r_P\cos\epsilon}\sin\theta d\theta\, d\phi.
\end{aligned} \tag{2.19}$$

TH-1501_10612103

and the Cartesian components of the magnetic field are written as

$$\begin{aligned} H_{XX} &= \frac{iA}{\pi}\int_0^{\alpha}\int_0^{2\pi}(1-\cos\theta)\cos\phi\sin\phi\sqrt{\cos\theta}e^{ik_0 r_P\cos\epsilon}\sin\theta d\theta\ d\phi \\ H_{XY} &= -\frac{iA}{\pi}\int_0^{\alpha}\int_0^{2\pi}\sqrt{\cos\theta}((1-(1-cos\theta)\sin^2\phi)))e^{ik_0 r_P\cos\epsilon}\sin\theta d\theta\, d\phi. \\ H_{XZ} &= \frac{iA}{\pi}\int_0^{\alpha}\int_0^{2\pi}\sin\theta\sin\phi\sqrt{\cos\theta}e^{ik_0 r_P\cos\epsilon}\sin\theta d\theta\, d\phi. \end{aligned} \tag{2.20}$$

where, $A = \frac{k_0 f l_0}{2}$.

2.3.2 Integral expressions for a Y polarized beam

Considering the incident monochromatic beam to be Y polarized, we have $\hat{e_0} = \hat{y}$. Consequently the Cartesian components of $\vec{a}$ can again be derived. Thus for the point P in the focal volume and for a Y polarized incident beam, the Cartesian components of the electric field can be written as

$$\begin{aligned} E_{YX} &= \frac{iA}{\pi}\int_0^{\alpha}\int_0^{2\pi}(1-\cos\theta)\cos\phi\sin\phi\sqrt{\cos\theta}e^{ik_0 r_P\cos\epsilon}\sin\theta d\theta\ d\phi \\ E_{YY} &= -\frac{iA}{\pi}\int_0^{\alpha}\int_0^{2\pi}\sqrt{\cos\theta}((1-(1-cos\theta)\sin^2\phi)))e^{ik_0 r_P\cos\epsilon}\sin\theta d\theta\, d\phi. \\ E_{YZ} &= \frac{iA}{\pi}\int_0^{\alpha}\int_0^{2\pi}\sin\theta\sin\phi\sqrt{\cos\theta}e^{ik_0 r_P\cos\epsilon}\sin\theta d\theta\, d\phi. \end{aligned} \tag{2.21}$$

and the same for the magnetic field are written as,

$$\begin{aligned} H_{YX} &= \frac{iA}{\pi}\int_0^{\alpha}\int_0^{2\pi}\sqrt{\cos\theta}(\cos\theta+(1-cos\theta)\sin^2\phi))e^{ik_0 r_P\cos\epsilon}\sin\theta d\theta\ d\phi. \\ H_{YY} &= -\frac{iA}{\pi}\int_0^{\alpha}\int_0^{2\pi}(1-\cos\theta)\cos\phi\sin\phi\sqrt{\cos\theta}e^{ik_0 r_P\cos\epsilon}\sin\theta d\theta\, d\phi. \\ H_{YZ} &= -\frac{iA}{\pi}\int_0^{\alpha}\int_0^{2\pi}\sin\theta\cos\phi\sqrt{\cos\theta}e^{ik_0 r_P\cos\epsilon}\sin\theta d\theta\, d\phi. \end{aligned} \tag{2.22}$$

2.3.3 Integral expressions for an arbitrarily polarized beam

An arbitrarily polarized beam may considered to be a laser beam whose pupil plane comprises electric field vector distributions which may be arbitrary or user defined in terms of orientation and the magnitude of the vectors. It is possible to split such a pupil plane into two constituent pupil planes, one comprising X polarized light

TH-1501_10612103

represented by a certain 2D function, say l_x, describing the magnitude of the X polarized light and the other comprising Y polarized light represented by another function, l_y, describing the magnitude of the Y polarized light. The Cartesian components of electric field and magnetic field for the X polarized pupil can be obtained using a modified form of the equations 2.19, and 2.20. Similarly the same for the Y polarized pupil can be obtained using a modified form of the equations 2.21 and 2.22. In order to obtain the modified form l_0 in A is replaced by l_x for the X polarized pupil and by l_y for the Y polarized pupil. Since in the modified form A is function of θ and ϕ hence it is incorporated into the integrand. Thus we have

$$\begin{aligned}
E_{XX} &= -\frac{if}{\lambda}\int_0^{\alpha}\int_0^{2\pi} l_x\sqrt{\cos\theta}(\cos\theta + (1-cos\theta)\sin^2\phi)e^{ik_0 r_P\cos\epsilon}\sin\theta d\theta\ d\phi. \\
E_{XY} &= \frac{if}{\lambda}\int_0^{\alpha}\int_0^{2\pi} l_x\ (1-\cos\theta)\cos\phi\sin\phi\sqrt{\cos\theta}e^{ik_0 r_P\cos\epsilon}\sin\theta d\theta\, d\phi. \qquad (2.23) \\
E_{XZ} &= \frac{if}{\lambda}\int_0^{\alpha}\int_0^{2\pi} l_x\ \sin\theta\cos\phi\sqrt{\cos\theta}e^{ik_0 r_P\cos\epsilon}\sin\theta d\theta\, d\phi.
\end{aligned}$$

and

$$\begin{aligned}
E_{YX} &= \frac{if}{\lambda}\int_0^{\alpha}\int_0^{2\pi} l_y\,(1-\cos\theta)\cos\phi\sin\phi\sqrt{\cos\theta}e^{ik_0 r_P\cos\epsilon}\sin\theta d\theta\ d\phi \\
E_{YY} &= -\frac{if}{\lambda}\int_0^{\alpha}\int_0^{2\pi} l_y\sqrt{\cos\theta}((1-(1-cos\theta)\sin^2\phi)))e^{ik_0 r_P\cos\epsilon}\sin\theta d\theta\, d\phi. \\
E_{YZ} &= \frac{if}{\lambda}\int_0^{\alpha}\int_0^{2\pi} l_y\ \sin\theta\sin\phi\sqrt{\cos\theta}e^{ik_0 r_P\cos\epsilon}\sin\theta d\theta\, d\phi. \qquad (2.24)
\end{aligned}$$

Therefore the Cartesian components of the electric field near the focus of an arbitrarily polarized beam can be written as

$$\begin{aligned}
E_X &= E_{XX} + E_{YX} \\
E_Y &= E_{XY} + E_{YY} \qquad (2.25) \\
E_Z &= E_{XZ} + E_{YZ}
\end{aligned}$$

Similar modifications can be performed in the magnetic field expressions and thus the Cartesian components of the magnetic field near the focus of an arbitrarily

TH-1501_10612103

polarized beam can be written as

$$\begin{aligned} H_X &= H_{XX} + H_{YX} \\ H_Y &= H_{XY} + H_{YY} \\ H_Z &= H_{XZ} + H_{YZ} \end{aligned} \tag{2.26}$$

2.4 Fast Fourier Transform form of vectorial diffraction theory

Integral form of the vectorial diffraction theory as elaborated above is easy and convenient only for pupil functions which have a simple analytical form. However this integral form is not easy to handle for pupil functions which have discontinuities or which do not have a simple analytical form, for instance, pupil functions in the presence of aberrations. Therefore to compute the focal field components of an arbitrarily polarized beam there is a need to look for a more convenient theory.

It was shown [36] that the diffraction integral near the focus can be carried out using a combination of Fourier Transforms (FT). The Cartesian components of the field near the focus can be computed [37] by using Fast Fourier Transforms (FFT) on the input field. However here input field needs to be described as the superposition of the radial and azimuthal (tangential) components. Later it was demonstrated that the integral form of the vectorial diffraction theory can also be converted into a Fourier transform form [28] in Cartesian coordinate system. Using this FT form one can easily and quickly compute electric field and magnetic field components near the focus even for complex pupil functions by using easily available Fast Fourier transform tools. In this particular scheme the input field needs to be describe as the superposition of X and Y polarized input field components. Thus the scheme [28] is more suitable for experimental setups generating an arbitrary vector beam as a combination of X and Y polarized fields.

2.4.1 Expressions for an X polarized beam

The electric field at $P(\vec{r}_P)$, such that $r_P << f$, can be defined as the Fourier transform of the 3D vectorial pupil function in k-space defined by the three mutually perpendicular axes (k_x, k_y, k_z). The pupil function in the k-space is denoted by

TH-1501_10612103

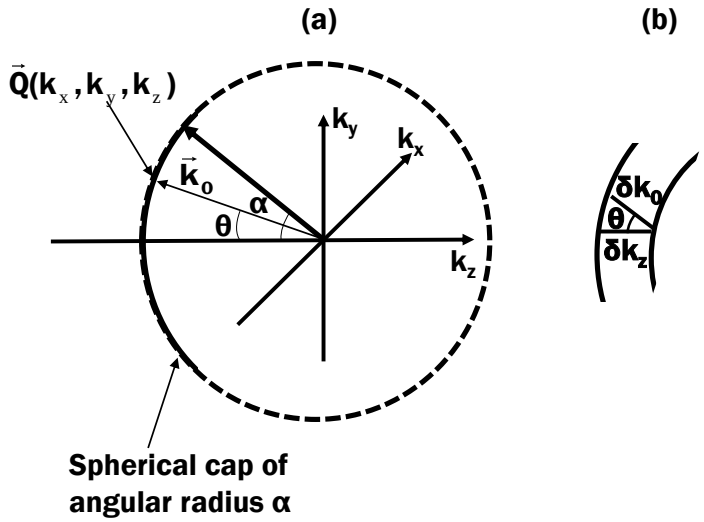

Figure 2.3: (a) Spherical cap of the three dimensional pupil plane, and (b) magnified view of a section of the spherical shell.

$\vec{L_1}(\vec{Q})$ where $\vec{Q} = (k_x, k_y, k_z)$ in Cartesian coordinate system or (k_0, θ, ϕ) in polar coordinate system. As shown in Fig. 2.3, the 3D pupil function is obtained by taking a cap off a sphere of radius k_0. The field at the point $P(\vec{r}_P)$, as shown in Fig. 2.2, barring some constant terms can be written as

$$E\vec{X}(P) = \int \vec{L}_1(\vec{Q}) e^{i\vec{k}_0\vec{r}_P} d\nu_Q \tag{2.27}$$

In the above expression $d\nu_Q = dk_x dk_y dk_z$ is the volume element in k-space and the integration is performed over the entire space. Since the pupil function is non zero only inside a spherical shell between radii k_0 and $k_0 - \delta k_0$ such that $\delta k_0 \rightarrow 0$, it is possible to write, after slicing the pupil function along the k_z=0 plane,

$$\vec{L}_1(\vec{Q}) = \vec{L}'_1(\vec{Q})\frac{k_0}{k_z}\delta(k_z - \sqrt{k_0^2 - k_r^2}) + \vec{L}'_1(\vec{Q})\frac{k_0}{k_z}\delta(k_z + \sqrt{k_0^2 - k_r^2}) \tag{2.28}$$

where $\vec{L}'_1(\vec{Q})$ is the generalized 3D pupil function and $k_r = \sqrt{k_x^2 + k_y^2}$. The two terms on the right of Eq. 2.28 corresponds to two pupil functions, for the forward propagating and the backward propagating beams, respectively. Considering the forward propagating beam we thus have

$$\vec{E}X(P) = \int_0^\infty \int_0^\infty [\int_0^\infty \vec{L}'_1(\vec{Q})\frac{k_0}{k_z}\delta(k_z - \sqrt{k_0^2 - k_r^2}) e^{i\vec{k}_0\vec{r}_P} dk_z] dk_x dk_y \tag{2.29}$$

TH-1501_10612103

Performing the integration over k_z and using the property of Dirac-delta function, we have

$$\vec{E}X(P) = \int_0^\infty \int_0^\infty \vec{L}_1'(k_x, k_y, \sqrt{k_0^2 - k_r^2}) \frac{k_0}{\sqrt{k_0^2 - k_r^2}} e^{i\vec{k}_0 \vec{r}_P} \, dk_x \, dk_y \tag{2.30}$$

Referring to the Figs. 2.2 and 2.3, it is seen that polar co-ordinates of R and $\vec{Q}$ only differ in the magnitude of the radius vectors and $\vec{L}_1'$ depends only on (k_x, k_y). Therefore we have $\vec{L}_1'(k_x, k_y, \sqrt{k_0^2 - k_r^2})$= Cn$\times\vec{l}_1(k_x, k_y)$, where Cn is a constant. Hence the above equation can now be written as

$$\vec{E}X(P) = \int_0^\infty \int_0^\infty [e^{ik_P z_P} \vec{l}_1(k_x, k_y) \cos^{-1}\theta] e^{i(k_x x_P + k_y y_P)} dk_x \, dk_y \tag{2.31}$$

where $\cos^{-1}\theta = \frac{k_0}{\sqrt{k_0^2 - k_r^2}}$. It is noticed that the Eq. 2.31 represents the 2D Fourier transform in Cartesian co-ordinates (k_x, k_y) of the expression within the bracket. Hence we may write

$$\vec{E}X(P) = F\left[e^{ik_z z_P} \vec{l}_1(k_x, k_y) \cos^{-1}\theta\right] \tag{2.32}$$

where $F[...]$ represents the Fourier transform in the Cartesian co-ordinate system. To be noted that if the Fourier transform is performed by the readily available FFT tool then the operation results in data over an entire plane passing through the point P and perpendicular to the optical axis. Following Eq. 2.19, the Cartesian components of l_1 are written as

$$\begin{aligned} l_{1x} &= l_0 \sqrt{\cos\theta}[\cos\theta + \sin^2\phi(1 - \cos\theta)] \\ l_{1y} &= l_0 \sqrt{\cos\theta}[(\cos\theta - 1)\sin\phi\cos\phi] \\ l_{1z} &= l_0 \sqrt{\cos\theta}\sin\theta\cos\phi \end{aligned} \tag{2.33}$$

The θ and ϕ dependent terms in the field expressions can be written in terms k_x, k_y and α, using the relations $\cos\theta = \frac{k_z}{k_0}$, $\sin\theta = \frac{k_r}{k_0}$, $\cos\phi = \frac{k_x}{k_r}$, and $\sin\phi = \frac{k_y}{k_r}$. Further we have $k_z = \sqrt{k_0^2 - k_r^2}$ and $k_0 \sin\alpha = 1$. Thus if $l_0(k_x, k_y)$ is the pupil function for an X polarized beam, then the electric field components on the plane (perpendicular

TH-1501_10612103

to the optical axis) passing through P can be written as,

$$\begin{aligned} EX_X &= F[l_0(k_x,k_y)G_X(k_x,k_y)] \\ EX_Y &= F[l_0(k_x,k_y)G_Y(k_x,k_y)] \\ EX_Z &= F[l_0(k_x,k_y)G_Z(k_x,k_y)] \end{aligned} \tag{2.34}$$

where

$$\begin{aligned} G_X(k_x,k_y) &= -ie^{ik_z z_P}\sqrt{\frac{k_0}{k_z}}\frac{k_0k_y^2+k_zk_x^2}{k_0k_r^2} \\ G_Y(k_x,k_y) &= ie^{ik_z z_P}\sqrt{\frac{k_0}{k_z}}\frac{(k_0-k_z)k_xk_y}{k_0k_r^2} \\ G_Z(k_x,k_y) &= ie^{ik_z z_P}\sqrt{\frac{k_0}{k_z}}\frac{k_x}{k_0} \end{aligned} \tag{2.35}$$

Similarly expressions for magnetic field on the plane passing through P for the same X polarized pupil are written as,

$$\begin{aligned} HX_X &= F[l_0(k_x,k_y)F_X(k_x,k_y)] \\ HX_Y &= F[l_0(k_x,k_y)F_Y(k_x,k_y)] \\ HX_Z &= F[l_0(k_x,k_y)F_Z(k_x,k_y)] \end{aligned} \tag{2.36}$$

where

$$\begin{aligned} F_X(k_x,k_y) &= ie^{ik_z z_P}\sqrt{\frac{k_0}{k_z}}\frac{(k_0-k_z)k_xk_y}{k_0k_r^2} \\ F_Y(k_x,k_y) &= -ie^{ik_z z_P}\sqrt{\frac{k_0}{k_z}}\frac{k_0k_x^2+k_zk_y^2}{k_0k_r^2} \\ F_Z(k_x,k_y) &= ie^{ik_z z_P}\sqrt{\frac{k_0}{k_z}}\frac{k_y}{k_0} \end{aligned} \tag{2.37}$$

In the above expressions $G_{X,Y,Z}$, $F_{X,Y,Z}$ and l_0 are 2D matrices having the same number of rows and columns.

2.4.2 Expressions for a Y polarized beam

We then assume a Y polarized field in the entrance pupil with $\vec{l_0}$ as the corresponding amplitude vector. We consider a new co-ordinate system, denoted as the primed

TH-1501_10612103

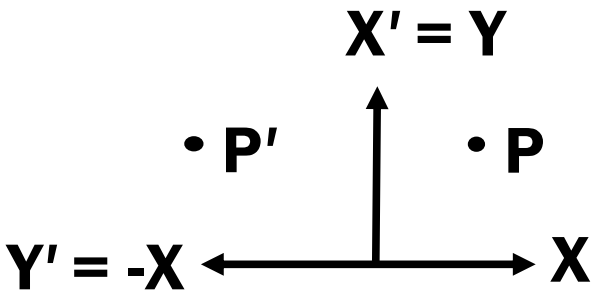

Figure 2.4: Co-ordinate rotation for the Y polarized pupil plane with respect to the X polarized pupil plane.

coordinate system, which is realized by rotating the unprimed co-ordinate system in Fig. 2.2 about Z axis by an angle of $\frac{\pi}{2}$ rad in the anti-clockwise direction, as shown in Fig. 2.4. The two co-ordinate systems are thus related as

$$(X, Y, Z) \Longleftrightarrow (-Y', X', Z') \tag{2.38}$$

It is now seen that the electric field components EY_X, EY_Y and EY_Z, at P in the focal volume can be obtained by using the Eqs. 2.34 as shown below

$$EY_{X,Y,Z} = R_C(F[(QY_{X,Y,Z})]) \tag{2.39}$$

where

$$\begin{aligned} QY_X &= -l_0'(k_x, k_y)G_Y(k_x, k_y) \\ QY_Y &= l_0'(k_x, k_y)G_X(k_x, k_y) \\ QY_Z &= l_0'(k_x, k_y)G_Z(k_x, k_y) \end{aligned} \tag{2.40}$$

Here $l_0' = R_C(l_0)$ such that R_C is a rotation by 90° in the clockwise direction, operated on the matrix on the right. Similarly the expressions for X, Y and Z components of the magnetic field, HY_X, HY_Y and HY_Z for the Y polarized beam are,

$$HY_{X,Y,Z} = R_C(F[(TY_{X,Y,Z})]) \tag{2.41}$$

TH-1501_10612103

where

$$\begin{aligned} TY_X &= -l_0'(k_x,k_y)F_Y(k_x,k_y) \\ TY_Y &= l_0'(k_x,k_y)F_X(k_x,k_y) \\ TY_Z &= l_0'(k_x,k_y)F_Z(k_x,k_y) \end{aligned} \tag{2.42}$$

2.4.3 Expressions for an arbitrarily polarized beam

In order to get the expressions of the Cartesian components of the electric and the magnetic field of an arbitrarily polarized beam we again decompose the pupil function into an X polarized pupil function and a Y polarized pupil function. Let l_x and l_y are the two constituent orthogonally polarized pupil functions. The electric field components $EX_{X,Y,Z}$ and the magnetic field components $HX_{X,Y,Z}$ at the point P near the focus for the X polarized pupil are obtained by replacing $l_0 = l_x$ in Eqs. 2.34 and 2.39. The electric field components $EY_{X,Y,Z}$ and magnetic field components $HY_{X,Y,Z}$ for the Y polarized pupil are obtained by replacing $l_0 = l_y$ in Eqs. 2.36 and 2.41. The resultant electric and magnetic field components due to the arbitrarily polarized beam can thus be written as,

$$\begin{aligned} E_X &= EX_X + EY_X \\ E_Y &= EX_Y + EY_Y \\ E_Z &= EX_Z + EY_Z \\ H_X &= HX_X + HY_X \\ H_Y &= HX_Y + HY_Y \\ H_Z &= HX_Z + HY_Z \end{aligned} \tag{2.43}$$

Considering the Jones matrix representation of a beam as

$$\begin{pmatrix} J_x \\ J_y \end{pmatrix}$$

In this thesis we will assume the cylindrical vector beam to have a uniform amplitude profile. Hence the electric and magnetic field components near the focus can be computed by using $l_x = J_x$ for the X polarized pupil plane and $l_y = J_y$ for the Y polarized pupil plane. Thus knowing the Jones matrix representation of an arbitrary

TH-1501_10612103

beam, the Cartesian components of electric and magnetic field near the focus can be computed.

2.5 Vectorial diffraction theory using Discrete Fourier Transform

The Discrete Fourier Transform (DFT) is a numerical variant of the Fourier Transform where discrete sets of space data are converted into a discrete sets of frequency data [38]. In FFT form of Fourier transform one needs to compute the entire spatial frequency spectrum, while in DFT it is possible to compute only a specific set of spatial frequencies. Thus when incorporated into the Fourier transform form of the vectorial diffraction theory, DFT allows quick computation of a magnified version of a small focal volume.

Consider a vector of n input amplitudes such as $x[0], x[1], x[2], \cdots, x[n-2], x[n-1]$. The Discrete Fourier Transform yields a set of n frequency magnitudes, $f[k]$, expressed as

$$f[k] = \sum_{n=0}^{N-1} x[n] e^{\frac{-i\,2\pi k n}{N}} \tag{2.44}$$

here, k is used to denote the frequency domain ordinate, and n is used to represent the space domain ordinate, while N is the length of the sequence to be transformed.

The Inverse DFT (IDFT) is given by the following equation

$$x[n] = \frac{1}{N} \sum_{k=0}^{N-1} X[k] W_N^{-kn} \tag{2.45}$$

where

$$W_N = e^{-j2\pi/N}$$

Again here also N is the length of the transformed sequence.

Expression for 2D Discrete Fourier Transform (DFT) is given as

$$f[k_x, k_y] = \frac{1}{MN} \sum_{m=0}^{M-1} \sum_{n=0}^{N-1} x[m,n]\, e^{-i\,2\pi(\frac{mk_x}{M} + \frac{nk_y}{N})} \tag{2.46}$$

Here $x[m,n]$ represents spacial data having M rows and N columns, and $f[k_x, k_y]$ represents frequency data as (m, n) represent the spatial co-ordinates and (k_x, k_y)

TH-1501_10612103

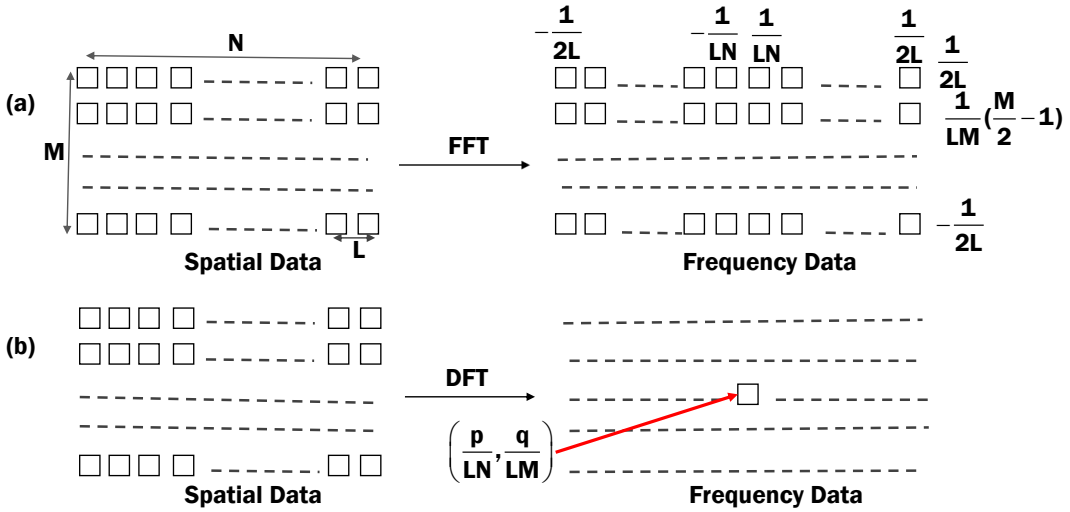

Figure 2.5: Schematic showing the difference between (a) the FFT based computation of the entire frequency plane and (b) the DFT based computation of specific frequency component. The pixel with co-ordinate (p, q) will correspond to spatial frequency co-ordinates $(k_x, k_y) = (\frac{p}{LN}, \frac{q}{LM})$.

represent the frequency coordinates. The same 2D DFT expression can also be written as

$$f[k_x, k_y] = \frac{1}{MN} \sum_{m=-M/2}^{M/2} \sum_{n=-N/2}^{N/2} x[m,n]\, e^{-i\,2\pi(\frac{mk_x}{M} + \frac{nk_y}{N})}. \tag{2.47}$$

Figure 2.5 depicts a comparison between the FFT based computation of the entire frequency plane and DFT based computation of specific frequency component. We may represent the two Eqs . 2.46 and 2.47, as

$$f[k_x, k_y] = DFT\,[x]\,(k_x, k_y). \tag{2.48}$$

Thus we can write the DFT form of Eq. 2.34 as

$$\begin{aligned} EX_X(P) &= DFT[l_0(k_x,k_y)G_X(k_x,k_y)](P) \\ EX_Y(P) &= DFT[l_0(k_x,k_y)G_Y(k_x,k_y)](P) \\ EX_Z(P) &= DFT[l_0(k_x,k_y)G_Z(k_x,k_y)](P) \end{aligned} \tag{2.49}$$

and Eq. 2.39 as

$$EY_{X,Y,Z}(P) = R_C(DFT[(QY_{X,Y,Z})])(P) \tag{2.50}$$

TH-1501_10612103

The magnetic field components and the resultant electric and magnetic field components for an arbitrarily polarized beam can similarly be written. In comparison with the FFT form it is seen that in the DFT form the electric field and magnetic field components can be computed only at one location, say P near the focus. Thus using the DFT form one can compute the focal field in a narrow region near the focus, however, with an enhanced spatial resolution without computing the data over the entire plane.

2.5.1 Derivation of the length units for the numerically constructed focal volume

The two versions of the Fourier transform form of the vectorial diffraction theory described above computes focal field components in a plane through a point P or at the point P, respectively. Here the distance between two points in the focal volume is denoted in terms of number of pixels. Thus there is a need to convert the distance in terms of number of pixels to real distance units.

To convert the pixels to distance units, we make use of normalized optical co-ordinates. Normalized optical co-ordinates are a natural generalization of the co-ordinates employed frequently in connection with diffraction in a lens system. The optical co-ordinates are defined as

$$\begin{aligned} u &= 4kz\sin^2\alpha/2 \\ v &= kr\sin\theta\sin\alpha = k\sqrt{(x^2+y^2)}\sin\alpha \end{aligned} \tag{2.51}$$

Here u is the optical coordinate along the optical axis, v is the optical coordinate in the transverse direction and the other symbols have their usual meaning. Therefore considering a small increment in u and v

$$\begin{aligned} \Delta v &= k_0\Delta\rho\sin\alpha \\ \Delta u &= 4k_0\Delta z\sin^2\alpha/2 \end{aligned} \tag{2.52}$$

where $\rho = r\sin\theta$. Assuming $\Delta\rho = \Delta z$, we can write

$$\begin{aligned} \frac{\Delta v}{k_0\sin\alpha} &= \frac{\Delta u}{4k_0\sin^2\alpha/2}, \\ \Delta u &= \Delta v \times 2\tan\alpha/2, \end{aligned}$$

TH-1501_10612103

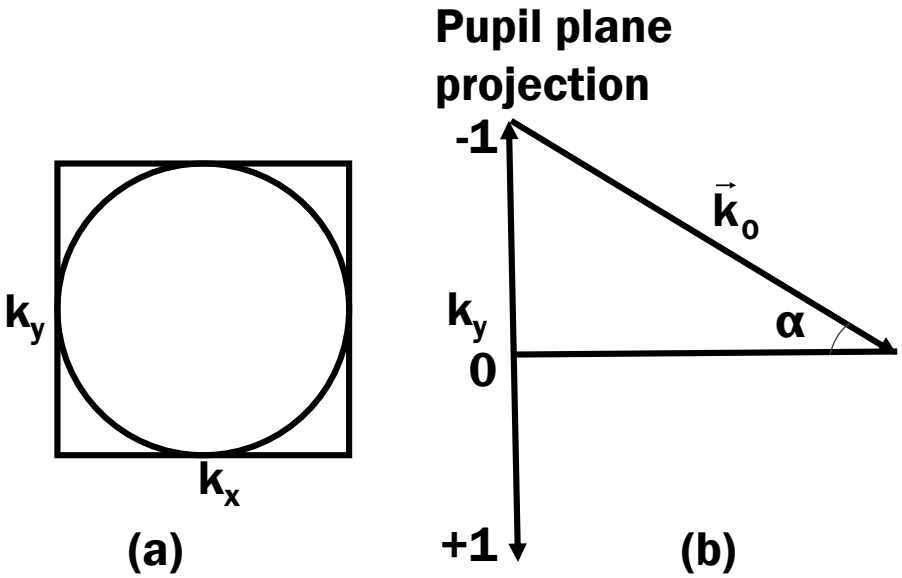

Figure 2.6: Schematic showing (a) the pupil plane and (a) the wavevector orientation for a marginal ray.

Meanwhile from section 2.4.1 we see that the pupil plane has a unit radius in the (kx, ky) plane since $k_0 \sin\alpha = 1$. Hence the values of (k_x, k_y) will vary between -1 and +1 as depicted in Fig. 2.6. Thus writing Fourier transform phase factor in Eq. 2.31 as

$$e^{i(k_x x + k_y y)} = e^{i2\pi(\frac{k_x}{2\pi}x + \frac{k_y}{2\pi}y)} \tag{2.53}$$

we have

$$\Delta v = \Delta N_{pixel} \times \pi. \tag{2.54}$$

Therefore

$$\Delta u = \Delta N_{pixel} \times \pi \times 2\tan\alpha/2 \tag{2.55}$$

where ΔN_{pixel} is the number of pixel to be converted to distance unit. Thus we can express ΔN_{pixel} in the unit of normalized optical coordinates u and v, which can be used in Eqs. 2.52 to obtain the corresponding values in physical distance unit.

2.5.2 Focal field computation in the presence of aberrations

So far in this chapter we have considered computation of electric and magnetic field near the focus when the beam does not have any aberration. In the presence of aberrations the same expressions get modified, as unaberrated pupil function l_0 is to be replaced by $l_0\, e^{i\Phi(x,y)}$, where $\Phi(x, y)$ represents the aberration function.

TH-1501_10612103

Table 2.1: Zernike circular polynomials.

j	$Z_j(x,y)$	Common aberration
4	$\sqrt{3}(2(x^2+y^2)-1)$	Defocus
5	$2\sqrt{6}xy$	primary astigmatism at $\pm$ 45°
6	$\sqrt{6}(x^2-y^2)$	primary astigmatism at 0°
7	$\sqrt{8}(3(x^2+y^2)-2)y$	primary y coma
8	$\sqrt{8}(3(x^2+y^2)-2)x$	primary x coma
9	$\sqrt{8}(3x^2y-y^3)$	primary y trefoil
10	$\sqrt{8}(x^3-3y^2x)$	primary x trefoil
11	$\sqrt{5}(6(x^2+y^2)^2-6(x^2+y^2)+1)$	primary spherical aberration
12	$\sqrt{10}(4(x^2+y^2)-3)(x^2-y^2)$	Secondary astigmatism at $\pm$ 45°
13	$\sqrt{10}(4(x^2+y^2)-3)2xy$	Secondary astigmatism at 0°
14	$\sqrt{10}(4(x^4+y^4)-6x^2y^2)$	Tetrafoil x
15	$\sqrt{10}(4xy(x^2-y^2))$	Tetrafoil y
16	$\sqrt{12}(10(x^2+y^2)^2-12(x^2+y^2)+3)x$	Secondary x coma
17	$\sqrt{12}(10(x^2+y^2)^2-12(x^2+y^2)+3)y$	Secondary y coma
18	$\sqrt{12}(5(x^2+y^2)-4)(x^3-3y^2x)$	Secondary x trefoil
19	$\sqrt{12}(5(x^2+y^2)-4)(3x^2y-y^3)$	Secondary y trefoil
20	$\sqrt{12}(5x(x^2+y^2)^2-4x^5-20y^2x^3)$	Pentafoil x
21	$\sqrt{12}(5y(x^2+y^2)^2-4y^5-20x^2y^3)$	Pentafoil y
22	$\sqrt{7}(20(x^2+y^2)^3-30(x^2+y^2)^2$ $+12(x^2+y^2)-1)$	Secondary spherical aberration

In this thesis, the aberration present in a beam will be expressed as a linear combination of orthogonal Zernike circular polynomials [21, 39], such that $\Phi(x,y) = \sum(\phi_{rms})_i Z_i$. Here ϕ_{rms} is RMS (root mean square) amplitude of aberration and Z_i is the single index Zernike polynomial. Zernike polynomials form a complete set of polynomials in two variables, (r,θ) or (x,y), and are orthogonal to one another over the interior of a unit circle. It is important to note that the Zernike modes are orthogonal only in a continuous fashion over the area, and in general they will not be orthogonal over a discrete set of data points within a unit circle. Table 2.1 shows a list of Zernike polynomials expressed using Cartesian coordinates which represent a few important monochromatic aberrations.

TH-1501_10612103

2.6 Conclusion

In this chapter we have introduced vectorial diffraction theory that is needed to compute the Cartesian components of the electric and magnetic fields near the focus of a beam. We began with the theory of Richards and Wolf and showed how this integral form can be converted to a Fourier transform form. We showed two versions of the Fourier transform form of the vectorial diffraction theory. We have also developed the expressions to convert the pixel units associated with the numerical computation to real distance units. We then showed how the focal field expressions get modified in the presence of aberrations present in the beam. It is to be noted that the same theoretical expressions, discussed in this chapter, can be used to compute the focal volume properties of any focusing system, having a numerical aperture ranging from low to high. Also for many applications such as optical trapping, the focusing medium is inhomogeneous. Nevertheless the focal field expressions developed in this chapter will be useful to compute some generalized properties near the focus, such as the various trapping forces, even for the above applications.

TH-1501_10612103

Chapter 3

Aberration effects on the azimuthally polarized beam

3.1 Introduction

As mentioned previously an azimuthally polarized beam has important properties in the focal volume. When focused by an unaberrated lens system, it produces a doughnut shaped intensity distribution in the focal plane [40, 41]. Azimuthally polarized beams have non diffracting and self healing properties [42] and when used as the pump beam it reduces transmission loss in the waveguide in comparison to a linearly or radially polarized pump beam [19]. Such doughnut shaped patterns can act as the erase beam in optical super resolution microscopy [43, 44]. These beams have also been shown to be useful in creating optical traps [45] for three-dimensional (3D) manipulation of the trapped particles. Pulsed azimuthally polarized beam can drills holes in certain kind of metals more efficiently as compared to linearly or circularly polarized beams [17].

In all the above stated applications, the azimuthally polarized beams are assumed to be free of any aberrations. Therefore whether the important properties of the beam are effected by the presence of small to moderate amount of common optical aberrations or not, is of significant interest in so far as the applications of the beam are concerned.

There are number of reports about the effect of primary aberrations on the azimuthally polarized beam [26, 28, 46, 47], however, these studies are mostly limited to the focal plane. There are also reports on the study of the effect of thermally

TH-1501_10612103

induced aberrations [48] and effect on irradiance and polarization properties of the beam as it propagates through a turbulent atmosphere [49]. Unfortunately there is no comprehensive study on the effect of the aberrations on the properties in the entire focal volume of an azimuthally polarized beam. Such studies are expected to reveal some non-trivial and so far unknown behavior of the azimuthally polarized beam. In this chapter we are interested to see how the focal volume properties of an azimuthally polarized beam change in the presence of the most commonly encountered monochromatic aberrations. Thus we present here detailed theoretical investigation on the effect of primary aberrations on the focal volume properties of an azimuthally polarized beam. This chapter also presents experimental results which verify the theoretical results for a low NA lens system.

3.2 Numerical simulation

We first investigate the effect of primary aberrations on the focal volume properties of an azimuthally polarized beam by considering a focusing lens of numerical aperture 0.9. Here we used Zernike polynomials [21] representing primary aberrations, such as astigmatism, coma, trefoil and spherical aberration, which are discussed in section 2.5.2 and are shown in the table 2.1 of chapter 2. In this investigation electric and magnetic field components in a focal volume, extending from -2λ to 2λ along X, Y and Z axes with origin of the coordinate system as the nominal focus, are computed. The Jones matrix representation of an unaberrated azimuthally polarized beam can be written as

$$\begin{pmatrix} -\sin\phi \\ \cos\phi \end{pmatrix}$$

where ϕ is the azimuthal angle in the pupil plane. The computational steps needed for the investigation has already been discussed in chapter 2. Throughout this thesis we use the notations I_x, I_y and I_z to indicate the time-averaged electric energy densities or intensity distributions due to the X polarized, Y polarized and Z polarized fields, respectively. Figure 3.1 shows the intensity distributions of an azimuthally polarized beam (a) I_x, (b) I_y, and (c) $I_x + I_y$ in the XY plane and (d) $I_x + I_y$ in the XZ plane in the aberration free case. Again throughout the thesis the XY plane will represent the focal plane with the nominal focus as the origin, and the XZ or YZ plane will represent a plane passing through the optical (i.e. Z) axis and the X or Y axis, respectively with the nominal focus as the origin. The intensity

TH-1501_10612103

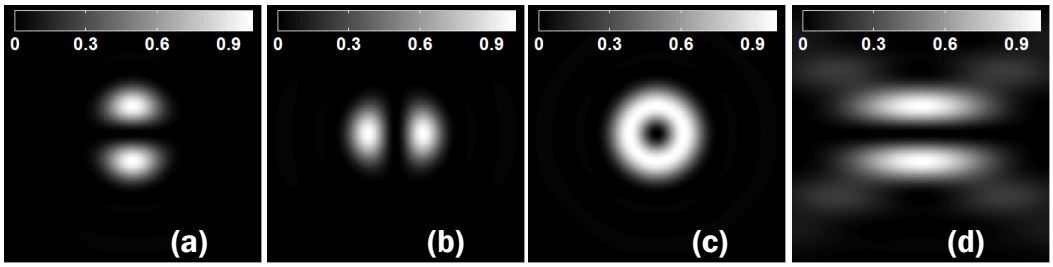

Figure 3.1: Normalized intensity distributions (a) I_x, (b) I_y, (c) $I_x + I_y$ in the XY plane and (d) $I_x + I_y$ in the XZ plane of an azimuthally polarized beam in the aberration free case. Every image has different peak intensity, which is indicated at its top by the horizontal color bar.

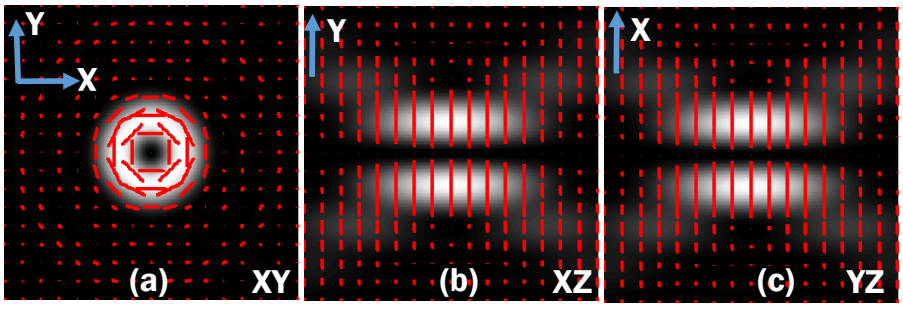

Figure 3.2: Polarization profile of an azimuthally polarized beam in the (a) XY, (b) XZ and (c) YZ planes. Polarization ellipses are overlaid on the normalized total intensity distributions in the corresponding plane, in the aberration free case.

distributions, due to the X polarized, or Y polarized fields and the total field in the presence of aberrations as well as in the aberration free case, are normalized by the maximum value of the total intensity in the aberration free case. In the case of an unaberrated azimuthally polarized beam, it is noticed that the focal plane contains both the X and Y polarized components, while in the XZ and YZ planes only Y or X polarized component is present. However the presence of Z polarized component in the focal volume in the entire range of numerical aperture is negligible. As expected the total intensity distribution of an azimuthally polarized beam in the focal plane has a ring like structure, thus having a circular symmetry about the optical axis.

3.2.1 Polarization profile near the focus

Besides the energy density, the polarization near the focus is one of the important properties of tightly focused vector beams. As light gets focused not just to a point

TH-1501_10612103

but to a diffraction limited volume, one must know the polarization property of the beam at every point in the focal volume. Below we discuss the representation of the polarization profile near the focus as adopted in this chapter.

Since the electric field components E_x, E_y and E_z are in general complex numbers, we can write,

$$E_{x,y,z}(P) = e_{x,y,z}(P)e^{i\psi_{x,y,z}(P)} \tag{3.1}$$

where $e_{x,y,z}(P)$ are the amplitudes and $\psi_{x,y,z}(P)$ are the phase angles of the electric field components at P. Incorporating the harmonic time dependence we can write

$$E_{x,y,z} = e_{x,y,z}e^{i(\psi_{x,y,z}+\omega t)} \tag{3.2}$$

The time dependence of the resultant electric field can be illustrated by drawing an ellipse, referred to as polarization ellipse, using instantaneous values of E_x, E_y and E_z. The polarization ellipse thus can indicate how the orientation of the resultant electric field changes as the time evolves.

Since the applications of the azimuthally polarized beam exploit the azimuthal symmetry of the polarization profile near the focus, hence it will be important to know how the common optical aberrations effect the polarization profile of the beam. Therefore in this chapter we have also investigated the time evolution of the net electric field in the entire focal volume of the azimuthally polarized beam, in the aberration free case as well as in the presence of various primary aberrations. To show the polarization profile we used two dimensional polarization ellipses. The electric field components computed are complex, which can be expressed as the product of a real valued amplitude and $e^{i\psi}$ where ψ is the phase angle. We draw the polarization ellipses by using the real amplitude and the phase values of the X polarized and Y polarized electric field components at every location in the XY, XZ and YZ planes. Figure 3.2 show the polarization profiles of an azimuthally polarized beam in the aberration free case in the (a) XY, (b) XZ and YZ planes. The polarization profiles are overlaid on the normalized total intensity distributions in the respective planes. In all the images, the top left corner shows the axes of the polarization ellipses. It is noticed that in the aberration free case in the XY, XZ and YZ planes, the light has linear polarizations. In the focal plane, the polarization profile has a circular symmetry and the electric field points in the azimuthal direction.

TH-1501_10612103

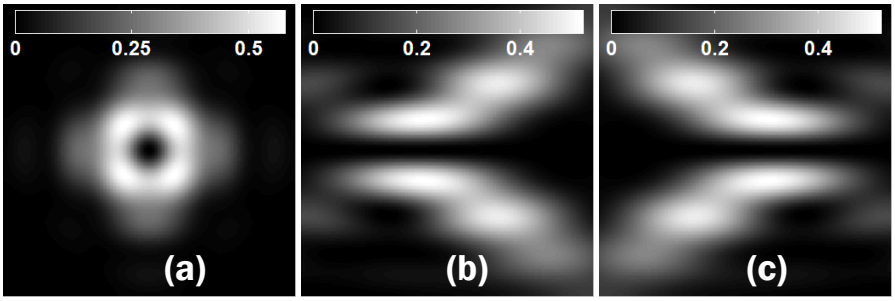

Figure 3.3: Normalized intensity distributions I_x, I_y and $I_x + I_y$ of an azimuthally polarized beam in the presence of astigmatism at 0° with RMS amplitude 1 radian in the (i) XY, (ii) XZ and (iii) YZ planes. Every image has different peak intensity, which is shown at its top by the horizontal color bar.

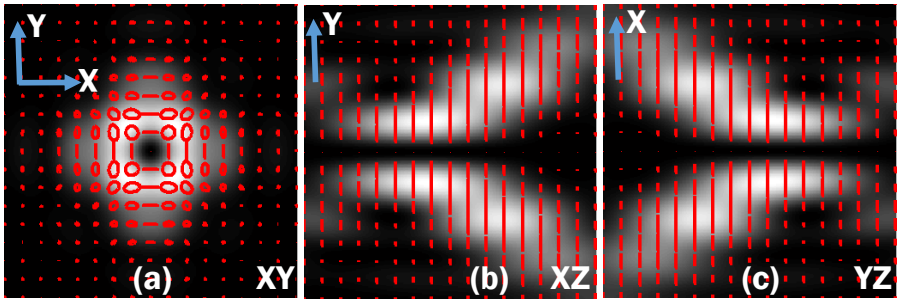

Figure 3.4: Polarization profile of an azimuthally polarized beam in the presence of astigmatism in the (a) XY, (b) XZ and (c) YZ planes. Polarization profiles are overlaid on the normalized total intensity distributions in the corresponding plane.

3.2.2 Effect of astigmatism

We again compute the Cartesian components of the electric field near the focus of an azimuthally polarized beam after introducing ϕ_{rms}=1 radian of astigmatism at 0° in the pupil plane. Figure 3.3 shows the resulting focal intensity distribution $I_x + I_y$ in the (a) XY, (b) XZ and (c) YZ planes, respectively. It is noticed that the circular symmetry of the intensity distribution in the focal plane is distorted, although there still exists a dark centre coincident with the nominal focus. In the XZ and YZ planes the intensity distributions maintain planar symmetry with respect to the optical axis. Even in the presence of astigmatism it is noticed that there is no light along the optical axis and the dark centre is surrounded by intense light over all the axial planes. If we apply aberration with opposite sign of ϕ_{rms} of the same magnitude, there occurs an interchange in the intensity distributions between

TH-1501_10612103

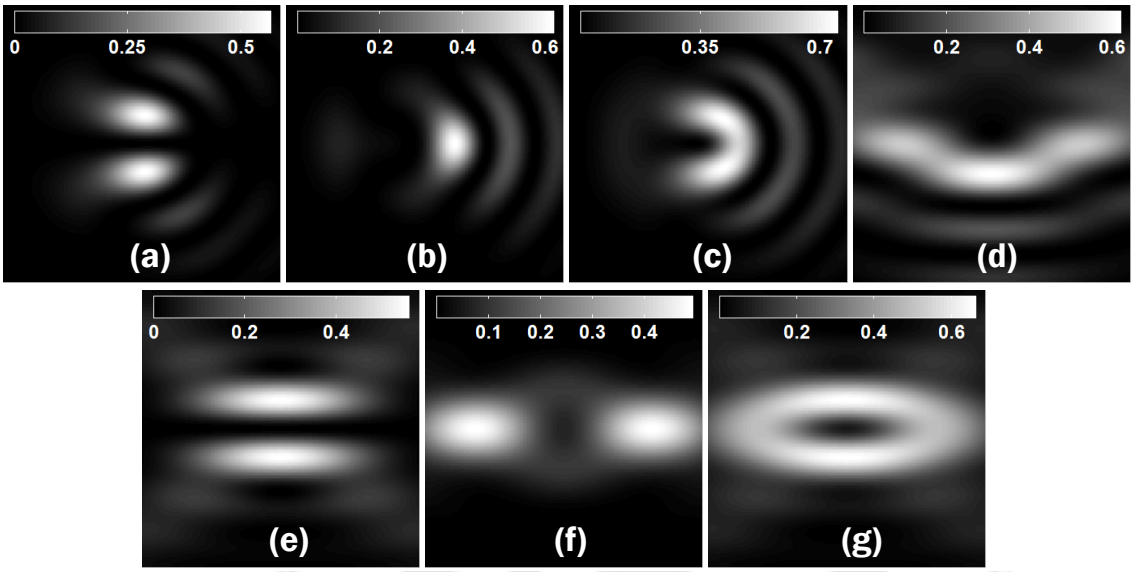

Figure 3.5: Normalized intensity distributions I_x, I_y and $I_x + I_y$, respectively, of an azimuthally polarized beam in the presence of coma with ϕ_{rms}=1 radian, (a-c) in the XY and (e-g) YZ planes, and (d) $I_x + I_y$ in the XZ plane. Every image has different peak intensity, which is shown at its top by the horizontal color bar.

the XZ plane and the YZ plane. Figure 3.4 shows the polarization ellipses near the focus of the azimuthally polarized beam in the (a) XY, (b) XZ and (c) YZ planes in the presence of ϕ_{rms}=1 radian of astigmatism. The ellipses are overlaid on the normalized total intensity distributions of the corresponding plane. It is noticed that in the presence of astigmatism circular symmetry of the polarization profile in the focal plane is distorted and there results in circular and elliptical polarizations in addition to linear polarization. On the other hand in the XZ and YZ planes the polarization is linear.

3.2.3 Effect of coma

Figure 3.5 shows the intensity distributions I_x, I_y and $I_x + I_y$ of an azimuthally polarized beam in the presence of ϕ_{rms}=1 radian of coma (a-c) in the XY plane and (e-g) in the YZ plane, and (d) $I_x + I_y$ in the XZ plane. It is noticed that the effect of coma is more on the Y polarized intensity than the X polarized intensity in the focal volume. The effect on the Y polarized component results in an asymmetry in the total intensity distribution in the focal plane. It is also seen that the intensity distribution in the XZ plane exists only on one side of the optical axis. There exists

TH-1501_10612103

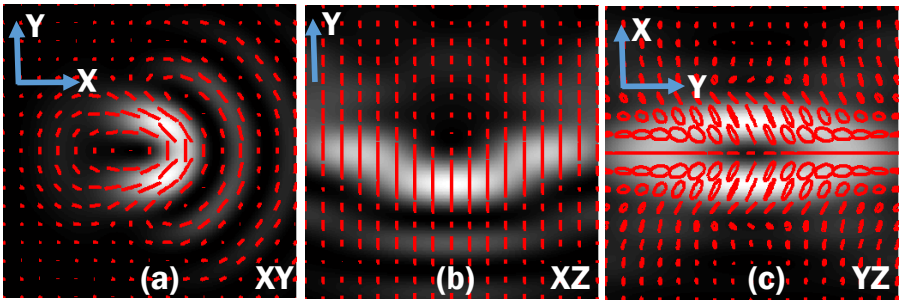

Figure 3.6: Polarization profile of an azimuthally polarized beam in the presence of coma in the (a) XY, (b) XZ and (c) YZ planes for ϕ_{rms}=1 radian. Polarization ellipses are overlaid on the normalized total intensity distributions in the corresponding plane.

two maxima of the y polarized intensity at two locations on the optical axis in the YZ plane situated symmetrically with respect to the focus. This intensity distribution due to the Y polarized component combines with the X polarized component to contribute to the total intensity distribution in the YZ plane having a dark centre surrounded by intense light.

Figure 3.6 shows the polarization profile of the azimuthally polarized beam in the presence of coma with ϕ_{rms}=1 radian, in the (a) XY, (b) XZ and (c) YZ planes. The polarization ellipses are overlaid on the normalized total intensity distributions of the corresponding planes. Here we have observed that in the presence of coma, circular symmetry of the polarization profile in the focal plane is distorted, although light in the focal plane still has linear polarization. Besides the light in the XZ plane also has linear polarization, although in the YZ plane the intensity distribution has elliptical polarization.

3.2.4 Effect of trefoil

Figure 3.7 shows the intensity distributions (a) I_x, (b) I_y, (c) I_x+I_y in the XY plane, and I_x+I_y in the (d) XZ and (e) YZ planes near the focus of an azimuthally polarized beam in the presence of ϕ_{rms}=1 radian of x trefoil. It is observed that trefoil distorts the circular symmetry of the intensity distribution in the focal plane, although there exists a dark centre co-incident with the nominal focus. The focal intensity distributions in the XZ and YZ planes indicate that the intensity distribution in the transverse planes away from the focal plane have a profile similar to the same in the focal plane. Thus there exist no light on the optical axis and the axis is

TH-1501_10612103

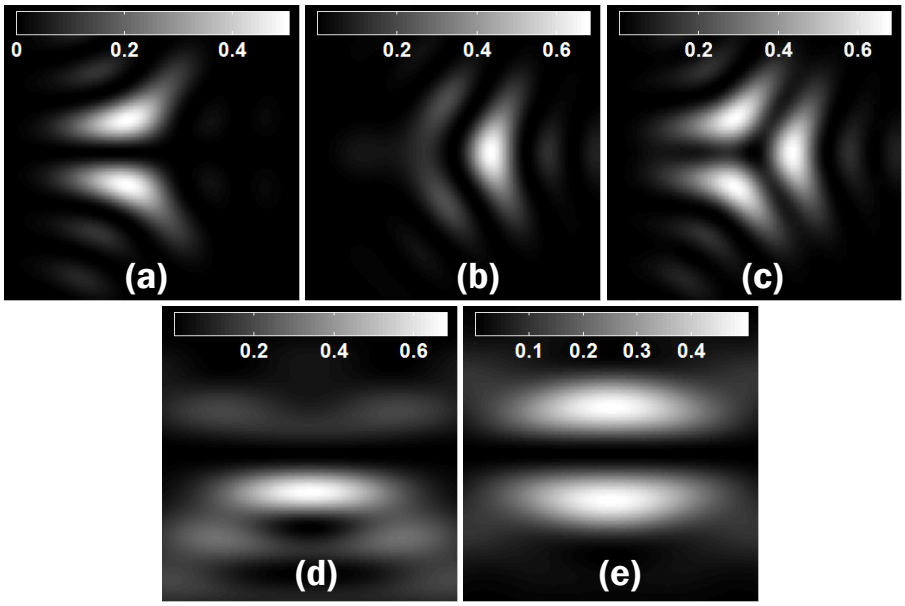

Figure 3.7: Normalized intensity distributions (a) I_x, (b) I_y, (c) $I_x + I_y$ in the XY plane, $I_x + I_y$ in the (d) XZ and (e) YZ planes of an azimuthally polarized beam in the presence of trefoil with ϕ_{rms}=1 radian. Every image has different peak intensity, which is shown at its top by the horizontal color bar.

surrounded by light distribution having discontinuity at three locations. Figure 3.8 shows the polarization profile of the beam in the (a) XY, (b) XZ and (c) YZ planes of the focal volume, in the presence of trefoil with ϕ_{rms}=1 radian. The polarization ellipses are overlaid on the normalized total intensity distribution profiles in the corresponding plane. As observed, in the presence of trefoil the circular symmetry of the polarization profile in the focal plane is distorted, although the polarization still remains linear. However in the XZ and YZ planes it has linear and elliptical

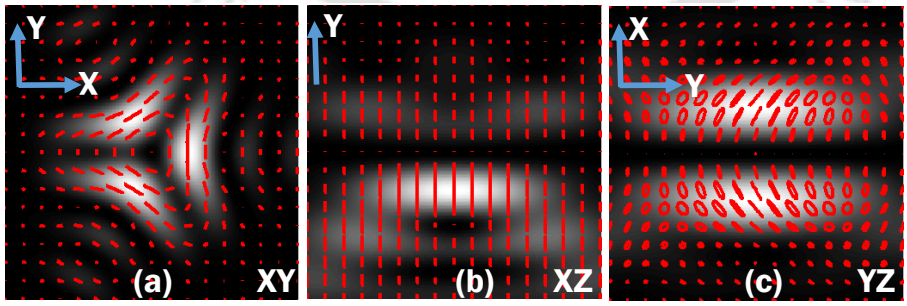

Figure 3.8: Polarization profile of an azimuthally polarized beam in the presence of trefoil in the (a) XY, (b) XZ and (c) YZ planes. Polarization ellipses are overlaid on the normalized total intensity distributions in the corresponding plane.

TH-1501_10612103

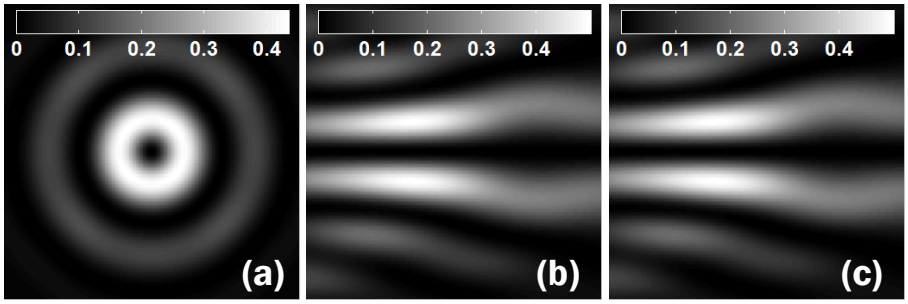

Figure 3.9: Normalized intensity distribution $I_x + I_y$ of an azimuthally polarized beam in the presence of spherical aberration with ϕ_{rms}=1 radian in the (a) XY, (b) XZ and (c) YZ planes. Every image has different peak intensity, which is shown at its top by the horizontal color bar.

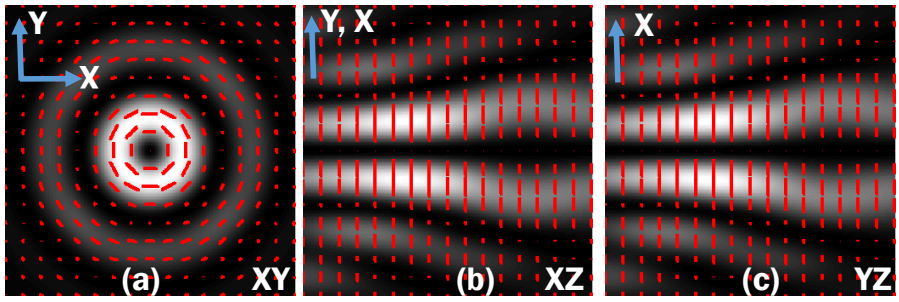

Figure 3.10: Polarization profile of an azimuthally polarized beam in the presence of spherical aberration in the (a) XY, (b) XZ and (c) YZ planes. Polarization ellipses are overlaid on the normalized total intensity distribution in the corresponding plane.

polarization profiles, respectively.

3.2.5 Effect of spherical aberration

Figure 3.9 shows the intensity distribution $I_x + I_y$ of an azimuthally polarized beam in the (a) XY, (b) XZ and (c) YZ planes, respectively, of the focal volume, in the presence of ϕ_{rms}=1 radian of spherical aberration. Here we can see that in the presence of spherical aberration there is no considerable change in the intensity distribution in the focal plane as it remains circularly symmetric with a dark centre at the nominal focus. The intensity distributions in the XZ or YZ plane indicate that there exist no light on the optical axis and light distribution has cylindrical symmetry about the optical axis. However as one goes along the optical axis the radius of the circular ring pattern gradually increases. The corresponding polarization profile of the beam in the presence of spherical aberration is shown in Fig. 3.10

TH-1501_10612103

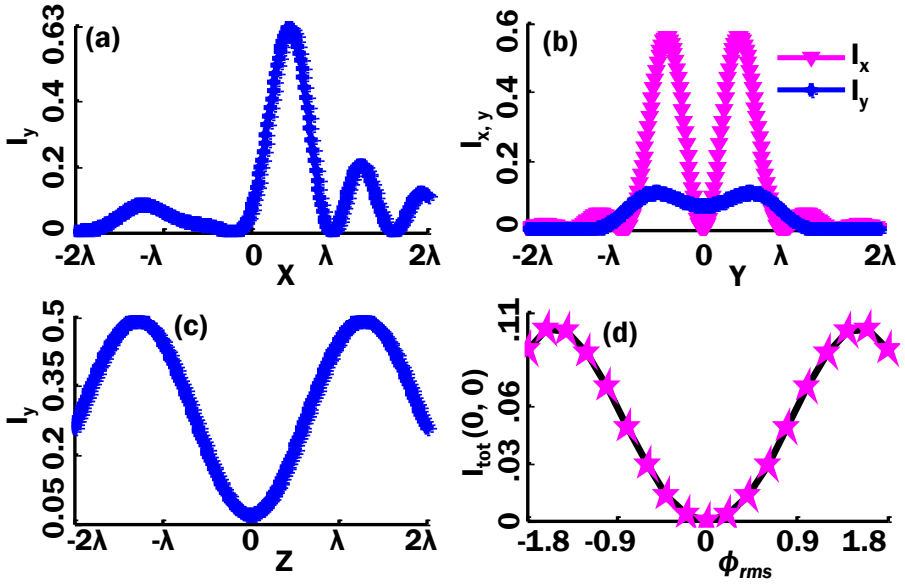

Figure 3.11: Line plots of the normalized intensity distributions I_x and I_y of an azimuthally polarized beam in the presence of coma with ϕ_{rms}=1 radian along (a) X, (b) Y and (c) Z axes, (d) variation of the intensity at the focus with ϕ_{rms} varying between -1.8 to 1.8. Intensity plots are normalized by the maximum value of intensity in the XY plane in the aberration free case.

which shows polarization profiles in the (a) XY, (b) XZ and (c) YZ planes. The polarization ellipses are overlaid on the normalized total intensity distributions of the corresponding plane. Here we have observed that in the XY, XZ and YZ planes of the focal volume, the azimuthally polarized beam has linear polarization. Owing to the symmetry of the spherical aberration such behavior will be observed on any plane parallel to the optical axis and containing the optical axis.

3.2.6 Generation of a boat-shaped beam

If we consider the intensity distribution in the XZ and YZ planes near the focus of an azimuthally polarized beam in the presence of coma, we may see that the dark centre near the focus is surrounded by light in all but one direction. Thus it indicates the formation of boat-shaped intensity distribution in the presence of coma [50]. Recently there have been a lot of interests in the light beams with a 3D dark spot, that is, a relatively dark centre surrounding by light in all directions. A dark spherical spot [51] is created using a 4π arrangement of two counter propagating radially polarized beams. Such a dark spot, when used in a STED (stimulated emission depletion) microscope [52], can provide uniform resolution enhancements

TH-1501_10612103

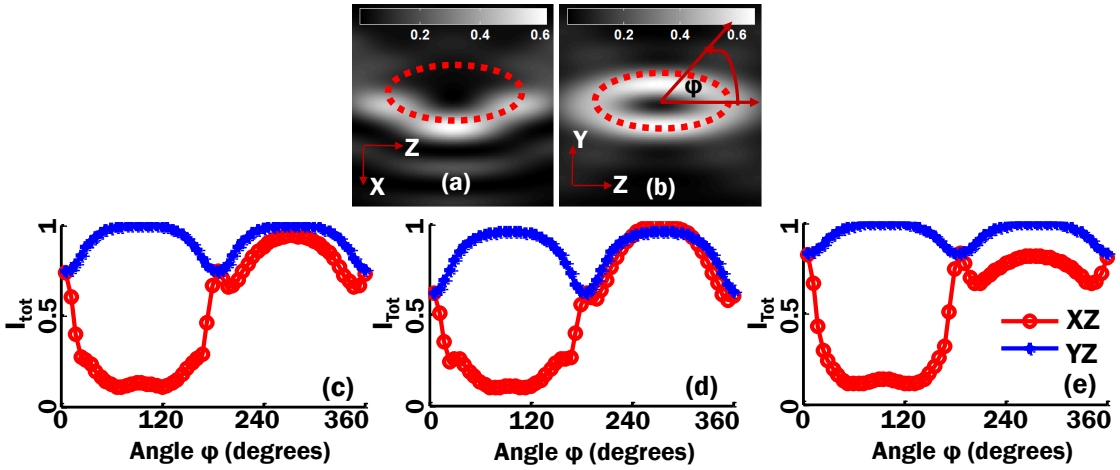

Figure 3.12: Intensity maxima locations (represented by the red dots) along the circumference of the boat-shaped beam in the (a) XZ and (b) YZ planes obtained from a coma aberrated azimuthally polarized beam with ϕ_{rms}=1 radian, The plots of the intensity values corresponding to the red dots vs φ in XZ and YZ planes in the presence of coma with ϕ_{rms} equal to (c) 1 radian, (d) 0.9 radian and (e) 1.1 radian.

in both transverse and axial directions. It has been demonstrated that a focal spot comprising a dark centre surrounded by a bright ring can provide an efficient optical trap for particles having refractive index lower than the surrounding medium [51, 53]. Realizing their importance especially in super-resolution microscopy and optical trapping, a number of schemes, to generate 3D dark spots or volumes, have been proposed. Many such schemes do not require the 4π arrangement of two microscope objectives, as aligning two counter propagating beams is always a challenging task. Some of such examples, where only one objective lens is needed, are the generation of optical bottle beams [54], and generation of spherical dark spots [55, 56, 57]. In these schemes two cylindrically polarized beams with custom defined pupil functions are overlapped, before being focused by the objective lens, to generate the desired focal volume.

The boat-shaped focal intensity distribution presented in this chapter can be achieved with a relatively simple arrangement involving one objective lens and without the need to overlap two beams. Unlike the 3D dark spots where a relatively dark region is surrounded by light from all six sides, such as, top, bottom, left, right, front and back, in the case of the proposed beam an axially elongated dark region is surrounded by light from five sides only. The dark volume of the boat shaped beam has a V-shaped cross section in the XZ plane. Taking a note that the direction of

TH-1501_10612103

the resultant electric field constituting the beam may be an important parameter in the prospective applications of the beam, in this work, we have also drawn the polarization ellipses over the entire focal volume.

To further investigate the formation of the boat-shaped intensity distribution, the X polarized and Y polarized intensities are plotted along X, Y and Z axes and are shown in Figs. 3.11 (a-c). It is noticed that along the X axis there exist only Y polarized component and is asymmetric with respect to the focus. Along Y axis both the X polarized and Y polarized intensities exist. Along Z axis there exists two intensity maxima at $\pm$ 1.3λ with respect to the focus. We also plotted the net intensity at the origin against the RMS amplitude varying from -1.8 radian to 1.8 radian and is shown in figure 3.11 (d). The central intensity value increases with ϕ_{rms} and become maximum at ϕ_{rms}=$\pm$1.6. Further increase in the RMS amplitude results in decrease in the central value of intensity. It is to be noted that at ϕ_{rms}=1 radian, the central intensity value is 0.05, indicating that the centre is only relatively dark.

In order to confirm the formation of the boat-like shape, we have considered the total intensity distributions in the XZ and YZ planes and are overlaid by red dots as shown in Figs. 3.12 (a) and (b). These red dots represent the location of the maximum intensity along a line joining the centre of the boat-shaped structure and the red point. The orientation of the line is also represented by the angle φ between the line and the horizontal axis. We have considered the maximum values of intensities along lines having angular separation of 6°, over a range of φ varying from 0 to 360°. Figures 3.12 (c), (d) and (e) show the plots of intensity maxima vs the angle φ in the XZ and YZ planes for RMS amplitude values of aberration 1, 0.9 and 1.1 radian, respectively. For each value of RMS amplitude, maximum intensity plots are normalized by the maximum of total intensity in the respective planes. It is seen that in the case of all the plots, in the first half portion (i.e. φ= 0 to 180°) of the XZ plane, the intensity maximum values are approximately zero while in the YZ plane the intensity maxima are relatively large. From Fig. 3.12 (c) it is noticed that on the optical axis of the focusing lens, the maximum intensity in the YZ planes reduces to $\sim$ 22% of the maximum. Also the maximum intensity values in the XZ plane are $\sim$ 9% smaller than the same in the YZ plane. We have further obtained plots similar to Fig. 3.12 (c), using ϕ_{rms}=0.9 rad and 1.1 rad and the same are seen in Figs. 3.12 (d) and (e), respectively. It is observed that in the presence of ϕ_{rms}= 0.9 rad, the maximum intensity values in the YZ and XZ planes are comparable,

TH-1501_10612103

while variation in the maximum intensities in the XZ plane increases to $\sim$ 30%. This variation gets reduced to $\sim$ 15% if we choose ϕ_{rms} = 1.1 rad, however, the same leads to a rise in the difference between the XZ plane maximum values and the YZ plane maximum values.

3.3 Experimental generation of cylindrical vector beams focused by a low NA lens

In the literature several reports are available which discuss the experimental generation of radially or azimuthally polarized beams. These beams can be generated by taking the superposition of two orthogonally polarized TEM_{01} modes [58]. Pure radially or azimuthally polarized beam can also be generated by passing a pair of right handed and left handed circularly polarized beams through a helical phase plate [59] or by passing linearly polarized beam through a liquid crystal based polarization converter [60]. However these methods can only generate a fixed type of vector beam. To generate cylindrical vector beams with user defined aberration profile in its pupil plane we require a dynamic vector beam forming arrangement such as a liquid crystal spatial light modulator (LCSLM) based arrangement. Most of the existing methods to generate arbitrary vector beams require the light to pass through two LCSLMs, one after the other [61], or gratings. Instead of using two LCSLMs one may make the light beam to pass through a single LCSLM twice [62, 63]. An arbitrary vector beam can also be generated using a single LCSLM in combination with a Wollaston prism [64]. However most of the arbitrary vector beam forming techniques involving one or two LCSLMs suffer from a serious limitation due to the damage threshold [65] of power of the LCSLM panel which puts an upper limit on the power of the vector beam generated. We have recently demonstrated a division of wavefront based arbitrary vector beam forming setup [66] that involves only one LCSLM. The arrangement permits generation of cylindrical vector beam with a user defined phase profile and power of the beam can, in principle, be raised to the highest value possible with an LCSLM based setup.

3.3.1 Brief description of the experimental setup

In our scheme we use computer generated holography technique [67, 68] and binary amplitude holograms to generate the cylindrical vector beams. If a collimated laser

TH-1501_10612103

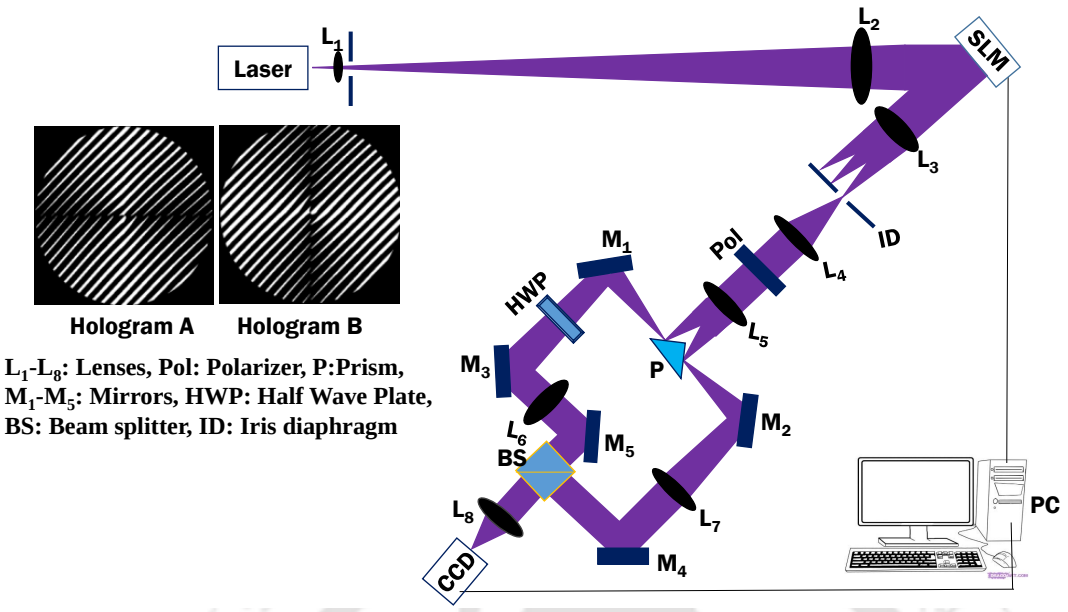

Figure 3.13: Experimental setup to generate arbitrary vector beams.

beam is incident on such holograms, they give rise to diffracted beams of orders 0, ± 1, ± 2, $\pm 3 \cdots$. The holograms are designed in a way that the diffracted beams of different orders are well separated from one another and the $+1$ order diffracted beam carries a user defined amplitude and phase profile. The LCSLM panel displays two binary holograms side by side and each hologram gives rise to a well defined linearly polarized amplitude and phase profile. The experimental arrangement then facilitates a 90° rotation of the polarization of one of the two diffracted beams. The two orthogonally polarized beams are then superimposed to generate an arbitrary vector beam.

A schematic diagram of the experimental arrangement to generate arbitrary vector beam is shown in Fig. 3.13. The beam of wavelength λ=632.8 nm from a He-Ne laser is focused by the lens L_1 on a pinhole PH. The pinhole selects the central portion of the beam and the diverging beam is collimated by the lens L_2. LCSLM is positioned in such a way that the collimated laser beam is incident on its display panel almost perpendicularly. Two binary holograms are displayed on the LCSLM panel, which can be reconfigured in real time by a computer program running in a PC. The two holograms are positioned horizontally close to one another as shown in the inset in Fig. 3.13, which are referred to as hologram A and hologram B. The hologram A is designed to generate a complex amplitude profile corresponding to X

TH-1501_10612103

(horizontally or p) polarized pupil plane of the vector beam and the hologram B is designed to generate the same for the Y (vertically or s) polarized pupil plane. The diffracted beam from the LCSLM contains many diffracted orders, whose direction can be controlled by using a tilt function incorporated in the two holograms. The diffracted beams are collected by lens L_3 followed by an iris diaphragm kept at the focal plane of Lens L_3. The iris diaphragm isolates the two +1 order beams from the rest and the two are then re collimated using lens L_4. A polarizer (pol) is optionally kept in the beam path to ensure that the both +1 order beams are s polarized. The two beams are then focused by the lens L_5 on a right angled prism P such that the beam from hologram A is directed to towards plane mirror M1 and the beam from hologram B is directed towards plane mirror M2. The beam reflected by M1 then passes through a half wave plate that rotates the incident polarization by 90° to make the emergent beam p polarized, which is reflected from the mirror M_3. The beam then gets collimated due to the lens L_6 and the same gets reflected from the mirror M_5. The reflected beam by M_5 being p polarized is then transmitted by the polarizing beam splitter PBS to be incident on the entrance of the lens L_8. The other +1 order beam reflected by the mirror M_2 is then collimated using the lens L_7 and gets reflected by mirror M_4 to incident on PBS. Since this beam is s polarized, it is reflected by the PBS towards the entrance pupil of the lens L_8. The lens pairs L_3 and L_4, L_5 and L_6, and L_5 and L_7 constitute three 4f relay systems, so that the plane of the LCSLM display panel and the entrance pupil of the lens L_8 are conjugate to one another. Therefore the +1 order beam originating from hologram A gives rise to the X polarized pupil and the same from hologram B gives rise to the Y polarized pupil at the entrance pupil of the lens L_8 to produce the desired arbitrary vector beam. The vector beam is then focused by lens L_8 on a CCD camera which is connected to the PC. The optical paths travelled by the two +1 order beams till they reach the PBS are kept approximately equal so that the two beams remain mutually coherent. Further the tilts of the mirrors and PBS are to be aligned to ensure that both the hologram planes are parallel to the plane of the entrance pupil.

Each of the two holograms is described over a circular area of diameter equal to 512 LCSLM pixels having width equal to 8.1 μm. The arrangement of lenses in the beam path between the LCSLM plane and the lens L_8 provides a beam diameter of 3.4 mm at the entrance pupil of L_8. The focal length of L_8 is 300 mm so that the effective numerical aperture (NA) of the lens focusing the vector beam is

TH-1501_10612103

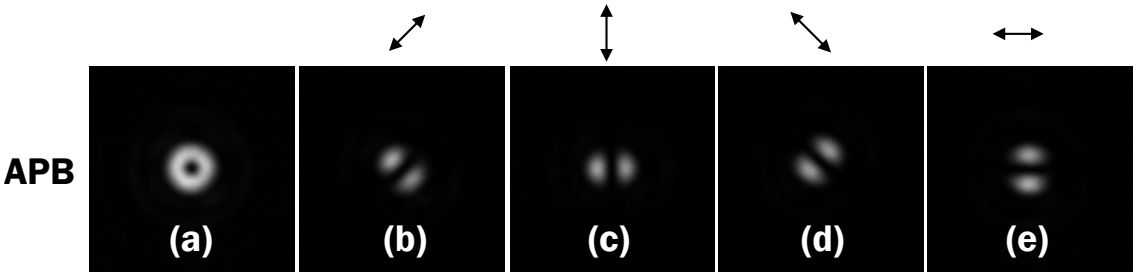

Figure 3.14: Intensity distribution of an azimuthally polarized beam at different orientations of the analyzer.

0.0056. Therefore the setup corresponds to low NA focusing of the beam where the well known displacement theorem [30] is applicable. According to the displacement theorem, the addition of defocus into the beam will not change the three dimensional intensity distribution near the focus barring a shift of the entire intensity distribution axially along +ve or -ve Z direction, depending on the polarity, and by an amount depending on the magnitude of defocus. In this work we thus incorporate specific amount of defocus, represented by Zernike mode Z_4, into the pupil plane of the cylindrical vector beam in order to capture the intensity distributions in different planes parallel to the focal plane and away from the focus, by keeping the CCD camera stationary at the nominal focal plane of an unaberrated beam. It is found that in the present arrangement, incorporation of Z_4 with ϕ_{rms}=$\pm$0.043 radian leads to an axial shift of $\pm$935 μm along the optical axis.

3.3.2 Results and discussion

We configure our experimental arrangement to capture the resultant intensity distributions in a focal volume described by (Δu, Δv) = (38, 38) with the nominal focus as the centre of the volume. The physical distances corresponding to Δu, and Δv can be calculated using Eq. 2.52 of chapter 2 considering NA=0.0056 (which is the NA of the focusing lens in our experimental arrangement). For all the experiments reported in this thesis, both in unaberrated and aberrated cases, our results refer to this focal volume.

We first use our setup to record the intensity distribution in the nominal focal plane of an unaberrated azimuthally polarized beam. In our experimental setup we have the option of using an analyzer which allows capturing of intensity distributions corresponding to different polarization angles. Figure 3.14 shows the experimental

TH-1501_10612103

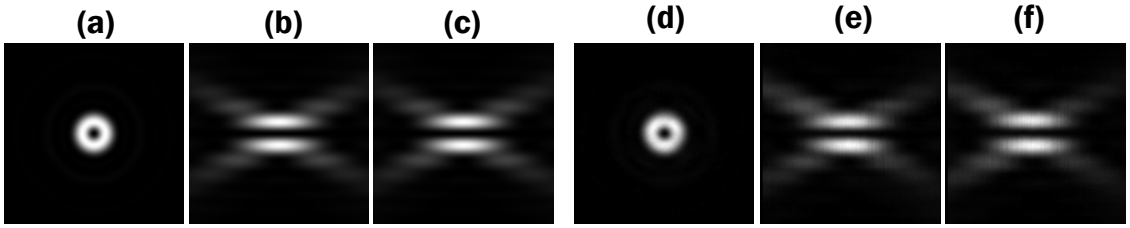

Figure 3.15: Resultant intensity distributions of azimuthally polarized beam in the XY, XZ and YZ planes, respectively, obtained (a→c) theoretically and (d→f) experimentally in the aberration free case.

images representing the focal intensity distribution (a) without the analyzer and (b→e) for different orientations, as indicated above each image, of the analyzer. Rotation of the intensity pattern with the rotation of the analyzer clearly indicate the generation of an azimuthally polarized beam. In parallel with the experiment we also compute the intensity distributions I_x, I_y and I_z numerically using NA=0.0056 in the expressions developed in chapter 2. We record the intensity distribution in the entire focal volume of an unaberrated azimuthally polarized beam and the same is also computed numerically. The intensity distribution without any polarizer in front of the CCD has a doughnut like structure. Figures 3.15 (a→c) show the intensity distributions in the XY, XZ and YZ planes obtained theoretically while Figs. 3.15 (d→f) show the corresponding images obtained experimentally. In order to experimentally demonstrate the effect of primary aberrations on an azimuthally polarized beam using our setup, we then modify the two holograms to incorporate 1 radian RMS of various primary aberrations to each of the X polarized and Y polarized pupil planes of the azimuthally polarized beam. The primary aberration comprises astigmatism, coma, trefoil, and spherical aberration, represented by single index Zernike modes $Z_{5,7,9}$ and Z_{11}. The intensity distributions in the XY, XZ and YZ planes in the presence of each aberration are captured with the CCD and same are also computed numerically. Figure 3.16 shows the total intensity distributions in the (a) XY, (b) XZ and (c) YZ planes obtained theoretically and in the (d) XY, (e) XZ and (f) YZ planes obtained experimentally. The rows (i→iv) of Fig. 3.16 correspond to an azimuthally polarized beam in the presence of astigmatism, coma, trefoil and spherical aberration, respectively. It is noticed that the theoretically obtained intensity distributions agree quite well with the experimental intensity distributions near the focus of the aberrated azimuthally polarized beam.

From our experimental results corresponding to the coma aberrated beam, we

TH-1501_10612103

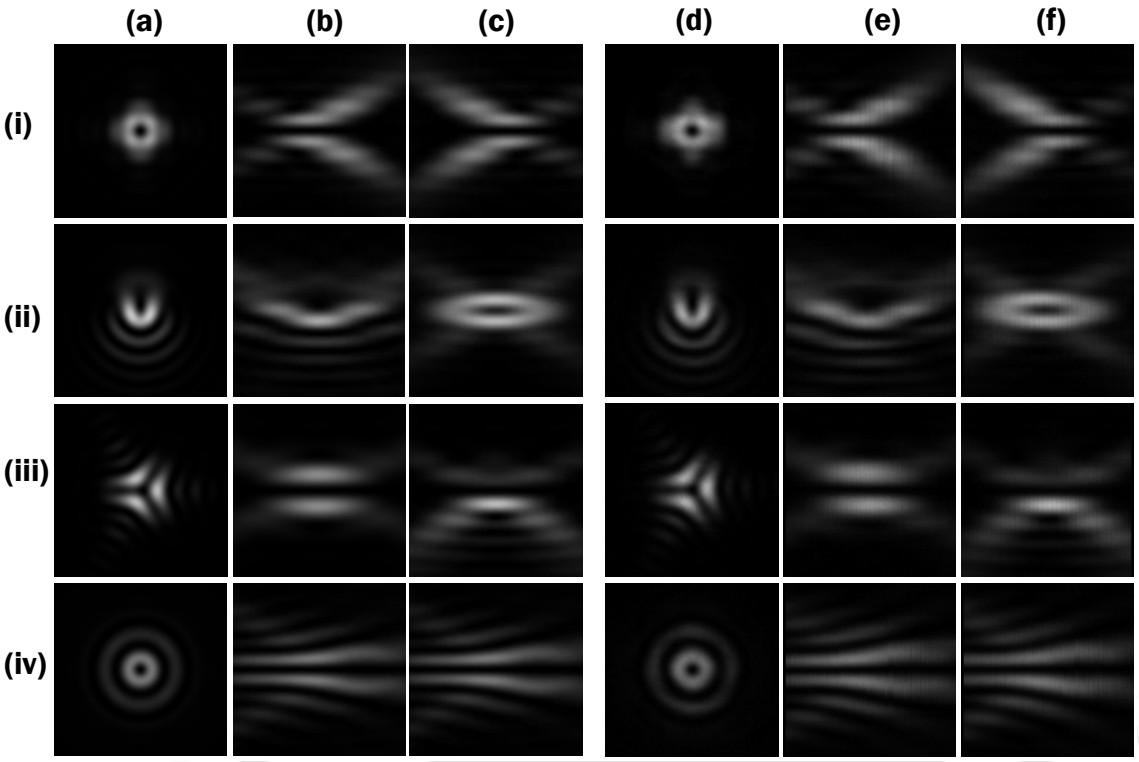

Figure 3.16: Resultant intensity distributions of azimuthally polarized beam in the XY, XZ and YZ planes obtained (a→c) theoretically and (d→f) experimentally in the presence of ϕ_{rms}= 1 radian of (i) astigmatism, (ii) coma, (iii) trefoil and (iv) spherical aberration.

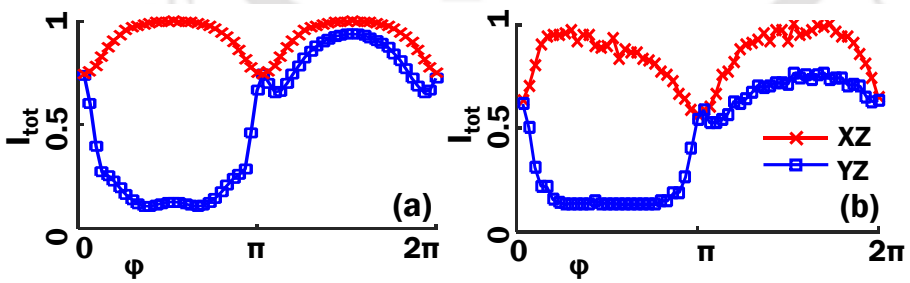

Figure 3.17: Variation of maximum value of intensity along the circumference of the boat-shaped beam in the XZ and YZ planes vs the angle φ corresponding to the (a) theoretically obtained and (b) experimentally obtained results.

TH-1501_10612103

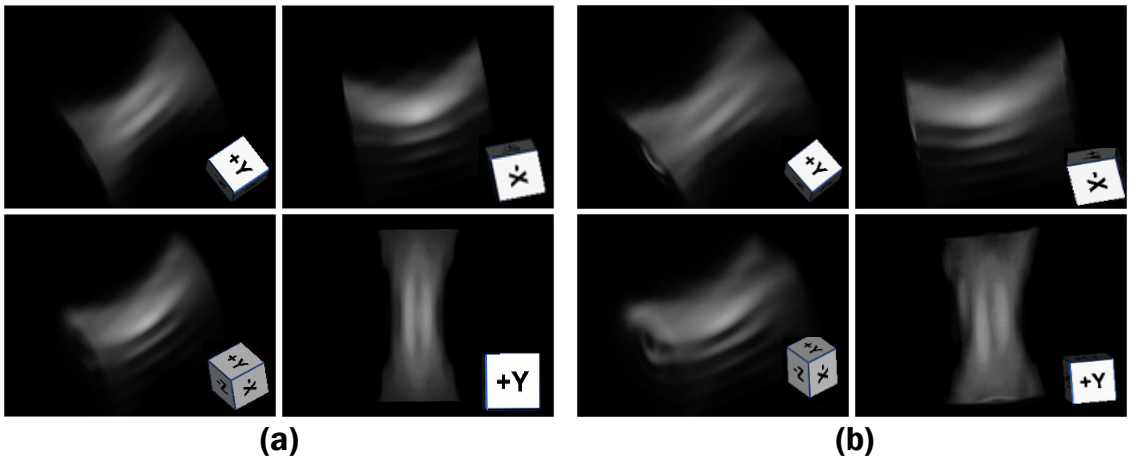

Figure 3.18: Different projections of the digitally constructed 3D boat-shaped beam from the (a) theoretically obtained and (b) experimentally obtained data of the coma aberrated azimuthally polarized beam. The projection planes are indicated at the bottom right corner of each image.

also plot the variation of maximum value of intensity in the XZ and YZ planes along the circumference of boat-shaped beam. Figure. 3.17 shows the (a) theoretically and (b) experimentally obtained plots of maximum intensity along a line oriented at φ with the horizontal vs the angle φ for the XZ and YZ planes. In order to get a 3D view of the boat-shaped intensity distribution we digitally combine the intensity distributions in all the planes parallel to the focal plane in the focal volume of the coma aberrated azimuthally polarized beam. Thus we construct a 3D focal volume from both our theoretical data and experimental data. Figures 3.18 (a) and (b) shows different projections of the boat-shaped beam in 3D, obtained theoretically and experimentally, which again validates, the vectorial diffraction theory, in general, and the theoretical predictions regarding the generation of the boat-shaped beam, in particular.

3.4 Conclusion

In this chapter we have investigated the effect of primary aberrations on the focal volume properties of an azimuthally polarized beam. We have used the Fourier transform form of the Vectorial diffraction theory to first compute the Cartesian field components in the focal volume in the presence of various Zernike circular polynomials representing the primary aberrations using a high NA lens. It is ob-

TH-1501_10612103

served that in the presence of astigmatism, coma and trefoil, the circular symmetry of the intensity distribution in the focal plane gets distorted. Moreover in the presence of coma there appears a significant amount of transversely polarized light on the optical axis. From our results we have also drawn polarization ellipses to indicate the time evolution of the resultant electric field vector in the focal volume of the aberrated azimuthally polarized beam. We have observed that in the presence of astigmatism, coma and trefoil the light in the focal volume does not remain linearly polarized as in some region it becomes elliptically polarized. Whereas in the presence of spherical aberration, the focal intensity distribution remains axially symmetric with no light on the optical axis. Our results further showed that in the presence of a moderate amount of coma the intensity distribution near the focus takes a boat-like shape. It gives us a dark centre surrounded by light in all but one direction. This chapter also describes a division of wavefront based arbitrary vector beam forming setup which was used to generate cylindrical vector beams with user defined phase profile in the pupil plane. We have presented experimental results for an azimuthally polarized beam focused by a low NA lens in the presence of various primary aberrations. As the vectorial diffraction theory described in chapter 2 is applicable for the entire range of numerical apertures, from low to high, hence the same theory can also be used to compute the focal intensity distributions at the numerical aperture corresponding to the experimental setup. We have noticed that the experimentally obtained results agree well with the corresponding results obtained numerically, thereby validating the accuracy of the theoretical expressions used.

TH-1501_10612103

Chapter 4

Effect of primary aberrations on an azimuthally polarized beam with a helical phase mask

Smaller sized focal spot is important in many applications such as in lithography, in optical data storage, in particle trapping and manipulation, in scanning optical microscopy, in instrumental precision measurement and so on. Radially polarized beam produces a small sized focal spot in the tight focusing condition, which is smaller as compared to that of the linearly polarized beam under the same focusing condition [2, 41]. We have already discussed the various properties of an azimuthally polarized beam such as the generation of a doughnut pattern in the focal plane of the beam. On the other hand it has been shown that a smaller sized focal spot can be generated even from an azimuthally polarized beam [69, 70, 71], when a helical phase mask, which is a mask introducing a phase profile varying from 0 to 2π in the azimuthal direction, is applied at the pupil plane of the focusing lens. This new kind of beam, i.e. an azimuthally polarized beam with a helical phase mask, is in this thesis referred to as APBH. The intensity distribution in the focal plane of the APBH and the normal linearly polarized beam appear similar, as for both the intensity maxima occur at the centre. There are published works which report the effect of primary aberrations on a linearly polarized beam [22, 23]. In this chapter we intend to make a comparison on the effect of aberrations on these two types of beams i.e. linearly polarized beam and the APBH. Here we present computer simulation results of various parameters, such as focal intensity distribution, Strehl

TH-1501_10612103

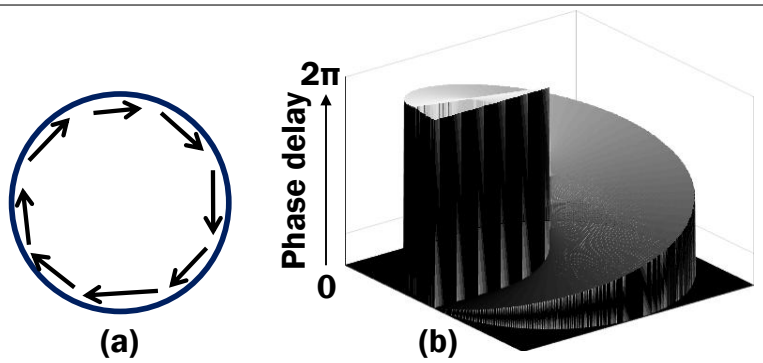

Figure 4.1: (a) Cylindrically symmetric polarization profile of an azimuthally polarized beam and (b) the surface plot of a helical phase mask.

ratio and width of the focal spot, in the focal volume of the two beams in the presence of various primary aberrations, in the high NA focusing condition [72]. We also perform experiment to generate APBH and experimentally investigate the aberration effects on both the linearly polarized beam and the APBH, under low NA focusing condition.

4.1 Focal field components of an azimuthally polarized beam with a helical phase mask

The procedure to obtain the focal field components of an azimuthally polarized beam from it's Jones matrix representation is discussed in chapters 2 and 3. To obtain the Cartesian components of the focal field of the APBH, the two pupil functions (l_x, l_y) of an azimuthally polarized beam are replaced by $(l_x\, e^{i\phi}, l_y\, e^{i\phi})$, where ϕ is the azimuthal coordinate in the pupil plane. Cylindrically symmetric polarization profile of an azimuthally polarized beam and the surface plot of a helical phase mask are displayed in Fig. 4.1. We use Zernike circular polynomials, which are shown in table 2.1 of chapter 2 to represent primary aberrations. In the presence of aberrations, the pupil functions of APBH get modified as $l_x = -\sin\phi e^{i(\Phi+\phi)}$ and $l_y = \cos\phi e^{i(\Phi+\phi)}$. In this expression $\Phi = \phi_{rms} \times Z_i$, where ϕ_{rms} is the root mean square amplitude of aberration and Z_i, i=6, 8, 10 and 11, are the various single indexed Zernike circular polynomials [21] representing primary aberrations.

TH-1501_10612103

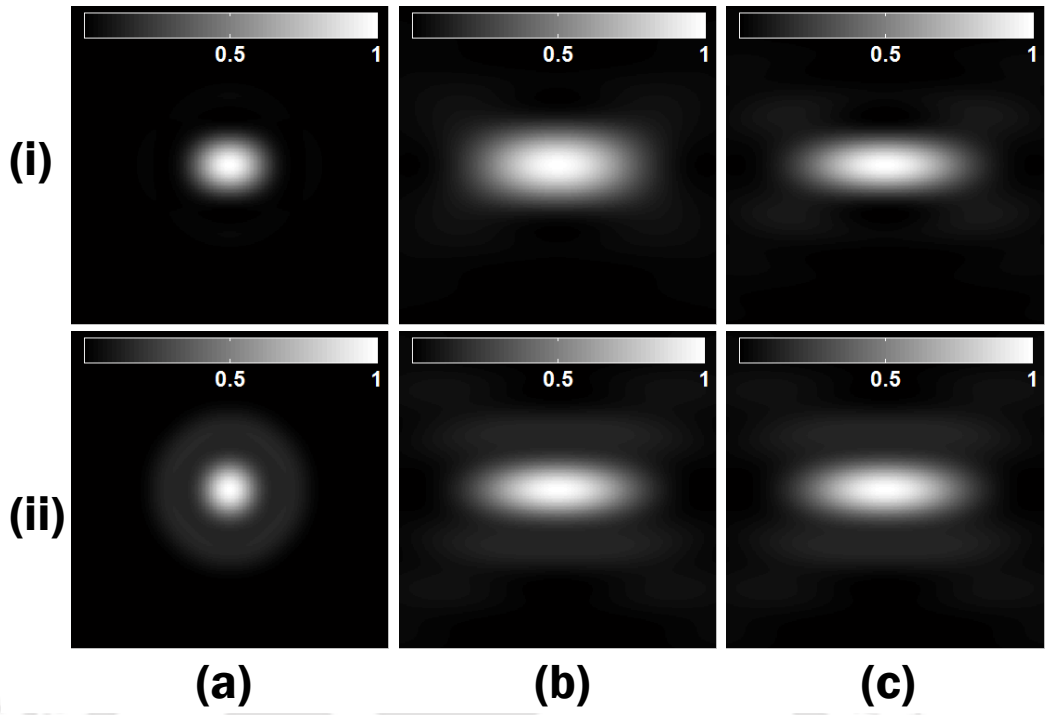

Figure 4.2: Resultant focal intensity distribution I_{tot} of (i) the X polarized beam and (ii) the APBH in the aberration free case in the (a) XY, (b) XZ and (c) YZ planes.

4.2 Numerical simulation

Numerical simulations are performed considering a focusing lens of numerical aperture equal to 0.9. Both a normal linearly polarized beam and a APBH are aberrated in the respective pupil planes by incorporating ϕ_{rms}=1 radian of various Zernike modes. Cartesian components of the focal field are computed over a volume ranging from -2λ to 2λ along the X, Y and Z axes, with the nominal focus as the origin. Figure 4.2 shows the resultant intensity distribution $I_{tot} = I_x + I_y + I_z$ of (i) the X polarized beam (XPB) and (ii) the APBH, in the (a) XY (focal plane), (b) XZ and (c) YZ planes in the aberration free case. It is noticed that only X and Z polarized components are present in the X polarized beam in the tight focusing condition, while in the case of APBH, only X and Y polarized components are present, as the Y polarized component of the X polarized beam has negligible magnitude and Z polarized component of the APBH is zero. Intensity distributions from every Cartesian component and the resultant intensity distributions, without aberration as well as in the presence of aberrations, are normalized by the respective maximum value

TH-1501_10612103

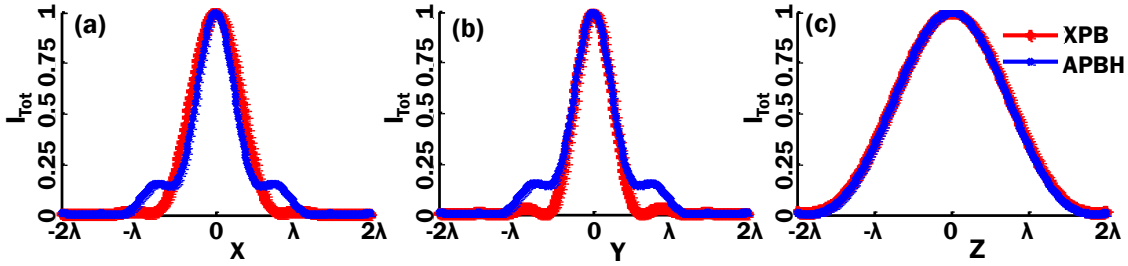

Figure 4.3: Line plots of the resultant intensity for the X polarized beam and the APBH along (a) X, (b) Y and (c) Z axes in the aberration free case. The intensity values in these plots are normalized by the respective maximum values.

of the resultant intensity in the focal plane in the aberration free case. It is noticed that in the high numerical aperture (NA) focusing condition, the X polarized beam has a significant amount of Z polarized intensity in the focal plane (which is negligible in the low NA case), which distorts the symmetry of the focal spot. However in the APBH, there is no contribution from Z polarized component (which is zero for the entire range of NA). The Z polarized component of the X polarized beam in the XZ plane in the high NA case is also of negligible value. The resultant intensity distributions of the APBH in the XZ and YZ planes are similar. However for the X polarized beam the resultant intensity distributions in the XZ and YZ planes are not similar in the high NA case. Figure 4.3 shows the line plots of the resultant intensity distribution along X, Y and Z axes for the two beams. Figures 4.3 (a) and (b) also reveal that the width of the intensity distribution at half maximum of the intensity (FWHM) along X and Y axes for the X polarized beam are not equal, which are equal for the APBH. From these figures (Figs. 4.3 (a) and (b)) it can also be noticed that the APBH has stronger side lobes relative to the XPB. Further, for the APBH, the intensity along the optical axis in the focal volume decreases, to a small extent faster relative to the XPB, as one goes away from the focus.

4.2.1 Effect of primary astigmatism

The resultant intensity distribution I_{tot} of (i) the X polarized beam and (ii) the APBH in the presence of 1 radian RMS amplitude of astigmatism in the (a) XY, (b) XZ and (c) YZ planes are presented in Fig. 4.4. The intensity distributions of these two beams in the focal plane have a two fold planar symmetry. While in the XZ and YZ planes they are symmetric only with respect to the optical axis. In the

TH-1501_10612103

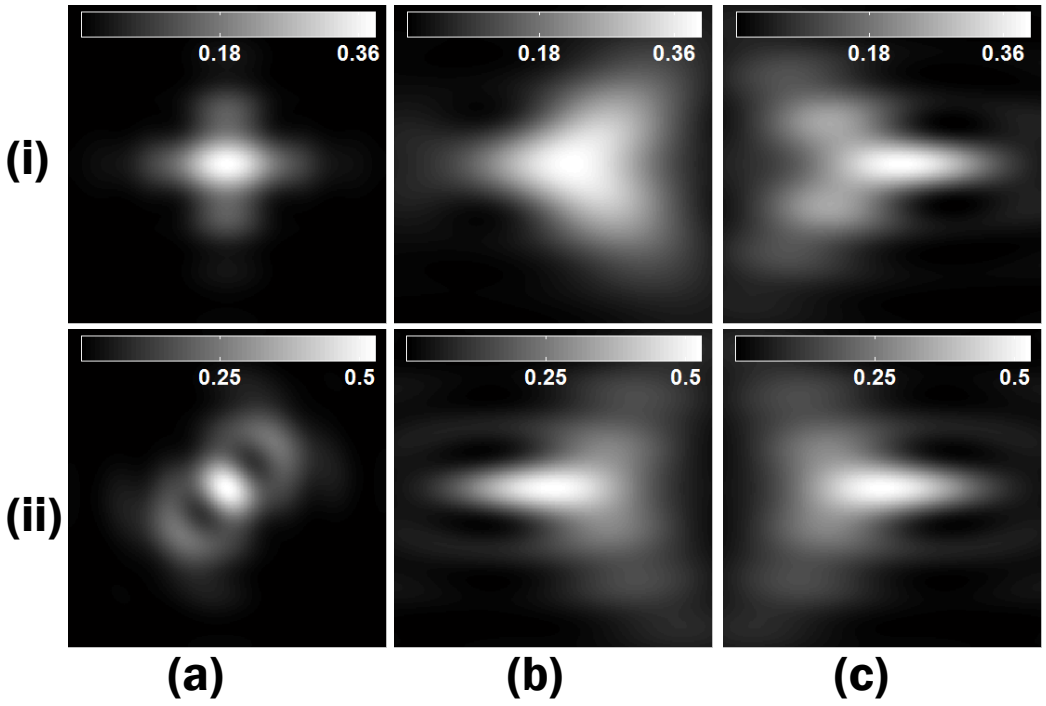

Figure 4.4: Total focal intensity distribution I_{tot} of (i) the X polarized beam and (ii) the APBH in the presence of primary astigmatism with RMS amplitude 1 radian in the (a) XY, (b) XZ and (c) YZ planes. Every image has a different color bar which is shown at its top.

case of the APBH, the intensity distributions in the XZ and YZ planes appear to be a mirror image of one another, which does not hold for the X polarized beam. Again the intensity distributions of the X polarized beam in the XZ and YZ planes are not identical. It is noticed that by applying the oppositely signed RMS amplitude to these two beams, the intensity distributions in the XZ and YZ planes can be made to rotate by 180°. It is also noticed that in the presence of astigmatism the focal spot of the APBH has higher peak intensity as compared to the X polarized beam. The line plots of the resultant intensity distribution along X, Y and Z axes are presented in Fig. 4.5. These line plots indicate that the X polarized beam has significantly larger FWHM in the focal plane along the X axis and a marginally smaller FWHM along the Y axis compared to the APBH, but the FWHM of the APBH along both the X and Y axes are equal. Further there is an axial shift in the location of the intensity maximum for the X polarized beam which is not observed for the APBH. In order to quantify the spread of the focal spot as the magnitude of various aberrations increases we describe a circular area in the focal plane around the centre of the focal

TH-1501_10612103

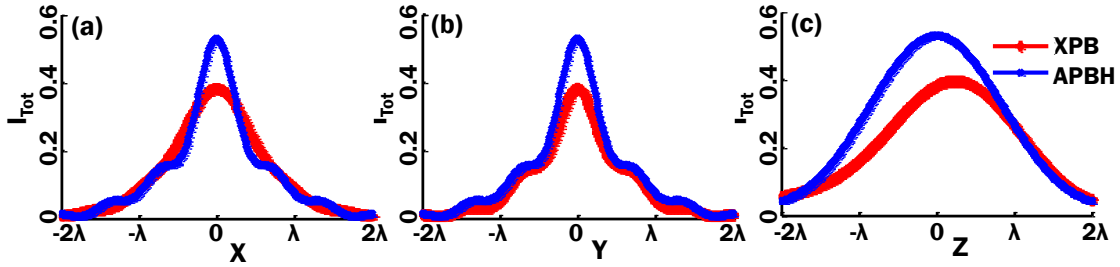

Figure 4.5: Line plots of resultant intensity for the X polarized beam and the APBH along (a) X, (b) Y and (c) Z axes in the presence of primary astigmatism with RMS amplitude 1 radian. The plots of both beams are normalized by respective maximum value of intensity in the aberration free case.

spot containing 80% of the net energy in the beam. We denote this radius as 80% energy radius (80ER). This new parameter facilitates quantitative measurement of the spread of the focal energy in the presence of aberrations. 80ER has a direction independence unlike FWHM of the focal spot which will be different in different directions for an asymmetric focal spot. We compute 80ER for the two beams as ϕ_{rms} of astigmatism increases from 0 to 1.2 radian and the same is seen Fig. 4.6 (a). It is noticed that width of the focal spot as indicated by 80ER is more effected by astigmatism in the case of the X polarized beam than the APBH.

Strehl ratio is defined as the ratio of the intensity at the focus in the presence of aberrations to the same without aberration. It is a very important parameter to quantify the quality of a lens system. For a perfect aplanatic lens system the Strehl ratio is 1. Mathematically, it can be written as

$$S = \frac{(I_x + I_y + I_z)_{Y_0, Y_0, \Phi \neq 0}}{(I_x + I_y + I_z)_{X_0, Y_0, \Phi = 0}} \tag{4.1}$$

Here X_0 and Y_0 are the coordinates of the focal point and Φ is the aberration function. We have computed the Strehl ration for the two beams by varying ϕ_{rms} from 0 to 1.2 radian. Variation of Strehl ratio with RMS amplitude is shown in Fig. 4.6. From Figs. 4.6 (a) and (b), it is clear that the width and peak intensity of the focal spot due to the APBH is least effected by astigmatism especially when it is compared with the X polarized beam. Thus the APBH is significantly more resistant to astigmatism compared to the X polarized beam.

TH-1501_10612103

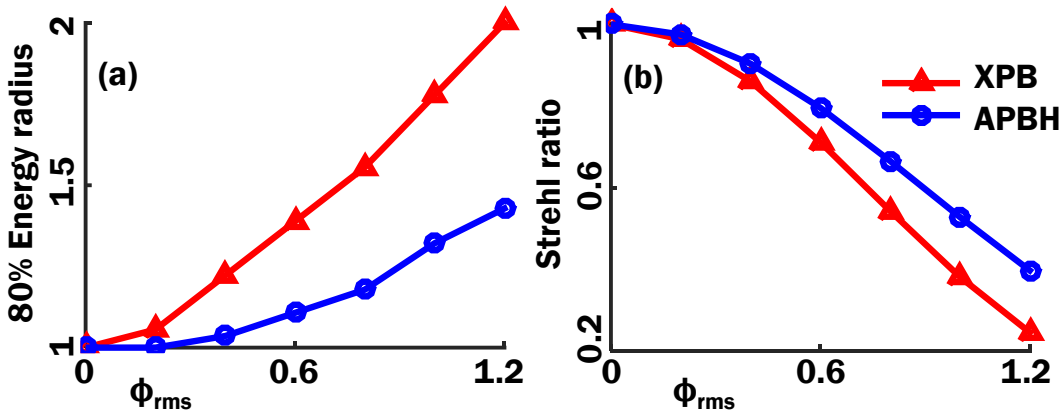

Figure 4.6: Plots of (a) 80% energy radius, and (b) Strehl ratio variation in the presence of primary astigmatism with RMS amplitude varying in between 0 to 1.2 radian. 80ER values for the two beams are normalized by the respective values in the aberration free case.

4.2.2 Effect of primary coma

The resultant intensity distribution (I_{tot}) of (i) the X polarized beam and (ii) the APBH, in the presence of 1 radian RMS amplitude of coma, in the (a) XY, (b) XZ and (c) YZ planes are displayed in Fig. 4.7. The intensity distributions in the focal plane show that the two focal spots are distorted in almost a similar manner. However in the XZ and YZ planes the two beams have different intensity distributions. For instance in the YZ plane of the X polarized beam intensity distribution has axial symmetry which is not present in the case of the APBH. Figure 4.8 show the line plots of the resultant intensity distribution along X, Y and Z axes. From these intensity plots it is seen that the APBH in the focal plane has higher side lobes as compared to the X polarized beam. Here we can also see that there is a shift in the location of the maximum of the intensity distribution for the X polarized beam which is not seen in the case of the APBH. Moreover the APBH has a much smaller FWHM along the axial direction relative to the X polarized beam in the presence of 1 radian RMS of coma. Variation of 80ER and the Strehl ratio with ϕ_{rms} of coma are presented in Fig. 4.9. It is observed that the spread of the focal spot in the presence of coma is less in the APBH than the X polarized beam, even though the Strehl ratio plots for the two beams are comparable.

TH-1501_10612103

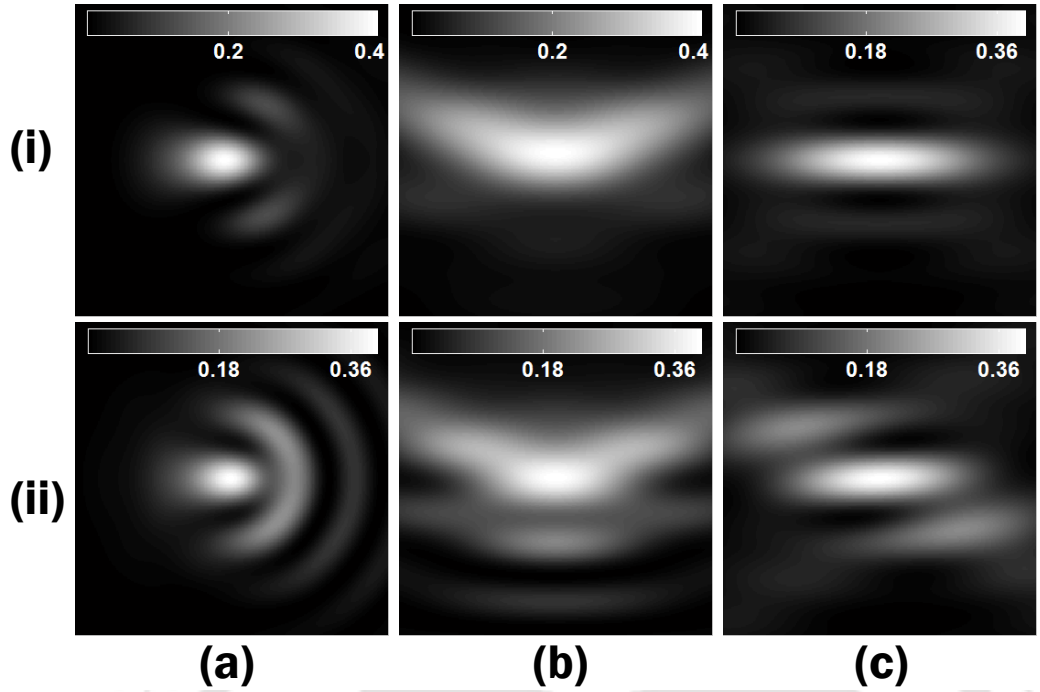

Figure 4.7: Total focal intensity distribution I_{tot} of (i) the X polarized beam and (ii) the APBH in the presence of primary coma with RMS amplitude 1 radiam in the (a) XY, (b) XZ and (c) YZ planes. Every image has a different color bar which is shown at its top.

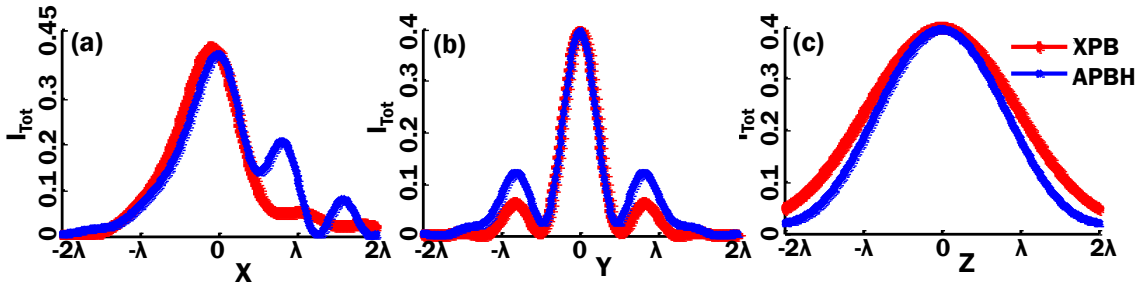

Figure 4.8: Line plots of resultant intensity for the X polarized beam and the APBH along (a) X, (b) Y and (c) Z axes in the presence of primary coma with RMS amplitude 1 radian. The Plots of this two beams are normalized by the respective maximum value of intensity in the aberration free case.

TH-1501_10612103

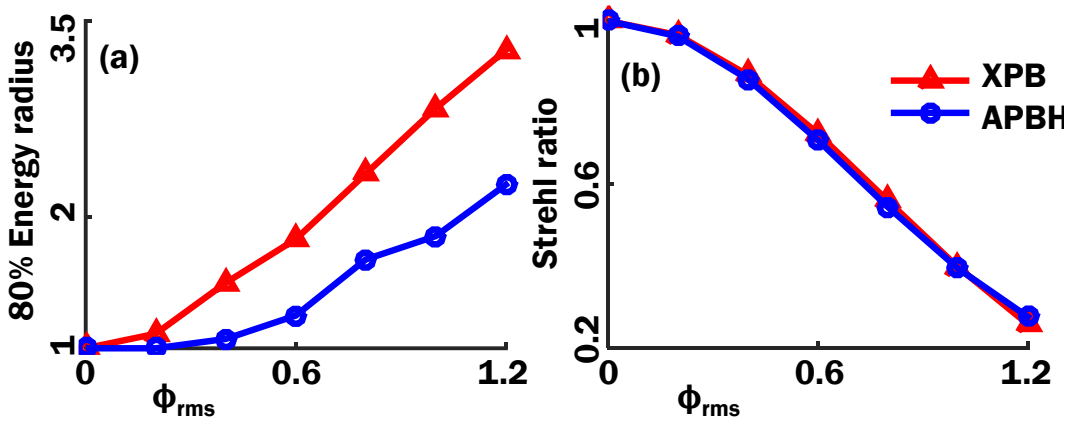

Figure 4.9: Plots of (a) 80% energy radius, and (b) Strehl ratio variation in the presence of primary coma with RMS amplitude varying in between 0 to 1.2 radian. 80ER values for the two beams are normalized by the respective values in the aberration free case.

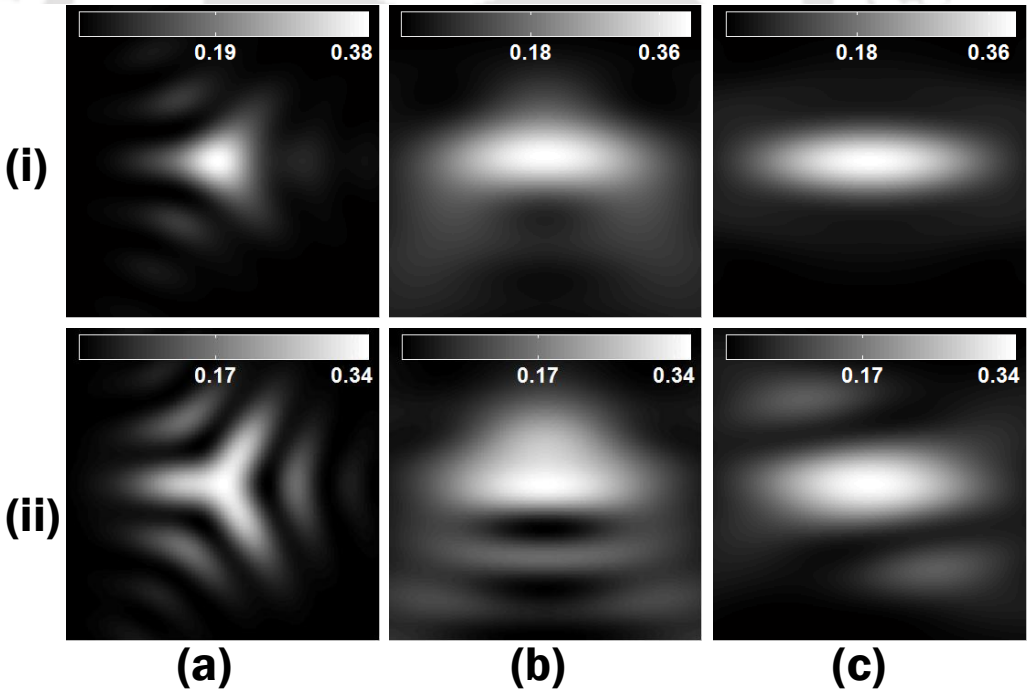

Figure 4.10: Resultant focal intensity distribution I_{tot} of (i) the X polarized beam and (ii) the APBH in the presence of primary trefoil with RMS amplitude 1 radian in the (a) XY, (b) XZ and (c) YZ planes. Every image has a different color bar which is shown at its top.

TH-1501_10612103

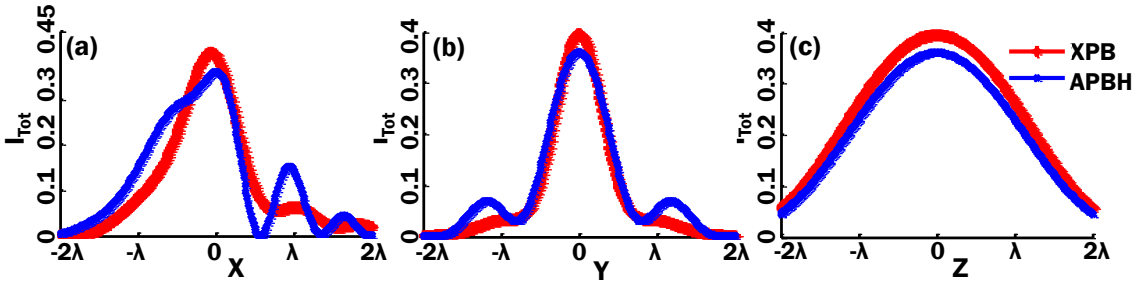

Figure 4.11: Line plots of resultant intensity for the X polarized beam and the APBH along (a) X, (b) Y and (c) Z axes in the presence of primary trefoil with RMS amplitude 1 radian. The plots of the two beams are normalized by respective maximum value of intensity in the aberration free case.

4.2.3 Effect of primary trefoil

Figure 4.10 show the resultant intensity distribution of (i) the X polarized beam and (ii) the APBH in the presence of 1 radian RMS amplitude of trefoil in the (a) XY, (b) XZ and (c) YZ planes. It is seen that for both the beams the intensity distributions in the focal plane in the presence of trefoil are distorted in a similar fashion. However the same does not apply in the XZ and YZ planes. The intensity distributions of both the beams in the XZ plane are symmetric only with respect to the transverse axis, where as in the YZ plane it is symmetric only for the X polarized beam and is asymmetric for the APBH. Figure 4.11 represents the line plots of the resultant intensity along X, Y and Z axes. It is noticed that in the XY plane the APBH has larger sidelobes compared to the X polarized beam. However in the axial direction the APBH has a marginally smaller FWHM relative to the X polarized beam. Again we have plotted 80% energy radius and the Strehl ratio for the two beams as the ϕ_{rms} varies and are seen in Figs. 4.12 (a) and (b). It is noticed that the X polarized beam spreads more quickly relative to the APBH as the magnitude of trefoil increases. However in the case of Strehl ratio, the X polarized beam peforms marginally better than the APBH.

4.2.4 Effect of primary spherical aberration

The resultant intensity distribution (I_{tot}) of (i) the X polarized beam and (ii) the APBH in the presence of 1 radian RMS amplitude of spherical aberration in the (a) XY, (b) XZ and (c) YZ planes are shown in Fig. 4.13. The intensity distributions in

TH-1501_10612103

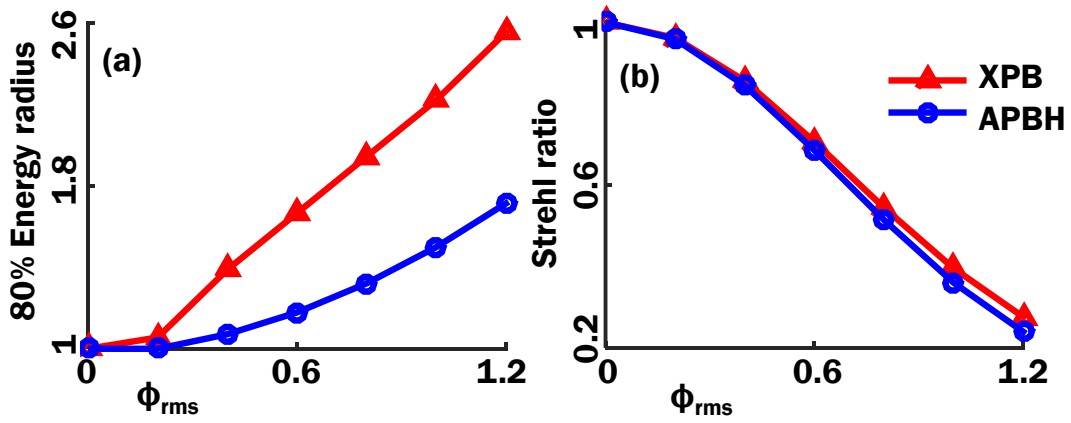

Figure 4.12: Plots of (a) 80% energy radius, and (b) Strehl ratio variation in the presence of primary trefoil with RMS amplitude varying in between 0 to 1.2 radian. 80ER values for the two beams are normalized by the respective values in the aberration free case.

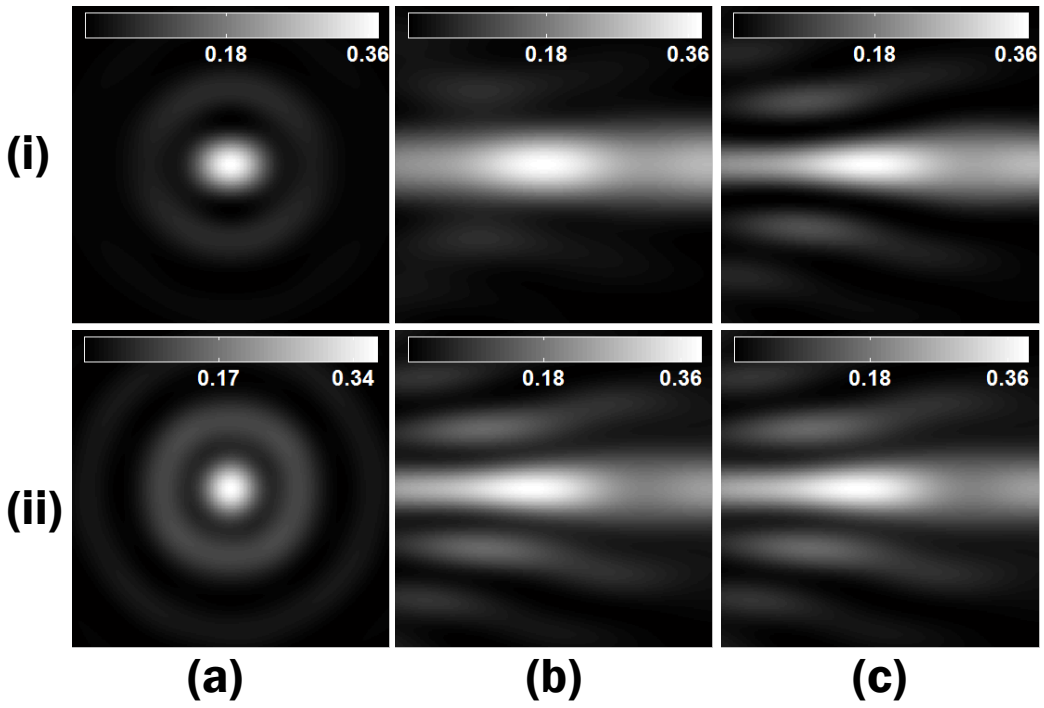

Figure 4.13: Resultant focal intensity distribution I_{tot} of (i) the X polarized beam and (ii) the APBH in the presence of primary spherical aberration with RMS amplitude 1 radian in the (a) XY, (b) XZ and (c) YZ planes. Every image has a different color bar which is shown at its top.

TH-1501_10612103

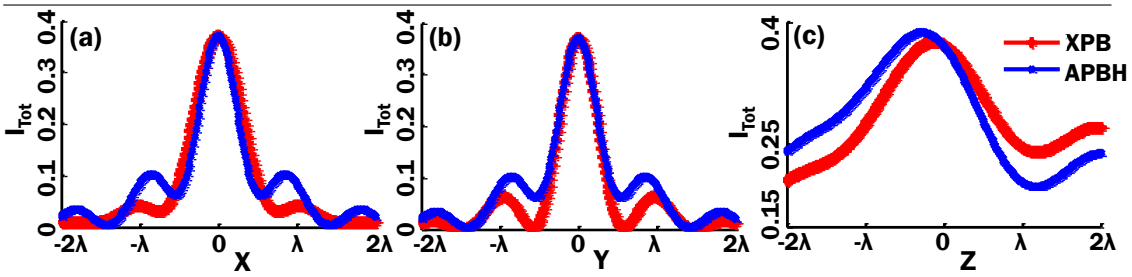

Figure 4.14: Line plots of resultant intensity for the X polarized beam and the APBH along (a) X, (b) Y and (c) Z axes in the presence of primary spherical aberration with RMS amplitude 1 radian. The plots of this two beams are normalized by respective maximum value of intensity in the aberration free case.

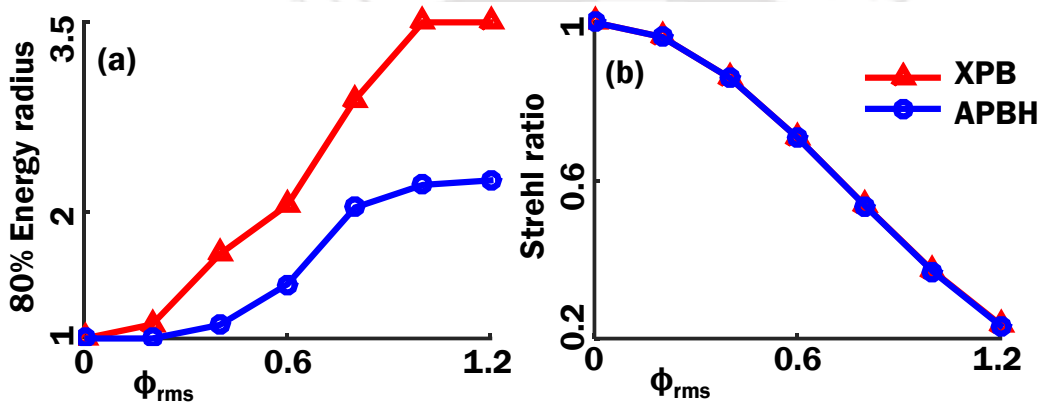

Figure 4.15: Plots of (a) 80% energy radius, and (b) Strehl ratio variation in the presence of primary spherical aberration with RMS amplitude varying in between 0 to 1.2 radian. 80ER values for the two beams are normalized by the respective values in the aberration free case.

the focal plane reveal that even though the effect on the X polarized and Y polarized intensity distributions of the two beams are different, the effect on the net intensity distributions is almost identical. Due to the circular symmetry of the aberration profile, in the XZ and YZ planes the intensity distributions of the two beams are symmetric with respect to the optical axis. The line plots of the resultant intensity along X, Y and Z axes are shown in Fig. 4.14. It is observed that in the focal plane the APBH contribute more side lobes compared to the X polarized beam. The maximum of the APBH has a small shift along the optical axis in the presence of spherical aberration which does not occur for the X polarized beam. To be noted that in the presence of defocus the maxima of both the beams under go equal amount of shift along the optical axis. Variation of 80ER and the Strehl ratio with respect to

TH-1501_10612103

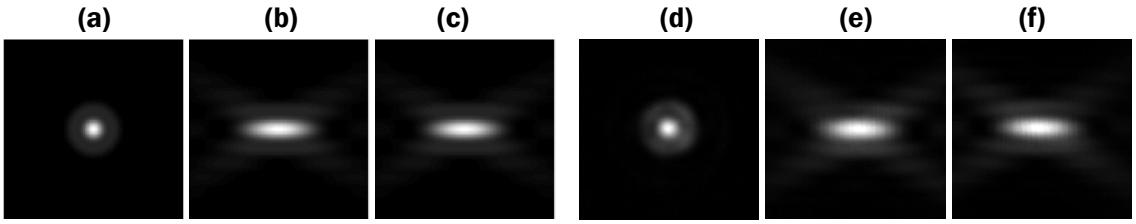

Figure 4.16: Resultant focal intensity distribution I_{tot} of the APBH in the (a) XY, (b) XZ and (c) YZ planes obtained theoretically, and in the (d) XY, (e) XZ and (f) YZ planes obtained experimentally, in the aberration free case, using a focusing lens of NA=0.056.

the RMS amplitude are shown in Fig. 4.15. We observe that the APBH has smaller spread of the focal spot in the presence of spherical aberration. However the Strehl ratio of the X polarized beam and the APBH degrade at the same rate with the increase in spherical aberration.

4.3 Experimental demonstration in the low NA case

We then used our experimental vector beam forming arrangement, described in chapter 3, to generate the APBH. We incorporated the effective NA of the focusing lens used in the setup in our theory to compute the corresponding field components numerically. We first captured the focal intensity distributions in the aberration free case. Both the theoretical and experimental focal intensity distributions in the XY, XZ and YZ planes in the aberration free case are seen in Fig. 4.16. We then reconfigured the two holograms to introduce ϕ_{rms}=1 radian of various primary aberrations such as astigmatism, coma, trefoil and spherical aberration, in the pupil plane of each of the beams. The theoretically and experimentally obtained focal intensity distributions are shown in Fig. 4.17. It is noticed that the theoretical results in the low NA case agree very well with the corresponding experimental results.

In order to further investigate the aberration resilience of APBH relative to the X polarized beam we captures focal spots of the two beams with ϕ_{rms} for each aberration varying between 0 and 1.2 radian. We estimated the 80% energy radius in the focal plane of both the beams for each ϕ_{rms} value of astigmatism, coma, trefoil and spherical aberration. Figures 4.18 (a), (b) and (c) show the experimental

TH-1501_10612103

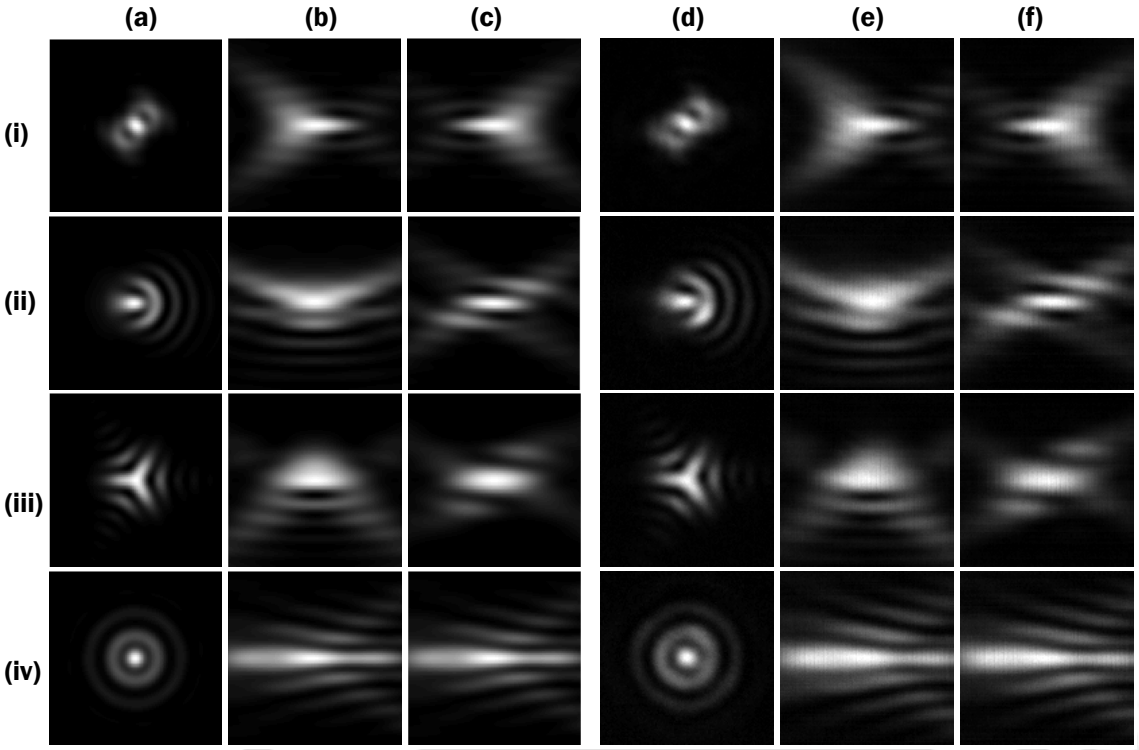

Figure 4.17: Resultant focal intensity distribution I_{tot} of the APBH in the (a) XY, (b) XZ and (c) YZ planes obtained theoretically, and in the (d) XY, (e) XZ and (f) YZ planes obtained experimentally, in the presence of ϕ_{rms}=1 radian of (i) astigmatism, (ii) coma, (iii) trefoil and (iv) spherical aberration, using a focusing lens of NA=0.056.

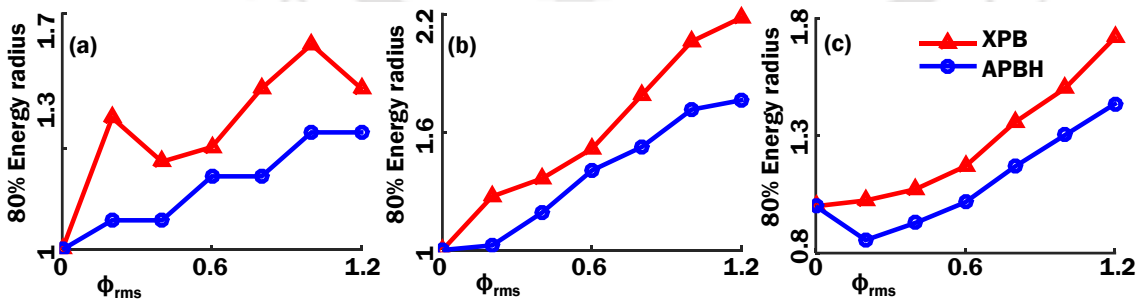

Figure 4.18: Plots of 80% energy radius for the X polarized beam and the APBH vs ϕ_{rms} corresponding to (a) astigmatism, (b) coma and (c) trefoil. 80ER values of each beam are normalized by the respective 80ER value in the unaberrated case.

TH-1501_10612103

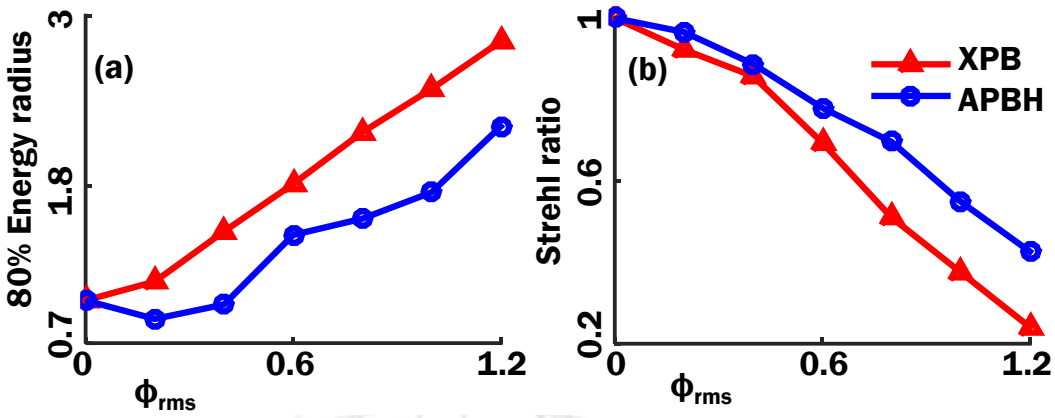

Figure 4.19: (a) Plots of 80% energy radius for the X polarized beam and the APBH vs ϕ_{rms} of spherical aberration. 80ER values of each beam are normalized by the respective 80ER value in the unaberrated case. (b) Plots of Strehl ratio for the X polarized beam and the APBH vs ϕ_{rms} of coma.

plots of 80ER vs ϕ_{rms} for the X polarized beam and the APBH in the presence of astigmatism, coma, and trefoli, respectively while Fig. 4.19 (a) shows the same plots in the presence of spherical aberration. It is noticed that as predicted by the simulation results the spread of the focal spot for the APBH is less affected by various aberrations compared to the X polarized beam. It has also been observed during our theoretical investigations under high NA focusing condition that the APBH exhibits superior immunity to the presence of astigmatism, in so far as Strehl ratio is concerned, relative to the X polarized beam. Thus in order to verify this feature experimentally we also obtained the experimental plots of Strehl ratio vs ϕ_{rms} for the X polarized beam and the APBH and are seen in Fig. 4.19. It is again observed that the APBH performs better than the X polarized beam in terms Strehl ratio, in the presence of astigmatism.

4.4 Conclusion

An azimuthally polarized beam with a helical phase mask and a linearly polarized beam have similar kind of focal intensity distributions. Thus the former beam can be used as an alternative to the latter beam. Due this similarity, in this chapter, it is intended to investigate the effect of primary aberrations on the two types of beams. Here we observed that the azimuthally polarized beam with a helical phase mask is more resistant to the primary aberrations as far as spread of the focal energy

TH-1501_10612103

is concerned. The same beam also provides a better performance for the Strehl ratio in the presence of primary astigmatism when compared with the X polarized beam. Thus the azimuthally polarized beam with a helical phase mask can provide superior resilience to primary aberrations, especially to astigmatism, relative to a linearly polarized beam. We have also demonstrated the aberration effect on the azimuthally polarized beam with a helical phase mask experimentally taking a low NA focusing lens. The theoretical predictions regarding aberration resilience of the APBH compared to the X polarized beam also has been verified experimentally under low NA focusing condition.

TH-1501_10612103

Chapter 5

Effect of primary and secondary aberrations on a radially polarized beam

5.1 Introduction

As stated previously the radially polarized beams have important properties in the tight focusing condition which may get affected in the presence of aberrations. Monochromatic aberrations commonly present in an optical system can be categorized into two groups, namely lower order or primary and higher order such as secondary or tertiary aberrations. There are published works on the effect of lower order or primary aberrations on the radially polarized beams, [24, 46, 73, 74, 75, 76]. Although the primary aberrations are considered to be most common in the optical systems, nevertheless, the presence of higher order aberrations in particular the secondary aberrations can not be nullified. Therefore it is important to study the effect of higher order aberrations, as well, on the radially polarized beams. In this chapter we investigate the effects of both primary and secondary monochromatic aberrations on different focal volume parameters of a radially polarized beam [77], such as the net energy density or intensity in the focal volume, the Strehl ratio and the spread of focal energy. We thus provide a comparative study between the effects of primary and secondary aberrations on the radially polarized beam. Our theoretical results in the low NA focusing condition are verified by using the vector beam forming arrangement.

TH-1501_10612103

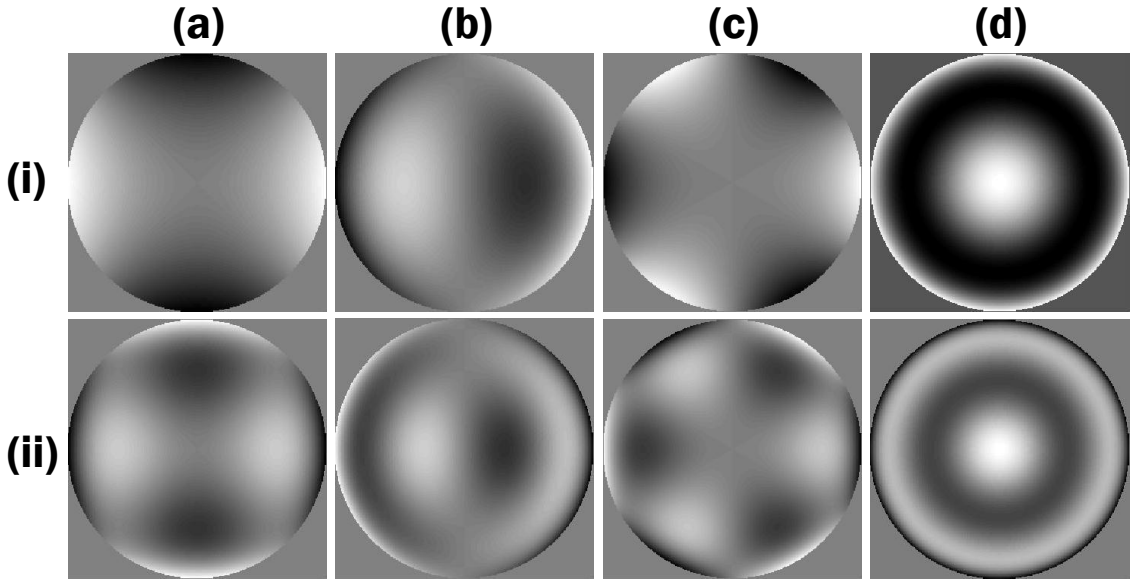

Figure 5.1: Gray scale plots of the phase profiles of, (i) (a-d), of primary astigmatism (Z_6), primary coma (Z_8), primary trefoil (Z_{10}) and primary spherical aberration (Z_{11}) and (ii) (a-d), of secondary astigmatism ($-Z_{12}$), secondary coma ($-Z_{16}$), secondary trefoil ($-Z_{18}$) and secondary spherical aberration ($-Z_{22}$). Both primary and secondary aberrations have RMS amplitude of 1 radian each.

5.2 Numerical simulation of high NA focusing

The Jones matrix representation of an unaberrated radially polarized beam can be written as

$$\begin{pmatrix} \cos\phi \\ \sin\phi \end{pmatrix}$$

where ϕ is the azimuthal angle in the pupil plane. The Cartesian components of the beam near the focus are computed by taking $l_x = \cos\phi$ and $l_y = \sin\phi$ in the Fourier transform form of the vectorial diffraction theory as discussed in chapter 2. The numerical simulations are performed by considering a focusing lens having numerical aperture equal to 0.9. The radially polarized beam incident on the lens is considered to have a uniform amplitude profile. The beam is aberrated using various Zernike polynomials, each of RMS amplitude equal to 1 radian, and the focal fields are computed over a volume extending from -2λ to 2λ along X, Y and Z axes by considering the nominal focal point to be the origin.

Zernike polynomials representing primary and secondary aberrations are shown in table 2.1 of chapter 2. For this investigation we have considered the second order

TH-1501_10612103

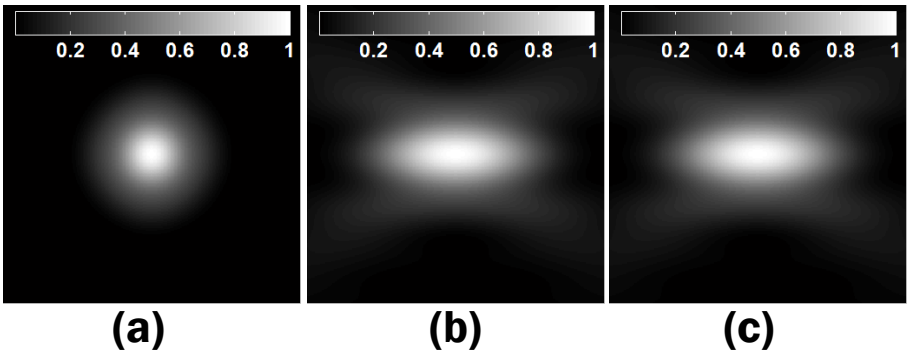

Figure 5.2: The normalized resultant intensity distribution ($I_x + I_y + I_z$) of a radially polarized beam in the aberration free case in the (a) XY, (b) XZ and (c) YZ planes, for a lens with NA=0.9.

aberrations such as secondary astigmatism (Z_{12}), tetrafoil (Z_{14}), secondary x coma (Z_{16}), secondary x trefoil (Z_{18}), pentafoil (Z_{20}) and secondary spherical aberration (Z_{22}). Figures 5.1 (i)(a-d) show the gray scale plots of primary astigmatism (Z_6), primary coma (Z_8), primary trefoil (Z_{10}) and primary spherical aberration (Z_{11}), while (ii) (a-d) show the gray scale plots of secondary astigmatism ($-Z_{12}$), secondary coma ($-Z_{16}$), secondary trefoil ($-Z_{18}$) and secondary spherical aberration ($-Z_{22}$), with RMS amplitude of aberration equal to 1 radian in both the two cases. We have noticed that some of the positive primary aberrations have comparable profiles with certain negative secondary aberrations. For instance, the phase profiles of primary aberrations such as primary astigmatism (Z_6), primary x coma (Z_8), primary trefoil (Z_{10}) and primary spherical aberration (Z_{11}) are similar (especially near the periphery) to the phase profiles of negative of secondary aberrations such as secondary astigmatism (Z_{12}), secondary coma (Z_{16}), secondary trefoil (Z_{18}) and secondary spherical aberration (Z_{22}). Due to this property, the effect of Z_6 and $-Z_{12}$, Z_8 and $-Z_{16}$, Z_{10} and $-Z_{18}$, and Z_{11} and $-Z_{22}$ are investigated in pairs, while for the remaining second order Zernike Polynomials investigations are made independently.

Various intensity values in the focal volume, both with and without aberrations, are normalized by the maximum value of total or resultant intensity in the focal plane in the aberration free case. In this investigation $I_x + I_y$, I_z and $I_x + I_y + I_z$ represents the sum of X and Y polarized intensity, axially polarized intensity and the resultant intensity due to all the polarization components, respectively. Figure 5.2 show the resultant intensity distribution ($I_x + I_y + I_z$) of a radially polarized beam in the (a) XY, (b) XZ and (c) YZ planes in the aberration free case. Owing to

TH-1501_10612103

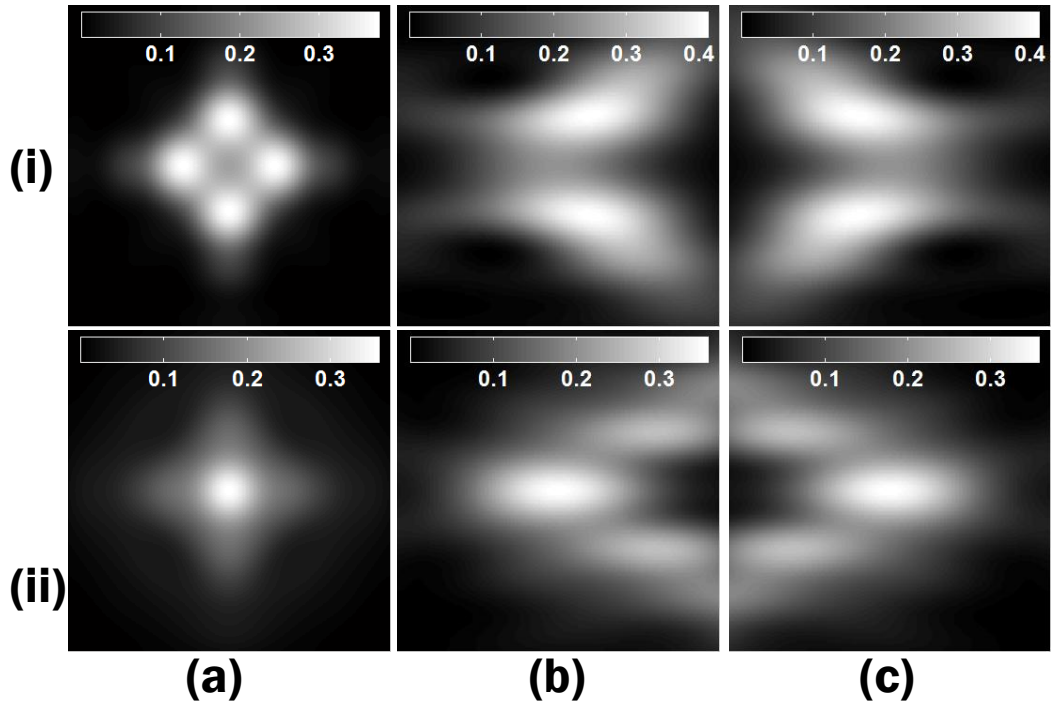

Figure 5.3: The normalized resultant intensity distribution ($I_x + I_y + I_z$) of a radially polarized beam aberrated with ϕ_{rms}=1 radian of (i) positive primary astigmatism and (ii) negative secondary astigmatism in the (a) XY, (b) XZ and (c) YZ planes.

the cylindrical symmetry, for a radially polarized beam in the unaberrated case, the XZ and YZ plane intensity distributions are identical. Also for a radially polarized beam at NA=0.9, a strong Z polarized electric field component exists at the center of the focal volume, which is negligible in the low numerical aperture case. Besides the resultant intensity distributions of a radially polarized beam in the XY, XZ and YZ planes have symmetry about the optical axis.

5.2.1 Effect of primary and secondary astigmatism

Figure 5.3 shows the resultant intensity distribution of a radially polarized beam in the presence of (i) positive primary and (ii) negative secondary astigmatism with RMS amplitude of aberration 1(radian) in the (a) XY plane, (b) XZ plane and (c) YZ plane. We notice that there is a disappearance in the circular symmetry of the intensity distribution in the XY plane, even though there exists a 4-fold planar symmetry. It is also seen that in the presence of secondary astigmatism there exists an intensity maximum at the focus, while in the presence of primary astigmatism there occur a intensity minimum. Further it is observed that the intensity distributions

TH-1501_10612103

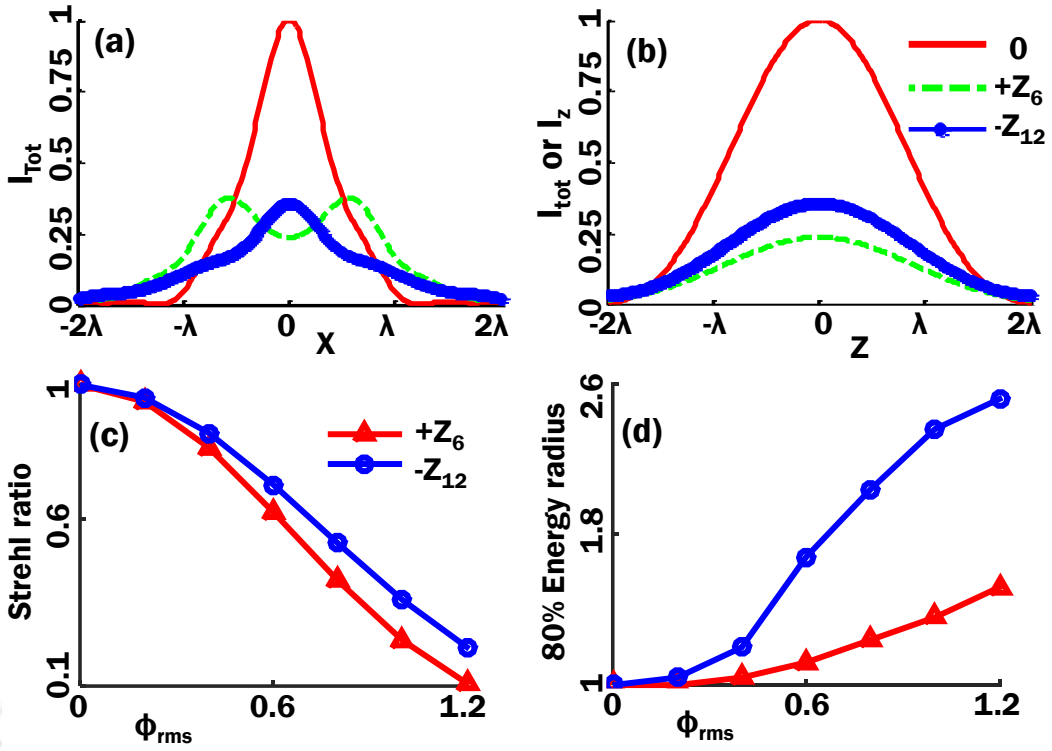

Figure 5.4: (a) Line plots of total intensity in the XY plane along X or Y axis, (b) line plots of total intensity or Z polarized intensity along the optical axis, (c) variation of Strehl ratio and (d) variation of 80ER in the presence of positive primary and negative secondary astigmatism vs ϕ_{rms}. 80ER values are normalized by the value in the respective zero aberration cases.

in the XZ plane is simply a 180° rotation of the YZ plane intensity distributions. Thus on reversing the sign of the aberration, the intensity distributions of the XZ plane and the YZ plane get interchanged. Our results also indicate that primary astigmatism has more pronounced effect on the Z polarized field than on the laterally polarized field while secondary astigmatism has more pronounced effect on the laterally polarized field than on the axially polarized field. Figures 5.4 (a) and (b) show line plots of total intensity variation along the X or Y axis and the Z axis, respectively. It is seen that the effect of primary astigmatism on the intensity distribution along the optical axis is more severe than that of secondary astigmatism. We have also computed the variation of Strehl ratio and 80% energy radius (80ER) of the resultant intensity in the focal plane as ϕ_{rms} varies from 0 to 1.2 radian and the plots are seen in Figs. 5.4 (c) and (d). We see that in the presence of primary astigmatism the Strehl ratio decreases faster compared to the presence of secondary astigmatism. Thus the effect of the primary astigmatism is more severe on the

TH-1501_10612103

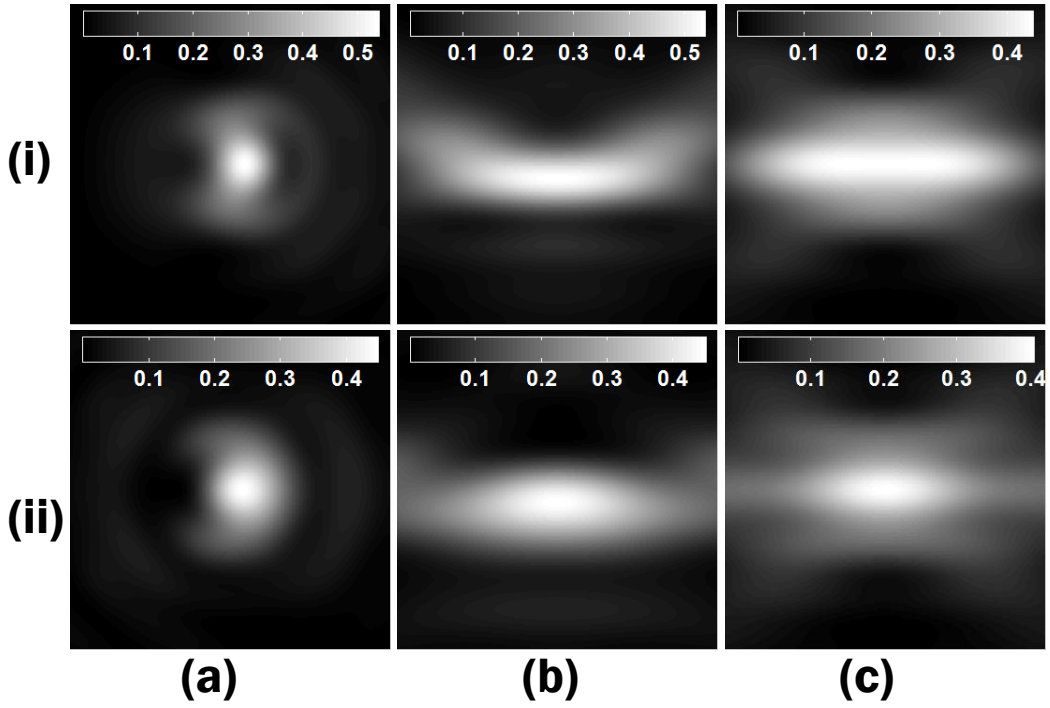

Figure 5.5: The normalized resultant intensity distribution ($I_x + I_y + I_z$) of a radially polarized beam aberrated with ϕ_{rms}=1 radian of (i) positive primary coma and (ii) negative secondary coma in the (a) XY, (b) XZ and (c) YZ planes.

Strehl ratio. However the spread of the focal spot is more due to the secondary astigmatism than the primary astigmatism as indicated by the 80ER plots seen in Fig. 5.4 (d).

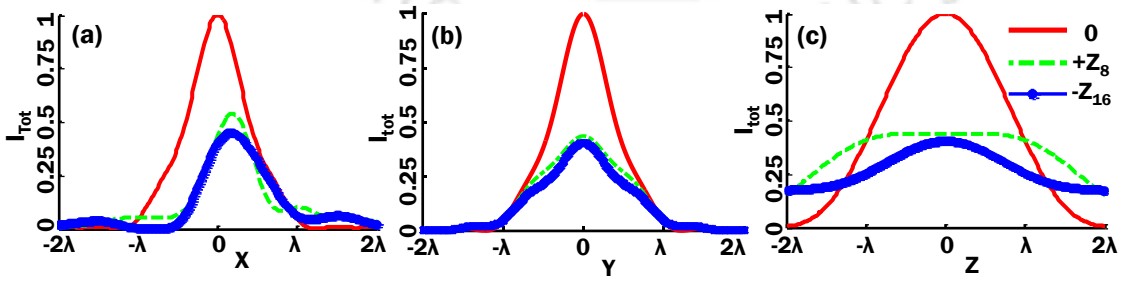

Figure 5.6: Line plots of total intensity in the XY plane along (a) X and (b) Y axes, (c) line plot of total intensity along the optical axis, in the presence of positive primary and negative secondary coma.

TH-1501_10612103

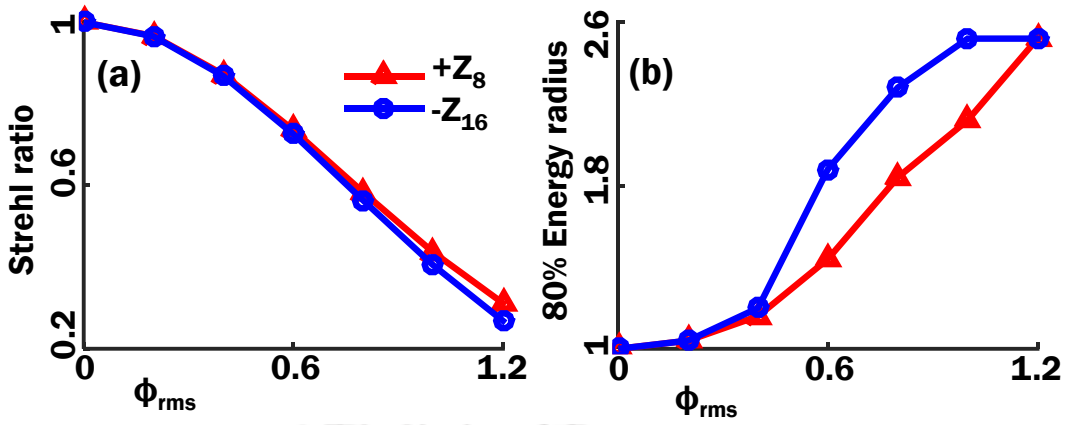

Figure 5.7: (a) Variation of Strehl ratio and (b) variation of 80ER vs ϕ_{rms} of positive primary and negative secondary coma.

5.2.2 Effect of primary and secondary coma

Figure 5.5 shows the resultant intensity distribution of a radially polarized beam in the presence of (i) positive primary and (ii) negative secondary x coma of RMS amplitude 1(radian) in the (a) XY plane, (b) XZ plane and (c) YZ plane in the focal volume. It is seen that the presence of primary or secondary coma distorts the circular symmetry of the intensity distribution in the focal plane. However the size of the focal spot in the presence of secondary coma appears larger as compared to that of primary coma. As seen in Figs. 5.5 (b) and (c), for a radially polarized beam in the presence of the two comas, the XZ and the YZ planes have different intensity distribution profiles. The intensity distribution in the XZ plane is primarily on one side of the optical axis, while in the YZ plane intensity distribution is on both the sides of the optical axis and is symmetric with respect to the Y and Z axes. Figures 5.7 (a) and (b) show the Strehl ratio and 80% energy radius in the focal plane, respectively, as ϕ_{rms} of the two aberrations increases from 0 to 1.2 radian. It is seen that secondary coma degrades the Strehl ratio and the 80% energy radius, more severely, in comparison to primary coma. Figures 5.6 (a), (b) and (c) show line plots of total intensity along X, Y and Z axes. Along the Y axis there is no significant variation in the total intensity (i.e. only a decrease in the peak value of intensity), while along the X axis, there is a shift in the maximum value of the intensity distribution. From the intensity plots, it is clear that in the total intensity along optical axis, there is a contribution from other polarization components in addition to the Z polarized component.

TH-1501_10612103

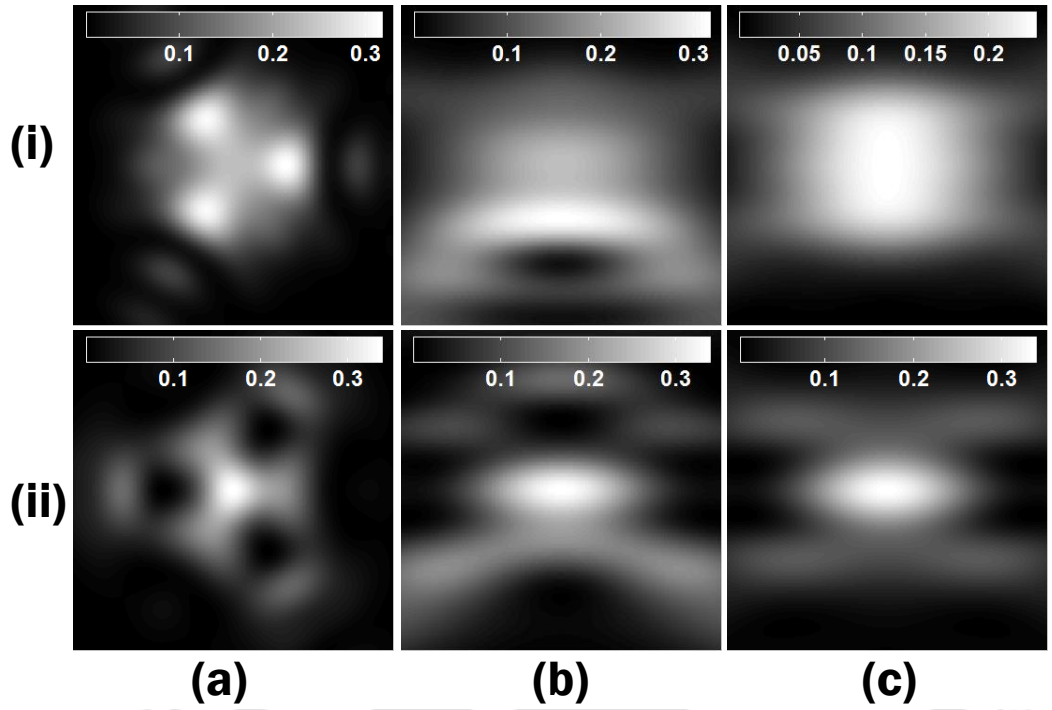

Figure 5.8: Normalized resultant intensity distribution ($I_x + I_y + I_z$) of a radially polarized beam aberrated with ϕ_{rms}=1 radian of (i) positive primary trefoil and (ii) negative secondary trefoil in the (a) XY, (b) XZ and (c) YZ planes.

5.2.3 Effect of primary and secondary trefoil

Figure 5.8 shows the resultant intensity distribution of a radially polarized beam in the presence of (i) positive primary and (ii) negative secondary trefoil aberration with RMS amplitude of 1(radian) in the (a) XY plane, (b) XZ plane and (c) YZ plane. Here we have noticed that the intensity distribution in the XY plane has three fold planar symmetry. In the case of primary and secondary trefoil, intensity distributions of a radially polarized beam in the XZ and YZ planes are not same. The intensity distribution in the XZ plane mostly exists on one side of the optical axis, while the intensity distribution in the YZ plane is symmetric with respect to the Y and Z axes. In the presence of secondary trefoil there exists a intensity maximum at the nominal focus, while in the presence of primary trefoil there exists an intensity minimum at the focus. Further, likewise astigmatism primary trefoil has more pronounced effect on the Z polarized field than on the laterally polarized field while secondary trefoil has more pronounced effect on the laterally polarized field than on the axially polarized field. Figures 5.9 (a) and (b) show the resultant intensity plots along the X axis and along the optical axis, respectively, in the

TH-1501_10612103

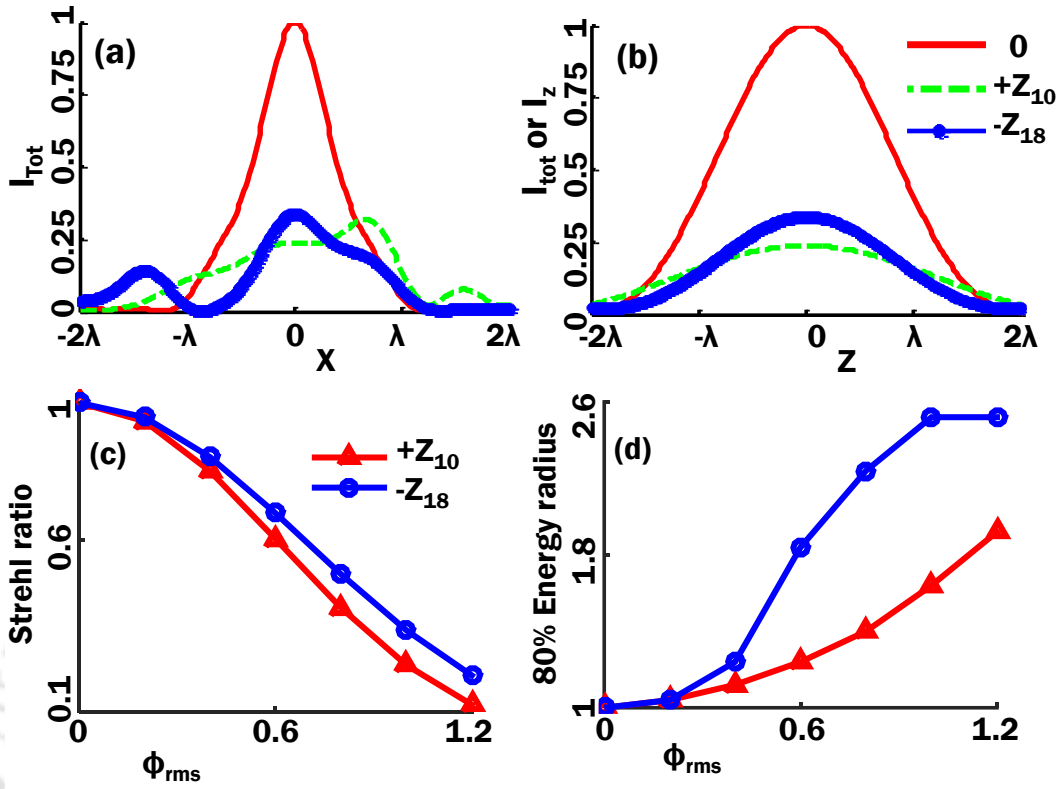

Figure 5.9: (a) Line plot of total intensity in the XY plane along the X axis, (b) line plot of total (and also Z polarized) intensity along the optical axis. Variation of (c) Strehl ratio and (d) 80% energy radius in the presence of positive primary and negative secondary trefoil vs ϕ_{rms}.

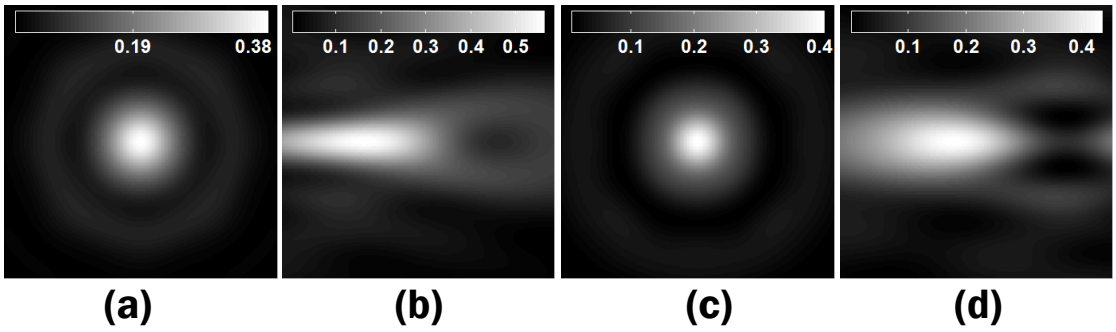

Figure 5.10: Normalized resultant intensity distribution ($I_x + I_y + I_z$) of a radially polarized beam aberrated with ϕ_{rms}=1 radian of positive primary spherical aberration in the (a) XY plane and (b) XZ or YZ plane and negative secondary spherical aberration in the (c) XY plane, and (d) XZ or YZ plane.

TH-1501_10612103

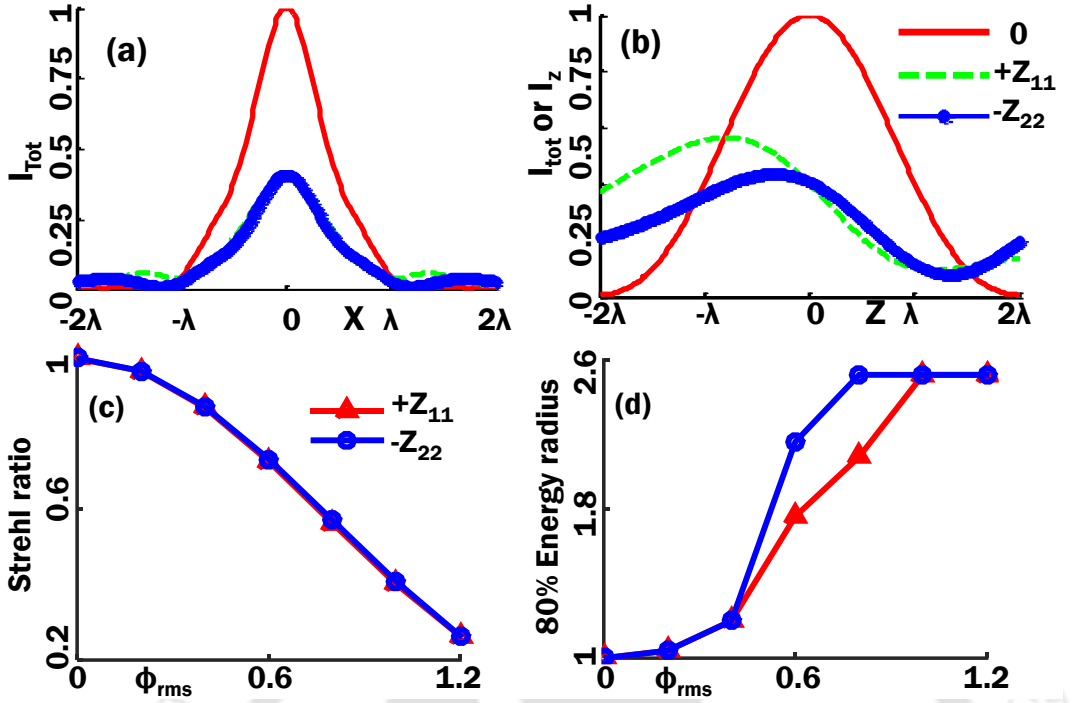

Figure 5.11: (a) Line plot of total intensity in XY plane along the X axis, and (b) line plot of total and Z polarized intensity along the optical axis. Variation of (c) Strehl ratio and (d) 80% energy radius in the presence of positive primary and negative secondary spherical aberration vs ϕ_{rms}.

presence of ϕ_{rms}=1 radian of the two trefoils. It is clear that there is a greater effect of primary trefoil on the intensity distribution along X and the optical axes. Further there is a shift in the intensity maximum along X axis in the presence of primary trafoil. As seen in Fig. 5.9 (c), the Strehl ratio decreases rapidly in the presence of primary trefoil as compared to secondary trefoil. However as indicated by Fig. 5.9 (d), the focal plane energy spreads more, as the magnitude of secondary trefoil increases, than the same in the case of primary trefoil.

5.2.4 Effect of primary and secondary spherical aberration

Figure 5.10 shows the resultant intensity distribution of a radially polarized beam in the (a) XY plane, and (b) XZ or YZ plane in the presence of positive primary and in the (c) XY plane, and (d) XZ or YZ plane in the presence of negative secondary spherical aberration with RMS amplitude 1 radian. We see that in the presence of spherical aberration, in the XY plane, the resultant intensity distribution maintains circular symmetry. Moreover for small values of aberration there is no significant effect on the intensity distribution, but for large values of aberration the effect is

TH-1501_10612103

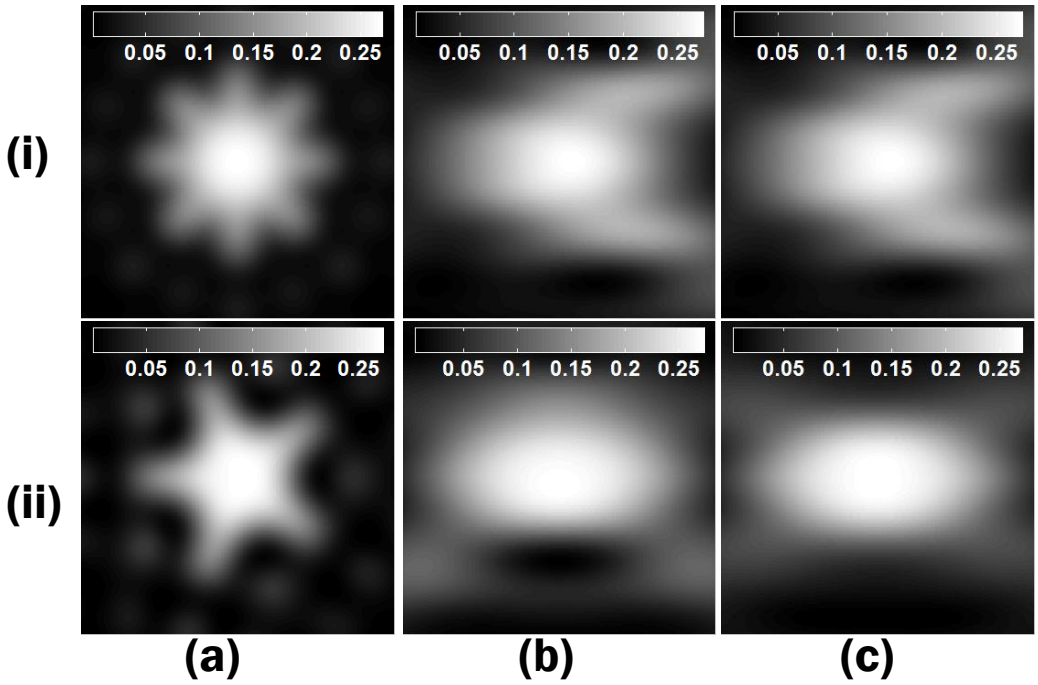

Figure 5.12: The normalized resultant intensity distribution ($I_x + I_y + I_z$) of a radially polarized beam aberrated with ϕ_{rms}=1 radian of positive (i) tetrafoil and (ii) pentafoil in the (a) XY, (b) XZ and (c) YZ planes.

much severe. Further in the case of spherical aberration, the intensity distributions in the XZ and YZ plane are identical and there is a shift in the intensity maximum along the optical axis from the nominal focus, which is more in the case of primary spherical aberration. To be noted that similar axial shift is also observed in the presence of defocus. The line plots of total intensity in Figs. 5.11 (a) and (b) indicate that the effect of primary spherical aberration on the intensity distribution in the XY plane as well as along the optical axis is greater than the effect due to secondary spherical aberration. However as indicated in Fig. 5.11 (c), the Strehl ratio, in the presence of the two aberrations, varies almost identically. In contrast the spread of the focal spot is more rapid due to secondary spherical aberration than due to primary spherical aberration as seen in the 80ER plots in Fig. 5.11 (d).

5.2.5 Effect of tetrafoil and pentafoil

Figure 5.12 shows the resultant intensity distribution in the (a) XY plane, (b) XZ plane and (c)YZ plane in the presence of (i) tetrafoil and (ii) pentafoil with RMS amplitude 1 radian. In the presence of these two aberrations the resultant intensity

TH-1501_10612103

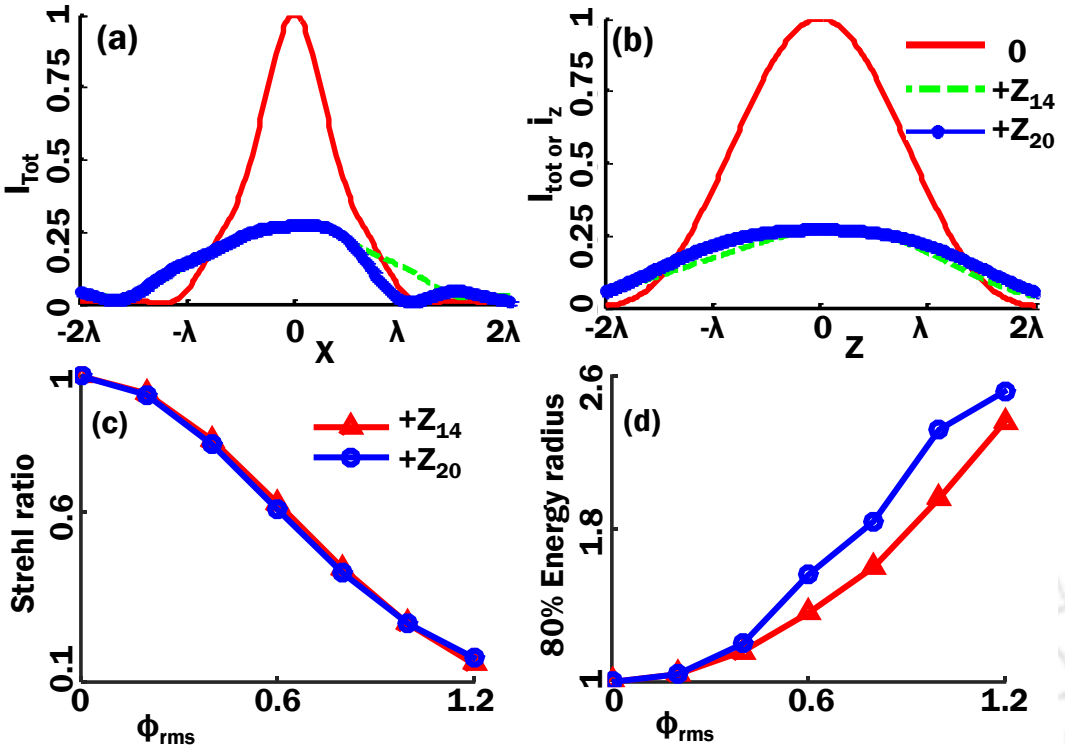

Figure 5.13: (a) Line plot of total intensity in XY plane along the X axis, and (b) line plot of total intensity along the optical axis. Variation of (c) Strehl ratio and (d) 80% energy radius vs the ϕ_{rms} for each of tetrafoil and pentafoil.

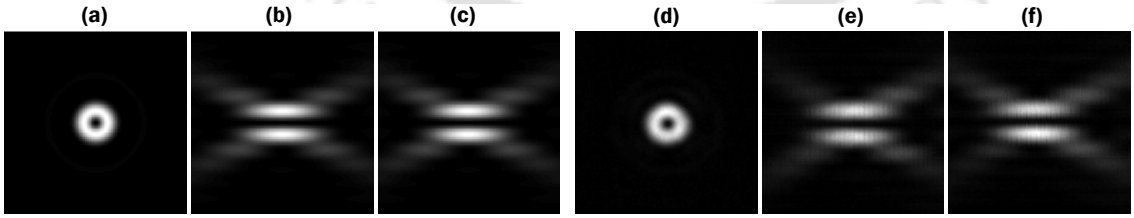

Figure 5.14: Normalized resultant intensity distribution $(I_x + I_y + I_z)$ of a radially polarized beam in aberration free case, in the (a) XY, (b) XZ and (c) YZ planes obtained theoretically and in the (d) XY, (e) XZ and (f) YZ planes obtained experimentally.

TH-1501_10612103

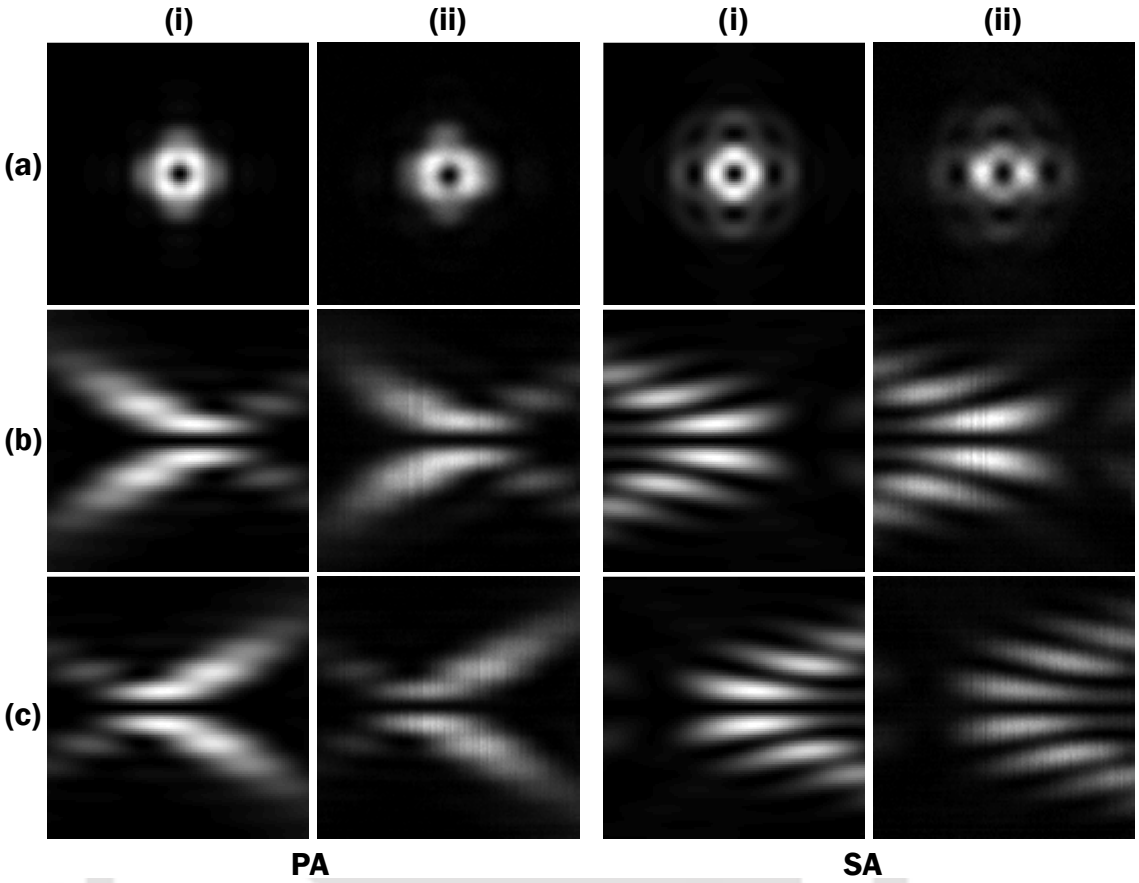

Figure 5.15: Normalized resultant intensity distribution ($I_x + I_y + I_z$) of a radially polarized beam aberrated with ϕ_{rms}=1 radian of positive primary astigmatism (PA) and negative secondary astigmatism (SA) in the (a) XY, (b) XZ and (c) YZ planes obtained (i) numerically and (ii) experimentally.

distribution in the XY plane looses the circular symmetry, even though there exists a 4 and 5 fold planar symmetry. The intensity distributions in XZ and YZ planes are identical for a radially polarized beam in the presence of tetrafoil. Further the resultant intensity distribution is symmetric with respect to the optical axis, although this is asymmetric with respect to the transverse axis. However in the presence of pentafoil the intensity distributions in the XZ and YZ planes are not identical. Figures 5.13 (a) and (b) show the line plots of the total intensity along X and Z axes in the presence of tetrafoil and pentafoil. It is seen that the plot along X is asymmetric with respect to the origin in the presence of pentafoil, while this is symmetric along the optical axis in the presence of both tetrafoil and pentafoil. Figure 5.13 (c) shows that the Strehl ratio in the presence of pentafoil decreases more abruptly for small values of RMS amplitude, while for large RMS amplitudes the decrease is more rapid in the presence of tetrafoil. As seen in 5.13 (d), the 80%

TH-1501_10612103

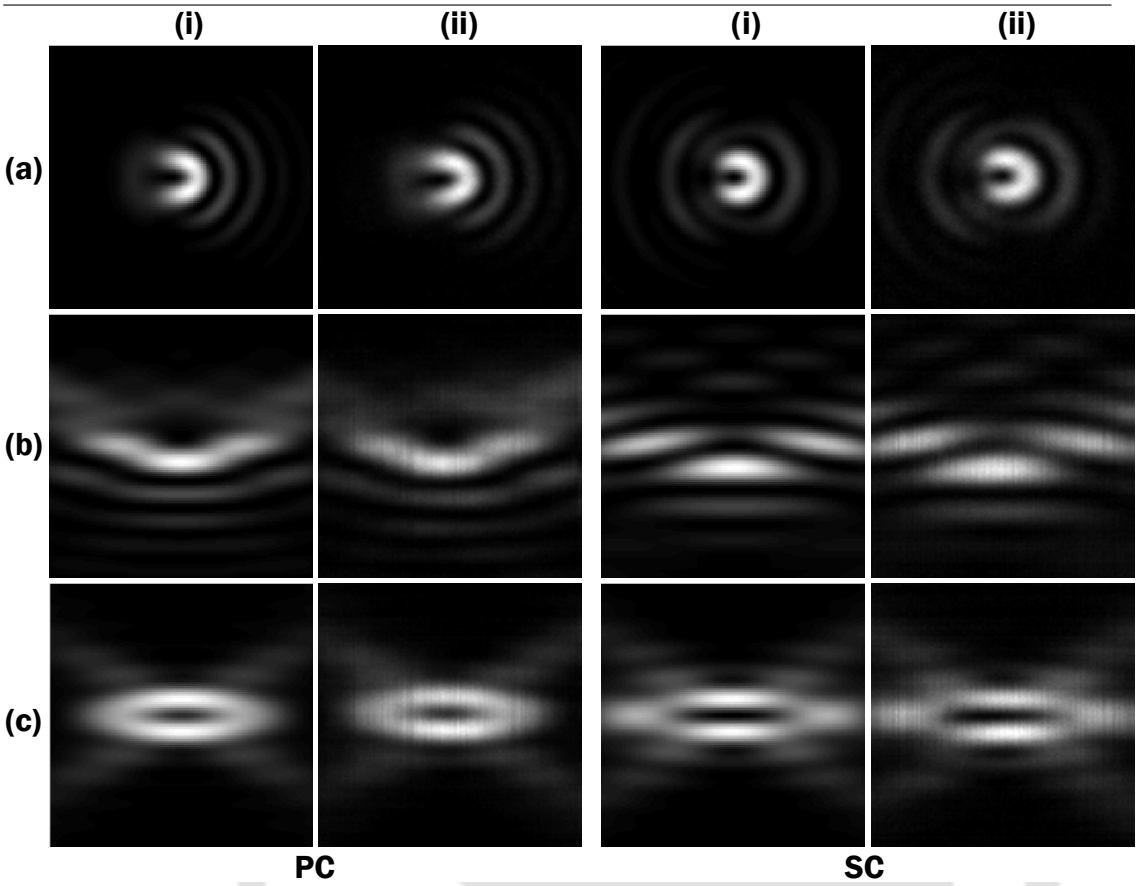

Figure 5.16: Normalized resultant intensity distribution ($I_x + I_y + I_z$) of a radially polarized beam aberrated with ϕ_{rms}=1 radian of positive primary coma (PC) and negative secondary coma (SC) in the (a) XY, (b) XZ and (c) YZ planes obtained (i) numerically and (ii) experimentally.

energy radius increases more rapidly with the magnitude of pentafoil in comparison with tetrafoil.

5.3 Experimental demonstration in the low NA case

We then use our experimental arrangement which is described in chapter 3 to generate a radially polarized beam under low NA focusing condition (NA=0.0056). We also compute the focal intensity distributions theoretically using the same numerical aperture. Figures 5.14 (a), (b) and (c) show the resultant intensity distributions in the XY, XZ and YZ planes, respectively, obtained theoretically and Figs. (d), (e) and (f) show the resultant intensity distributions in the XY, XZ and YZ planes,

TH-1501_10612103

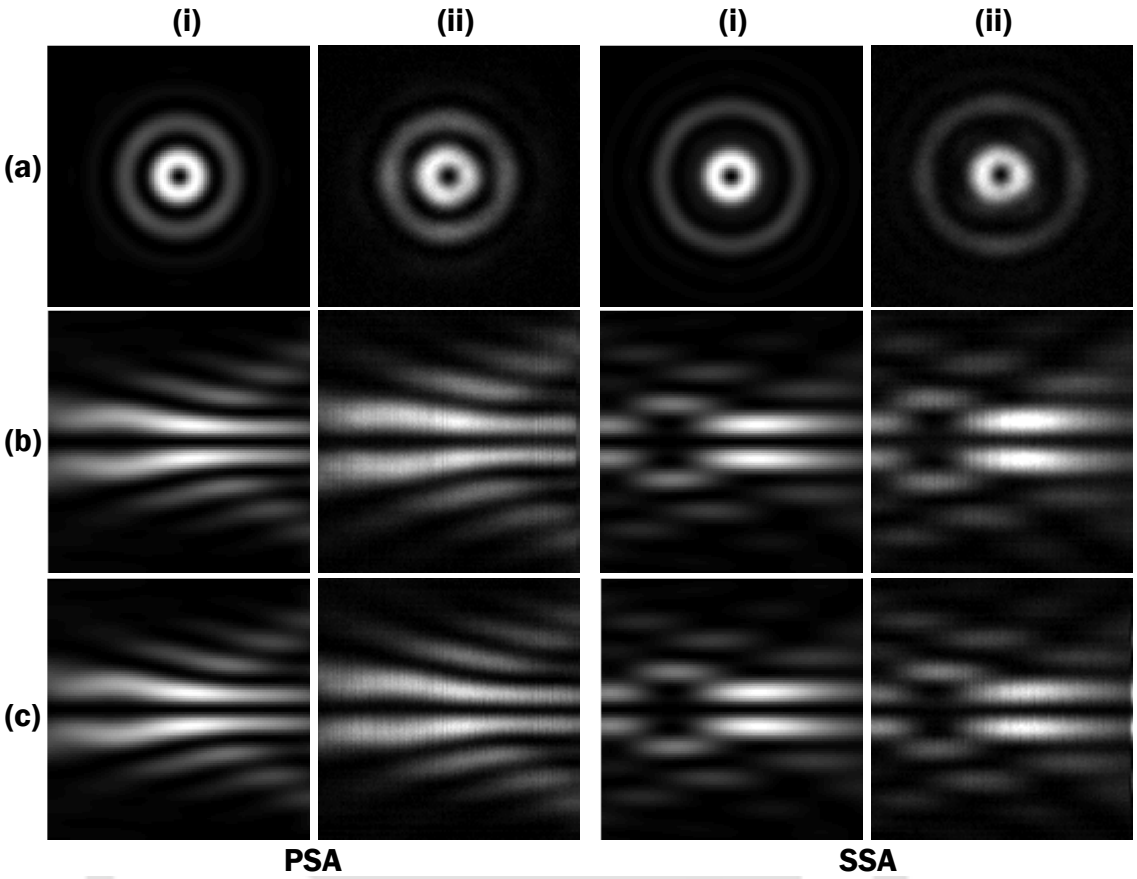

Figure 5.17: Normalized resultant intensity distribution ($I_x + I_y + I_z$) of a radially polarized beam aberrated with ϕ_{rms}=1 radian of positive primary spherical aberration (PSA) and negative secondary spherical aberration (SSA) in the (a) XY, (b) XZ and (c) YZ planes obtained (i) numerically and (ii) experimentally.

respectively, obtained experimentally. The similarity between the two sets of figures indicate the accuracy of the experimental results. It is noticed that in the low NA case there is no Z polarized light appearing on the optical axis thus giving rise to a doughnut shaped intensity distribution in the focal plane.We then use the experimental setup to demonstrate the effect of primary and secondary aberrations in the focal plane of the radially polarized beam in the low NA focusing condition. For each aberration we also perform numerical simulation to generate the respective theoretical intensity distributions.

Figures 5.15 (a), (b) and (c) show the resultant intensity distributions in the focal volume of a radially polarized beam in the XY, XZ and YZ planes, respectively, obtained (i) theoretically and (ii) experimentally aberrated with ϕ_{rms}=1 radian of positive primary astigmatism (PA) and negative secondary astigmatism (SA). Sim-

TH-1501_10612103

ilarly Figs. 5.16 (a), (b) and (c) show the resultant intensity distributions in the focal volume of a radially polarized beam in the XY, XZ and YZ planes, respectively, obtained (i) theoretically and (ii) experimentally aberrated with ϕ_{rms}=1 radian of positive primary coma (PC) and negative secondary coma (SC). From the intensity distributions in the XZ plane and the YZ plane it is seen that primary coma gives rise to a boat-shaped structure in the focal volume, however in the presence of secondary coma such a boat-shaped structure is not formed. Figures 5.17 (a), (b) and (c) show the resultant intensity distributions in the focal volume of a radially polarized beam in the XY, XZ and YZ planes, respectively, obtained (i) theoretically and (ii) experimentally aberrated with ϕ_{rms}=1 radian of positive primary spherical aberration (PSA)and negative secondary spherical aberration (SSA). The close resemblance between the theoretically and experimentally obtained intensity distributions near the focus of the aberrated radially polarized beam validates the theoretical results obtained using the vectorial diffraction theory.

5.4 Conclusion

In this chapter we have investigated the effect of primary and secondary aberrations on the focal volume properties of a radially polarized beam. We have identified certain primary aberrations whose phase profiles are comparable with those of the secondary aberrations. We have provided a comparative study on the focal volume properties of radially polarized beams in the presence of both primary and secondary aberrations. We have noticed from our investigation that in most of the cases the focal volume properties are maximally effected by the primary aberrations compared to the respective secondary aberrations. However as far as the spread of the focal spot is concerned, in most of the cases the secondary aberrations are more influential. The theoretical results obtained with a low NA lens are verified by performing experiments using the division of wavefront based vector beam forming setup.

TH-1501_10612103

Chapter 6

Poynting vector profile of a tightly focused radially polarized beam in the presence of primary aberrations

6.1 Introduction

Poynting vector in the focal volume of a cylindrical vector beam, especially, a radially polarized beam is a very important parameter. The strong on-axis axially polarized field in the focal volume of a tightly focused radially polarized beam has non propagating power [10]. The non propagating power due to the axially polarized field on the optical axis is exhibited by a null Poynting vector. There are two types of forces on an optical trap, namely, the scattering force or the radiation pressure and the gradient force [45, 78]. Of these two forces, the radiation pressure is due to the transfer of linear momentum from the photons onto the trapped particle. Thus the radiation pressure due to a focused beam will be dependent on the Poynting vector profile. Owing to the strong field and zero Poynting vector near the focus, the radially polarized beam offers a strong gradient force and zero radiation pressure [79, 80]. Thus a radially polarized beam has a strong trapping capability when compared to other beams.

Optical trapping, since its invention by Authur ashkin [78, 81], has found applications in diverse fields to trap and manipulate microscopic particles [82]. In the

TH-1501_10612103

initial period, optical trapping primarily dealt with linearly and circularly polarized laser beams. Metallic particles had been treated as difficult to trap due a strong scattering and absorption forces. Recently it has been shown [83] that the metallic particles can be trapped by using vector beams with axially symmetric polarization profile such as the radially polarized beam. In trapping dielectric sphere, the radially polarized beam has higher axial trapping efficiency as compared to a circularly polarized vortex beam [84] and an azimuthally polarized beam [16, 85]. The trapping efficiency of a radially polarized beam is in fact shown to be 1.84 times that of a linearly polarized beam [6]. The radially polarized beam also has the strongest trapping efficiency, amongst linearly and azimuthally polarized beams, to trap gold nano particles [86]. The longitudinal trapping range in an optical trap can be increased by using a radially polarized narrow-width annular beam such that the range is larger than that of the doughnut beam [87]. The radially polarized beams are also used to generate three-dimensional (3D) optical chains for controllable delivery of multiple particles [88].

The unique Poynting vector profile of the radially polarized beam also exhibits superior self-healing properties [89] when the beam passes through a sector-shaped opaque obstacle and a thin lens. Another outcome of the null Poynting vector of a radially polarized beam along the optical axis is the increment in the electric field between two metallic blocks kept at a sub wavelength separation along the optical axis, in the focal volume [90]. Further an unconventional flat-top intensity distribution can be generated by a single radially polarized beam focused by a lens having numerical aperture in the intermediate range [91, 92], where the central part has non propagating power.

The applications described above assume the Poynting vector profile of an unaberrated radially polarized beam. We have observed in the previous chapter how the aberrations effect the focal intensity distribution of a radially polarized beam. It can be expected that the various primary aberrations will also have significant effect on the Poynting vector profile in the focal volume. In this chapter thus we present a detailed study on the Poynting vector profile in the focal volume of a tightly focused radially polarized beam [93], in the presence of various primary monochromatic aberrations.

Under plane wave approximations, the time averaged Poynting vector is equal to the product of the time averaged energy density and the velocity of light in the given medium [29, 30]. In high numerical aperture case, when the rays intersect at large

TH-1501_10612103

angles, such approximations are not useful. Thus we need to use the vectorial focal field expressions, as described earlier in this thesis and extend them to compute the Poynting vector profile near the focus [94].

6.2 Poynting vector profile

In electrodynamics, the Poynting vector represents the directional energy flux density (the rate of energy transfer per unit area) of an electromagnetic field [29]. The SI unit of the Poynting vector is watt per square meter (W/m^2). If E_x, E_y and E_z and H_x, H_y and H_z are electric and magnetic field components, respectively, we can define the Poynting vector as

$$\vec{S} = \vec{E} \times \vec{H} \tag{6.1}$$

In the above the E and H at every point near the focus are given by the vectorial diffraction theory described in chapter 2. From the expression in Eq. 6.1 we can thus compute the Cartesian components of instantaneous Poynting vector, S_x, S_y and S_z. To compute the time averaged Poynting vector, the same expression gets modified as

$$<\vec{S}> = <\vec{E} \times \vec{H}> = \Re(\vec{E} \times \vec{H^*}) \tag{6.2}$$

The Cartesian components of the time averaged Poynting vector, therefore, are

$$\begin{aligned} <S_x> &= \Re(E_y H_z^* - E_z H_y^*) \\ <S_y> &= \Re(E_z H_x^* - E_x H_z^*) \\ <S_z> &= \Re(E_x H_y^* - E_y H_x^*) \end{aligned} \tag{6.3}$$

Here $\Re(...)$ represent the real part of the argument. We define the total time averaged Poynting vector $\langle S_t \rangle$ in terms of $\langle S_x \rangle$, $\langle S_y \rangle$ and $\langle S_z \rangle$ as $\langle S_t \rangle = \sqrt{\langle S_x \rangle^2 + \langle S_y \rangle^2 + \langle S_z \rangle^2}$.

On the other hand, the Cartesian components of the time dependent Poynting vector, considering harmonic time dependence, are given as,

$$S_{X,Y,Z}(t) = S_{X,Y,Z} e^{\frac{i2\pi ct}{\lambda}} \tag{6.4}$$

TH-1501_10612103

6.3 Numerical simulation of the Poynting vector profile

The expressions in the above section are used to compute the Poynting vector profile of a radially polarized beam in the presence of primary aberrations. The computations are performed using a focusing lens of NA=0.9 over a focal volume extending from -3λ to 3λ along X, Y and Z axes with the nominal focus as the origin. For our investigation, we consider primary aberrations such as primary astigmatism, coma, trefoil and spherical aberration, which are represented by single indexed Zernike polynomials, Z_i where (i =5 $\rightarrow$ 11) [21, 39].

The time averaged Poynting vector values in both the aberrated and aberration free cases are normalized by the maximum value of the total time averaged Poynting vector value in the focal plane in the aberration free case. Figure 6.1 (a) shows the normalized time averaged Poynting vector profiles (i) $\langle S_x \rangle$, (ii) $\langle S_y \rangle$ and (iii) $\langle S_z \rangle$ in the XY, XZ and YZ planes of a radially polarized beam in the aberration free case. Every image has a different color bar which is shown at its top by the horizontal bar. It is seen that in the XY plane $\langle S_x \rangle$ and $\langle S_y \rangle$ are zero, and only $\langle S_z \rangle$ contribute to the total Poynting vector. On the other hand there is a considerable amount of $\langle S_x \rangle$ and $\langle S_y \rangle$ in the XZ and YZ planes, respectively. Also each of $\langle S_x \rangle$, $\langle S_y \rangle$ and $\langle S_z \rangle$ is zero along the optical axis indicating that there is no energy flow along the optical axis. Thus there exists an intensity maximum at the focus where there is a null Poynting vector. To be noted that the first column of Fig. 6.1 (a) shows the direction of the axes describing the three planes.

Figure 6.1 (b) shows the normalized time averaged Poynting vector profiles (i) $\langle S_x \rangle$, (ii) $\langle S_y \rangle$ and (iii) $\langle S_z \rangle$ in the XY, XZ and YZ planes of a radially polarized beam in the presence of 1 radian RMS (i.e. ϕ_{rms}) of spherical aberration (Z_{11}). In the presence of spherical aberration there is no significant effect on the Poynting vector profile in the XY plane. Likewise the unaberrated case there is no energy flow along the optical axis. However the Poynting vector profiles in the XZ plane and YZ plane indicate that the net energy flow around the optical axis is through a region that forms a conical nozzle.

Figure 6.2 (a) shows the normalized time averaged Poynting vector profile (i) $\langle S_x \rangle$, (ii) $\langle S_y \rangle$ and (iii) $\langle S_z \rangle$ in the XY, XZ and YZ planes of the focal volume in the presence of 1 radian RMS of astigmatism at $\pm 45^\circ$ (Z_5). It is noticed in the case

TH-1501_10612103

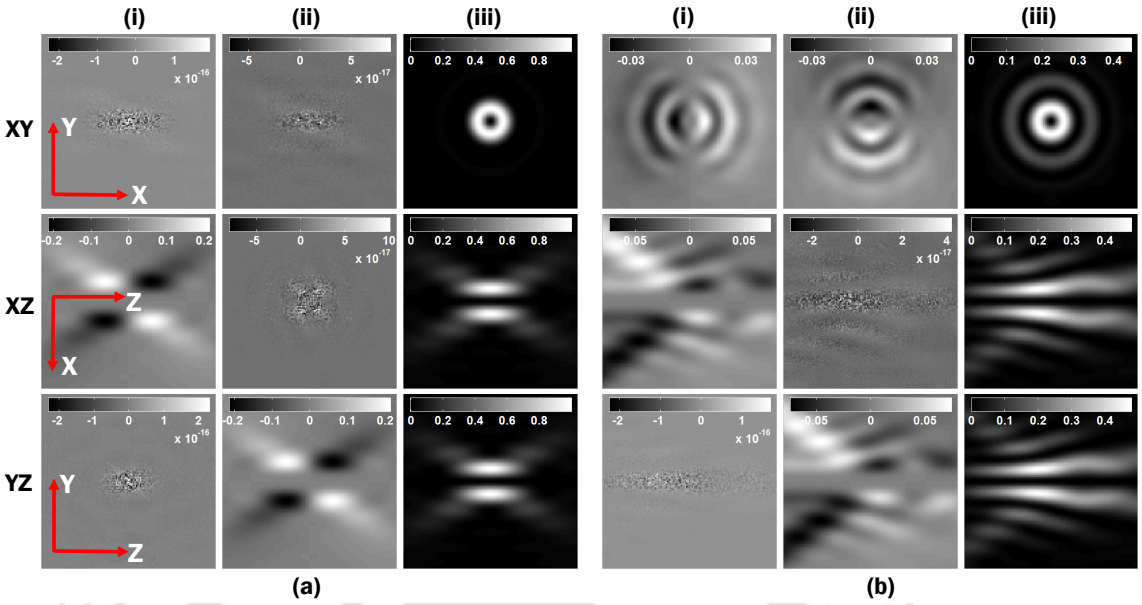

Figure 6.1: Normalized time averaged Poynting vector profiles (i) $\langle S_x \rangle$, (ii) $\langle S_y \rangle$ and (iii) $\langle S_z \rangle$ in the XY, XZ and YZ planes near the focus of a radially polarized beam in (a) the aberration free case and (b) in the presence of 1 radian RMS of spherical aberration (Z_{11}).

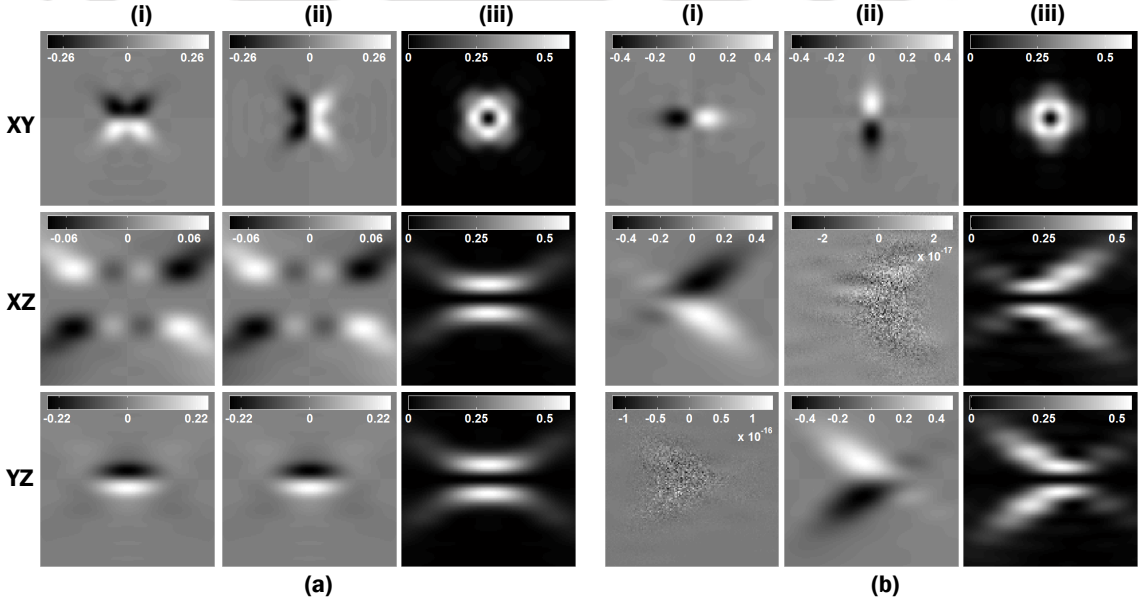

Figure 6.2: Normalized time averaged Poynting vector profiles (i) $\langle S_x \rangle$, (ii) $\langle S_y \rangle$ and (iii) $\langle S_z \rangle$ in the XY, XZ and YZ planes of a radially polarized beam in the presence of 1 radian RMS of (a) astigmatism at $\pm 45°$ (Z_5) and (b) astigmatism at $0°$ (Z_6).

TH-1501_10612103

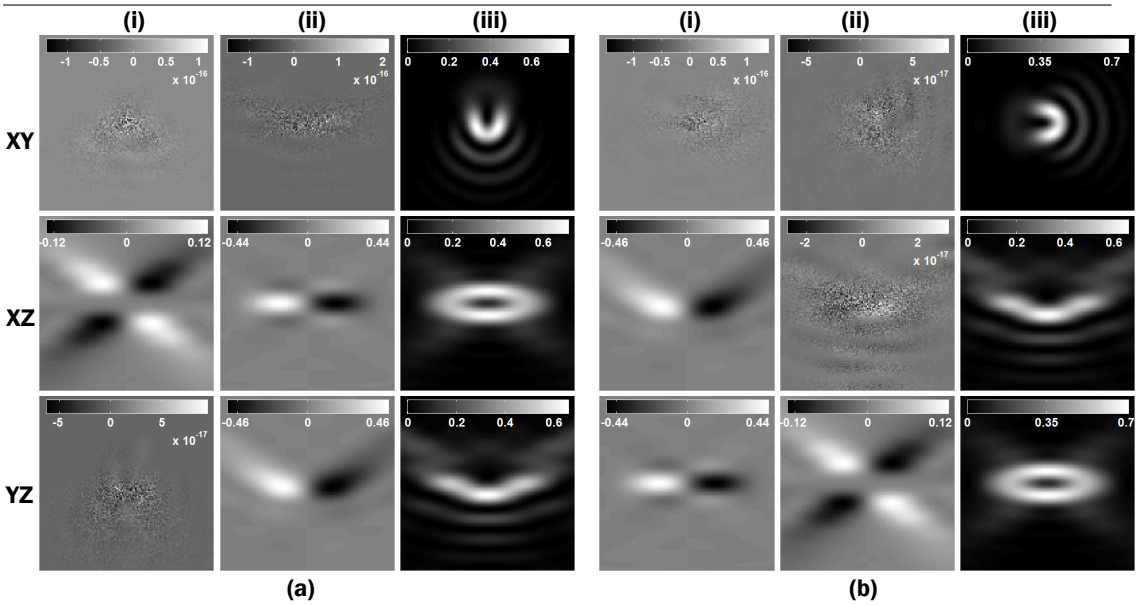

Figure 6.3: Normalized time averaged Poynting vector profiles (i) $\langle S_x \rangle$, (ii) $\langle S_y \rangle$ and (iii) $\langle S_z \rangle$ in the XY, XZ and YZ planes of a radially polarized beam in the presence of 1 radian RMS amplitude of (a) y coma (Z_7) and (b) x coma (Z_8).

of all the three planes that there is a significant amount of $\langle S_x \rangle$ and $\langle S_y \rangle$. Also the Poynting vector profile in the focal plane looses the circular symmetry in the presence of astigmatism, even though there exist a two fold planar symmetry. However there is no energy flow along the optical axis likewise the unaberrated case. Figure 6.2 (b) shows the respective normalized time averaged Poynting vector profiles in the focal volume of a radially polarized beam in the presence of 1 radian RMS of astigmatism at 0° (Z_6).

Figure 6.3 (a) shows the normalized time averaged Poynting vector profiles (i) $\langle S_x \rangle$, (ii) $\langle S_y \rangle$ and (iii) $\langle S_z \rangle$ in the XY, XZ and YZ planes in the focal volume of a radially polarized beam in the presence of 1 radian RMS of y coma (Z_7). It is noticed that in the XY plane the net Poynting vector profile appears asymmetric and there is no contribution from the $\langle S_x \rangle$ and $\langle S_y \rangle$. The asymmetry in the XY plane may lead to a non-zero value of the net Poynting vector at the nominal focus. The profiles in the XZ and YZ planes reveal the presence of a strong $\langle S_t \rangle$ at two locations on the optical axis. In fact the net Poynting vector profile in the focal volume resembles the shape of a boat. Figure 6.3 (b) shows the normalized time averaged Poynting vector profiles in the focal volume of a radially polarized beam in the presence of 1 radian RMS of x coma (Z_8). It is observed that in the presence

TH-1501_10612103

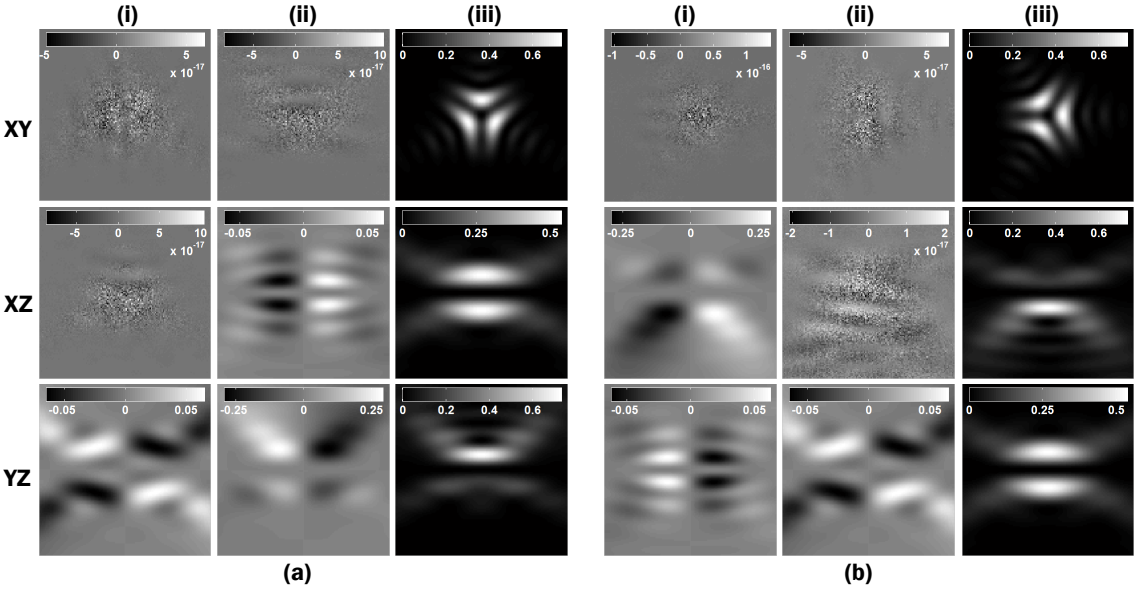

Figure 6.4: Normalized time averaged Poynting vector profiles (i) $\langle S_x \rangle$, (ii) $\langle S_y \rangle$ and (iii) $\langle S_z \rangle$ in the XY, XZ and YZ planes of a radially polarized beam in the presence of 1 radian RMS of (a) y trefoil (Z_9) and (b) x trefoil (Z_{10}).

of either x or y coma there is a significant presence of $\langle S_x \rangle$, or, and $\langle S_y \rangle$ along the optical axis. Thus in the presence of coma there is a non-zero energy flow along the optical axis.

Figures 6.4 (a) and (b) show the normalized time averaged Poynting vector profiles (i) $\langle S_x \rangle$, (ii) $\langle S_y \rangle$ and (iii) $\langle S_z \rangle$ in the XY, XZ and YZ planes in the focal volume of a radially polarized beam aberrated with 1 radian RMS of y trefoil (Z_9) and x trefoil (Z_{10}), respectively. It is seen that even in the presence of x and y trefoil, there is no $\langle S_x \rangle$ and $\langle S_y \rangle$ in the XY plane. Besides there is a disappearance in the circular symmetry of the Poynting vector profile in the focal plane, even though there exists a three fold planar symmetry. Further there appears a significant amount of $\langle S_x \rangle$ and $\langle S_y \rangle$ in the XZ and YZ planes in the presence of x and y trefoils, although along the optical axis there is no energy flow.

We have seen that in the presence of coma there is a non-zero energy flow along the optical axis. To investigate this feature closely we have plotted $\langle S_x \rangle$, $\langle S_y \rangle$ and $\langle S_z \rangle$ along the optical axis, as shown in Fig. 6.5 (a). It is noticed that there exist a non-zero $\langle S_x \rangle$ and $\langle S_z \rangle$ along the optical axis in the presence of x coma, and non-zero $\langle S_y \rangle$ and $\langle S_z \rangle$ in the presence of y coma. The $\langle S_x \rangle$ and $\langle S_y \rangle$ maximize their values with opposite signs at distances $\pm 1.5\lambda$ from the focal point. To observe the

TH-1501_10612103

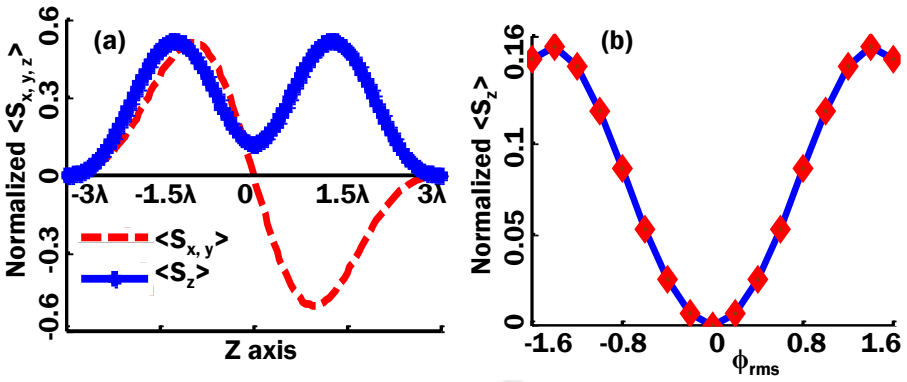

Figure 6.5: (a) Line plot of $\langle S_x \rangle$ and $\langle S_z \rangle$ in the presence of x coma or $\langle S_y \rangle$ and $\langle S_z \rangle$ in the presence of y coma both with ϕ_{rms}=1 radian, along the optical axis from -3λ to 3λ on the two sides of the nominal focus, (b) variation of central value of the Poynting vector profile with ϕ_{rms} variation in between -1.6 radian to 1.6 radian.

variation of the net Poynting vector value at the focal point with RMS amplitude, we have plotted the net Poynting vector value at the focus with RMS amplitude of coma varying between -1.6 radian to 1.6 radian, as shown in Fig. 6.5 (b). Initially the Poynting vector at the focus is zero, however, as RMS amplitude increases, it also increases and becomes 0.16 at RMS amplitude equal to 1.4. Further increase in the RMS amplitude results in a decrease in the central value of the Poynting vector.

6.3.1 Time dependence of the Poynting vector profile

In the previous section we have discussed the time averaged Poynting vector profile in the focal volume of a radially polarized beam in the presence of various primary aberrations. However the time averaged profile can not entirely depict the time dependent behavior of the Poynting vector values. In this section we discuss the effect of primary aberrations on the time dependent Poynting vector profile. To observe the time dependence of Poynting vector profile, we have computed $S_{x,y,z}(t)$ at different time instants by using Eq. 6.4, over a volume extending along X, Y and Z axes are from -λ to λ. Here we use amplitude and phase values of $S_{x,y,z}(t)$ to draw 3D Poynting vector ellipses to represent the time evolution of the Poynting vector profile. The tip of the instantaneous Poynting vector is used to draw the ellipse while the origin of the vector coincides the location at which the Poynting vector is computed. For the visualization, we have considered few representative points (i.e. 9 locations), on the optical axis and on the 0.5λ radius circle, which are separated

TH-1501_10612103

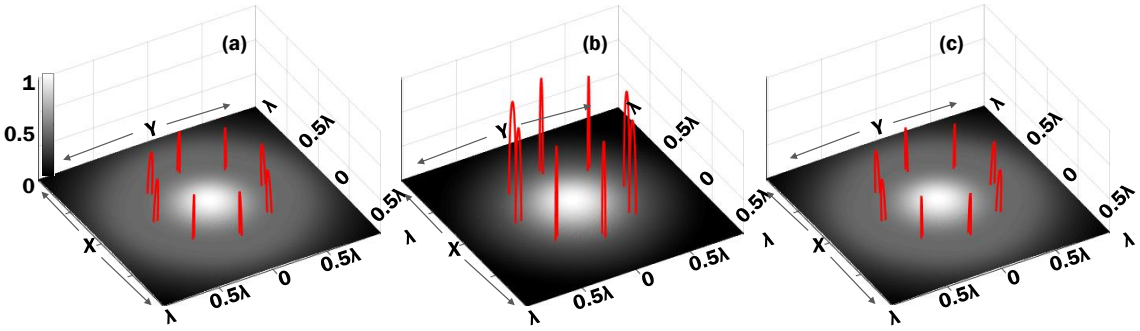

Figure 6.6: Time evolution of the Poynting vector profile of a tightly focused radially polarized beam in the (a) z=-λ, (b) focal and (c) z=λ planes in the aberration free case. The Poynting vector ellipses are overlaid on the respective intensity distributions over an area described by (x, y)= -λ to λ.

by 45° angular separation starting from the X axis. Every time dependent Poynting vector component is scaled by the same factor in all the planes and in the case of all the primary aberrations.

In order to investigate the relative axial deformation caused by primary aberrations, we have considered three planes perpendicular to the optical axis, at z=-λ, 0 and +λ. The time evolution of the instantaneous Poynting vector is overlaid on the normalized intensity distribution (while the intensity distribution is normalized by the respective maximum value of intensity) of the radially polarized beam both in the aberration free and aberrated cases. Figure 6.6 shows the time evolution of the Poynting vector profile in the aberration free case in the (i) z=-λ, (ii) focal and (iii) z=+λ planes. It is seen that the Poynting vector ellipses in the focal plane have large semi major axes and small semi minor axes, while in z= $\pm\lambda$ planes the semi major axes of the ellipses decrease in size as compared to the focal plane. Besides in the z= $\pm\lambda$ planes the Poynting vector ellipses are tilted in opposite directions with respect to the Z axis.

Figure 6.7 (i) shows the time evolution of the instantaneous Poynting vector in the presence of ϕ_{rms}=1 radian astigmatism at 0° in the (a) z= -λ, (b) focal and (c) z=+λ planes. In the presence of astigmatism at 0°, in the focal plane, the maximum intensity locations corresponds to large semi major axis ellipses which have much smaller semi minor axes and are tilted with respect to Z axis. The intensity minimum locations, on the other hand, have negligible semi major axes ellipses. In z=$\pm\lambda$ planes, the maximum intensity locations have smaller semi major axis ellipses and relatively large semi minor axes. In the presence of ϕ_{rms}=1 radian

TH-1501_10612103

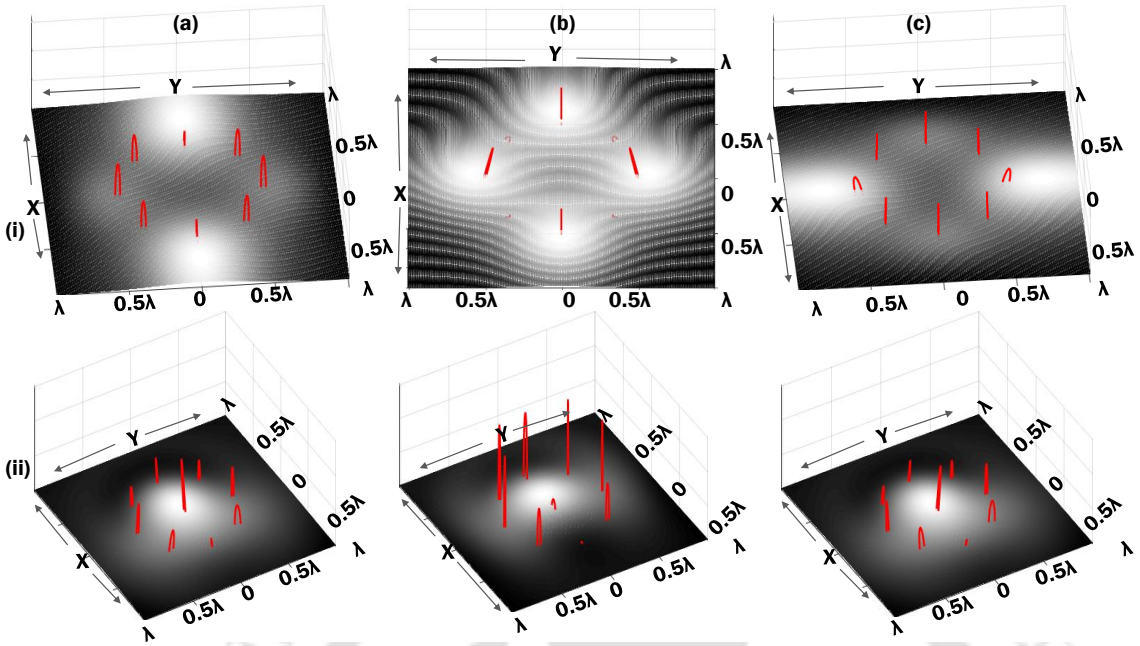

Figure 6.7: Time evolution of the Poynting vector profile of a tightly focused radially polarized beam in the (a) z=-λ, (b) focal and (c) z=λ planes, in the presence of (i) astigmatism at 0° and (ii) x coma both with ϕ_{rms}=1 radian. The Poynting vector ellipses are overlaid on the respective intensity distributions over an area described by (x, y)= -λ to λ.

x coma, as in Figs. 6.7 (ii) (a-c), it is seen that the ellipses have larger semi major axes in the focal plane relative to the other two planes. In all the three planes one can see the existence of Poynting vector ellipse at the center of the focal volume. While in the z=±λ planes, the ellipses have larger semi minor and smaller semi major axes when compared to the focal plane ellipses.

Figures 6.8 (a) and (b) show the time evolution of the Poynting vector profile in the focal volume in the presence of x trefoil and spherical aberration, respectively, in the (i) z=-λ, (ii) focal and (iii) z=+λ planes. In the presence of x trefoil, in the focal plane, it is noticed that the Poynting vector ellipses along the circle of radius of 0.5λ have large semi major axes at the locations of maximum intensity and smaller semi major axes at the locations of minimum intensity. On the other hand the ellipses at the same locations in the other two planes have semi major axes, which are of comparable magnitude. Further, the ellipses in z=±λ planes are tilted in opposite directions with respect to the Z axis. In the presence of spherical aberration, the Poynting vector ellipses on the 0.5λ circle maintain a symmetric profile. It is noticed that in z=-λ plane ellipses have larger semi major axes as compared to z=λ plane

TH-1501_10612103

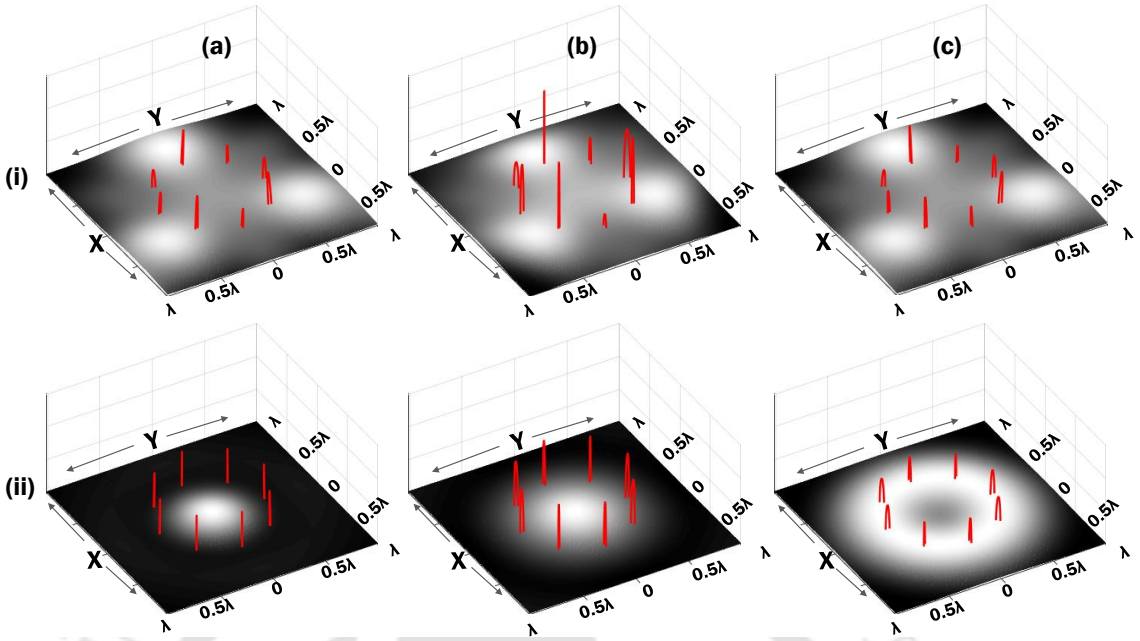

Figure 6.8: Time evolution of the Poynting vector profile of a tightly focused radially polarized beam in the (a) z=-λ, (b) focal and (c) z=λ planes in the presence of ϕ_{rms}= 1 radian of (i) x trefoil and (ii) spherical aberration. The Poynting vector ellipses are overlaid on the respective intensity distributions over an area described by (x, y)= -λ to λ.

ellipses.

6.4 Conclusion

In this chapter, we have investigated the Poynting vector profile near the focus of a radially polarized beam in the presence of various primary aberrations. We have simulated both the time averaged and time dependent Poynting vector profiles. Here we have noticed that even in the presence of astigmatism, trefoil and spherical aberration, there is no energy flow along the optical axis. In the presence of coma there exists non-zero Poynting vector along the optical axis and also at the focal point. The net Poynting vector value at the focus increases with RMS amplitude and for NA=0.9 it attains the highest value at RMS amplitude equal to 1.4 radian. Further increase in RMS amplitude results in decrease in the net Poynting vector value. Here we have also showed the time dependence of the instantaneous Poynting vector at certain representative locations in the focal volume of the radially polarized beam in the presence of various primary aberrations.

TH-1501_10612103

Chapter 7

Conclusion and future prospect

7.1 Conclusion

Cylindrical vector beams have drawn a lot of interest in recent years due to their interesting and unique properties resulting in applications in various fields. These beams have pupil planes comprising circularly symmetric polarization profiles. Two important members of the cylindrical vector beam are the azimuthally polarized beam and the radially polarized beam. The focal volumes of these beams have interesting properties. The pupil plane of the azimuthally polarized beam has electric field vectors oriented in the azimuthal direction while that of the radially polarized beam has electric field vectors oriented in the radial direction. When focused the azimuthally polarized beam gives rise to a doughnut pattern in the focal plane. Thus the intensity distribution in the focal plane has a dark centre surrounded by an intense ring of light. The radially polarized beam, when focused by a high numerical aperture lens, gives rise to a circularly symmetric intensity distribution in the focal plane with intensity maximum occurring at the centre. The intensity at the centre is contributed purely by an axially polarized field which has non propagating power. The applications of the two beams exploiting their unique properties assume the respective cylindrical vector beam to be unaberrated. However any optical system will always suffer from aberrations to a degree that may vary from one system to another. So far there has not been any comprehensive study on the effect of aberrations on these two important cylindrical vector beams, especially, when the aberration effects on the entire focal volume is concerned. In this thesis we have used the vectorial diffraction theory to perform a detailed investigation on various beam

TH-1501_10612103

parameters over an entire volume near the focus. Our theoretical results, in the low numerical aperture focusing case, are also verified by performing experiments. Below we provide a chapter wise conclusion of the entire thesis work.

In chapter 1, we have provided a general introduction to the research problem discussed in this thesis followed by a chapter wise overview of the entire thesis..

In chapter 2, we have introduced vectorial diffraction theory, more specifically the Fourier transform based vectorial diffraction theory, that is needed to compute the Cartesian components of the electric and magnetic field near the focal point of a tightly focused beam. We initiated our discussion with the theory of Richards and Wolf and showed how this integral form can be converted to a Fourier transform form. We showed two versions of the Fourier transform form of the vectorial diffraction theory. We have also developed the expressions to convert the pixel units associated with the numerical computation to real distance units. We then showed how the focal field expressions get modified in the presence of aberrations in the beam.

In chapter 3 we have investigated the effect of primary aberrations on the focal volume properties of an azimuthally polarized beam. We have used the Fourier transform form of the Vectorial diffraction theory to first compute the Cartesian field components in the focal volume in the presence of various primary aberrations using a high NA lens. It is observed that in the presence of astigmatism, coma and trefoil, the circular symmetry of the intensity distribution in the focal plane is broken. Moreover in the presence of coma there appears a significant amount of transversely polarized light on the optical axis. From our results we have also drawn polarization ellipses to indicate the time evolution of the resultant electric field vector in the focal volume of the aberrated azimuthally polarized beam. We have observed that in the presence of astigmatism, coma and trefoil, the light in the focal volume does not remain linearly polarized as in some region it becomes elliptically polarized. Our investigation suggests that in the presence of spherical aberration, the focal intensity distribution remains axially symmetric with no light appearing on the optical axis. Our results further showed that in the presence of a moderate amount of coma, the intensity distribution near the focus takes a boat-like shape. It gives us an elongated dark region surrounded by light in all but one direction. This chapter also describes a division of wavefront based arbitrary vector beam forming setup which can be used to generate cylindrical vector beams with user defined phase profile in the pupil plane. We have presented experimental

TH-1501_10612103

results for an azimuthally polarized beam focused by a low NA lens in the presence of various primary aberrations. The experimentally obtained results agree well with the corresponding results obtained numerically.

It is known that an azimuthally polarized beam with a helical phase mask and a linearly polarized beam have similar kind of focal intensity distributions. Thus the former beam can be used as an alternative to the latter beam. Due to this similarity, in chapter 4, it is intended to investigate the effect of primary aberrations on the two types of beams. Here we observed that the azimuthally polarized beam with a helical phase mask is more resistant to the primary aberrations as far as spread of the focal energy around the centre is concerned. The same beam also provides a better performance in terms of the Strehl ratio in the presence of primary astigmatism when compared to the X polarized beam. Thus the azimuthally polarized beam with a helical phase mask can provide superior resilience to primary aberrations and especially to astigmatism relative to a linearly polarized beam. We have also demonstrated the aberration effect on the azimuthally polarized beam with a helical phase mask experimentally, taking a low NA focusing lens. The theoretical predictions regarding aberration resilience of the APBH compared to the X polarized beam, have been verified experimentally under low NA focusing condition.

There has already been studies on the effect of primary aberrations on the radially polarized beam. In chapter 5 we have investigated the effect of both the primary and secondary aberrations on the focal volume properties of a radially polarized beam. We have identified certain primary aberrations whose phase profiles are comparable with those of the secondary aberrations. We then provided a comparative study on the focal volume properties of radially polarized beam in the presence of both primary and secondary aberrations. Our investigation has revealed that in most of the cases the focal volume properties are maximally effected by the primary aberrations compared to the respective secondary aberrations. However as far as the spread of the focal spot is concerned, in most of the cases the secondary aberrations are more influential. The theoretical results obtained with a low NA lens are verified by performing experiments using the division of wavefront based vector beam forming setup.

For applications such as optical trapping, the Poynting vector value near the focus of a radially polarized beam is very much crucial. Therefore in chapter 6, we have investigated the Poynting vector profile of a radially polarized beam in the presence of various primary aberrations. We have simulated both the time averaged

TH-1501_10612103

and time dependent Poynting vector profiles. Here we have noticed that even in the presence of astigmatism, trefoil and spherical aberration, there is no energy flow along the optical axis. In the presence of coma, however, there exists non-zero Poynting vector along the optical axis and also at the focal point. The net Poynting vector value at the focus increases with the RMS amplitude and for NA=0.9 it attains the highest value at RMS amplitude equal to 1.4 radian. Further increase in RMS amplitude results in a reduction in the net Poynting vector value. Here we have also showed the time dependence of the instantaneous Poynting vector at certain representative locations in the focal volume of a radially polarized beam in the presence of various primary aberrations.

7.2 Future prospect

In this thesis we have theoretically analyzed the polarization profile of the cylindrical vector beams in the presence of various aberrations. However the theoretically obtained polarization profiles are not experimentally verified. Thus in future the experimental arrangement can be further developed to be able to estimate the polarization at each point near the focus of the beam.

Also the experimental results presented in this thesis corresponds to a low numerical aperture lens. In future the experimental arrangement can be upgraded to investigate the high numerical focusing as well.

We have observed that an azimuthally polarized beam with a helical phase mask provides us a focal spot that offers superior resistance to aberrations, especially, to astigmatism. In this thesis aberrations have been introduced separately and not in a group. Thus it will be interesting to see the behaviour of the beam when a combination of aberrations are introduced in the pupil plane.

Further, there can be experiments such as using an optical trapping setup to measure the average Poynting vector so that the theoretical findings on the Poynting vector can be verified.

Moreover in our numerical investigations we have used uniform amplitude profiles for the two cylindrical vector beams. In contrast a realistic beam will have a Gaussian amplitude profile. Thus our numerical investigations can be extended to Gaussian amplitude profiles.

TH-1501_10612103

References

[1] B. Richards and E. Wolf. Electromagnetic diffraction in optical systems. ii. structure of the image field in an aplanatic system. *Proceedings of the Royal Society of London A: Mathematical, Physical and Engineering Sciences*, 253 (1274):358–379, 1959. ISSN 0080-4630. doi: 10.1098/rspa.1959.0200. 29, 31, 32, 37

[2] R. Dorn, S. Quabis, and G. Leuchs. Sharper focus for a radially polarized light beam. *Phys. Rev. Lett.*, 91:233901, Dec 2003. doi: 10.1103/PhysRevLett.91.233901. URL `http://link.aps.org/doi/10.1103/PhysRevLett.91.233901`. 29, 75

[3] Qiwen Zhan. Trapping metallic rayleigh particles with radial polarization. *Opt. Express*, 12(15):3377–3382, Jul 2004. doi: 10.1364/OPEX.12.003377. URL `http://www.opticsexpress.org/abstract.cfm?URI=oe-12-15-3377`. 30

[4] Shaohui Yan and Baoli Yao. Radiation forces of a highly focused radially polarized beam on spherical particles. *Phys. Rev. A*, 76:053836, Nov 2007. doi: 10.1103/PhysRevA.76.053836. URL `http://link.aps.org/doi/10.1103/PhysRevA.76.053836`. 30

[5] Hikaru Kawauchi, Kazuhiro Yonezawa, Yuichi Kozawa, and Shunichi Sato. Calculation of optical trapping forces on a dielectric sphere in the ray optics regime produced by a radially polarized laser beam. *Opt. Lett.*, 32(13):1839–1841, Jul 2007. doi: 10.1364/OL.32.001839. URL `http://ol.osa.org/abstract.cfm?URI=ol-32-13-1839`. 30

[6] Masaki Michihata, Terutake Hayashi, and Yasuhiro Takaya. Measurement of axial and transverse trapping stiffness of optical tweezers in air using a radially polarized beam. *Appl. Opt.*, 48(32):6143–6151, Nov 2009. doi: 10.1364/AO.48.

TH-1501_10612103

006143. URL http://ao.osa.org/abstract.cfm?URI=ao-48-32-6143. 30, 108

[7] Colin JR Sheppard and Amarjyoti Choudhury. Annular pupils, radial polarization, and superresolution. *Applied optics*, 43(22):4322–4327, 2004. 30

[8] V G Niziev and A V Nesterov. Influence of beam polarization on laser cutting efficiency. *Journal of Physics D: Applied Physics*, 32(13):1455, 1999. URL http://stacks.iop.org/0022-3727/32/i=13/a=304. 30

[9] EYS Yew and CJR Sheppard. Second harmonic generation polarization microscopy with tightly focused linearly and radially polarized beams. *Optics communications*, 275(2):453–457, 2007. 30

[10] L. Novotny, M. R. Beversluis, K. S. Youngworth, and T. G. Brown. Longitudinal field modes probed by single molecules. *Phys. Rev. Lett.*, 86:5251–5254, Jun 2001. doi: 10.1103/PhysRevLett.86.5251. URL http://link.aps.org/doi/10.1103/PhysRevLett.86.5251. 30, 107

[11] Haifeng Wang, Luping Shi, Boris Lukyanchuk, Colin Sheppard, and Chong Tow Chong. Creation of a needle of longitudinally polarized light in vacuum using binary optics. *Nature Photonics*, 2(8):501–505, 2008. 30

[12] KB Rajesh, N Veerabagu Suresh, PM Anbarasan, K Gokulakrishnan, and G Mahadevan. Tight focusing of double ring shaped radially polarized beam with high na lens axicon. *Optics & Laser Technology*, 43(7):1037–1040, 2011. 30

[13] Geo M Philip and Nirmal K Viswanathan. Long-range longitudinally-polarized optical needle beam. In *Frontiers in Optics*, pages FW4F–4. Optical Society of America, 2013. 30

[14] Fei Peng, Baoli Yao, Shaohui Yan, Wei Zhao, and Ming Lei. Trapping of low-refractive-index particles with azimuthally polarized beam. *J. Opt. Soc. Am. B*, 26(12):2242–2247, Dec 2009. doi: 10.1364/JOSAB.26.002242. URL http://josab.osa.org/abstract.cfm?URI=josab-26-12-2242. 30

[15] Yiming Dong, Fei Wang, Chengliang Zhao, and Yangjian Cai. Effect of spatial coherence on propagation, tight focusing, and radiation forces of an azimuthally

TH-1501_10612103

polarized beam. *Phys. Rev. A*, 86:013840, Jul 2012. doi: 10.1103/PhysRevA.86.013840. URL `http://link.aps.org/doi/10.1103/PhysRevA.86.013840`. 30

[16] Yuichi Kozawa and Shunichi Sato. Optical trapping of micrometer-sized dielectric particles by cylindrical vector beams. *Opt. Express*, 18(10):10828–10833, May 2010. doi: 10.1364/OE.18.010828. URL `http://www.opticsexpress.org/abstract.cfm?URI=oe-18-10-10828`. 30, 108

[17] M Meier, V Romano, and T Feurer. Material processing with pulsed radially and azimuthally polarized laser radiation. *Applied Physics A*, 86(3):329–334, 2007. 30, 55

[18] David P. Biss, Kathleen S. Youngworth, and Thomas G. Brown. Dark-field imaging with cylindrical-vector beams. *Appl. Opt.*, 45(3):470–479, Jan 2006. doi: 10.1364/AO.45.000470. URL `http://ao.osa.org/abstract.cfm?URI=ao-45-3-470`. 30

[19] Jessica C Mullen, Michael P Buric, Benjamin T Chorpening, and Steven D Woodruff. Azimuthal polarization for raman enhancement in capillary waveguides. *Optical Engineering*, 52(11):117103–117103, 2013. 30, 55

[20] Kathleen S. Youngworth and Thomas G. Brown. Inhomogenous polarization in scanning optical microscopy. *Proc. SPIE*, 3919:75–85, 2000. doi: 10.1117/12.384181. URL `http://dx.doi.org/10.1117/12.384181`. 30

[21] Virendra N. Mahajan. Zernike circle polynomials and optical aberrations of systems with circular pupils. *Appl. Opt.*, 33(34):8121–8124, Dec 1994. doi: 10.1364/AO.33.008121. URL `http://ao.osa.org/abstract.cfm?URI=ao-33-34-8121`. 31, 53, 56, 76, 110

[22] Rishi Kant. An analytical solution of vector diffraction for focusing optical systems with seidel aberrations: I. spherical aberration, curvature of field, and distortion. *Journal of Modern Optics*, 40(11):2293–2310, 1993. 31, 75

[23] Rishi Kant. An analytical method of vector diffraction for focusing optical systems with seidel aberrations ii: Astigmatism and coma. *Journal of Modern Optics*, 42(2):299–320, 1995. doi: 10.1080/09500349514550291. URL `http://dx.doi.org/10.1080/09500349514550291`. 31, 75

TH-1501_10612103

[24] David Biss and T. Brown. Primary aberrations in focused radially polarized vortex beams. *Opt. Express*, 12(3):384–393, Feb 2004. doi: 10.1364/OPEX.12.000384. URL `http://www.opticsexpress.org/abstract.cfm?URI=oe-12-3-384`. 31, 91

[25] Rakesh Kumar Singh, P Senthilkumaran, and Kehar Singh. Effect of coma on the focusing of an apertured singular beam. *Optics and lasers in engineering*, 45(4):488–494, 2007. 31

[26] Rakesh Kumar Singh, P Senthilkumaran, and Kehar Singh. Tight focusing of vortex beams in presence of primary astigmatism. *JOSA A*, 26(3):576–588, 2009. 31, 55

[27] Suhui Deng, Li Liu, Ya Cheng, Ruxin Li, and Zhizhan Xu. Effects of primary aberrations on the fluorescence depletion patterns of sted microscopy. *Optics express*, 18(2):1657–1666, 2010. 31

[28] BR Boruah and MAA Neil. Focal field computation of an arbitrarily polarized beam using fast fourier transforms. *Optics Communications*, 282(24):4660–4667, 2009. 31, 32, 43, 55

[29] John David Jackson. *Classical electrodynamics*, volume 3. Wiley New York etc., 1962. 31, 108, 109

[30] Max Born and Emil Wolf. *Principles of optics: electromagnetic theory of propagation, interference and diffraction of light*. CUP Archive, 1999. 36, 37, 70, 108

[31] Joseph W Goodman et al. *Introduction to Fourier optics*, volume 2. McGraw-hill New York, 1968. 36

[32] VS Ignatowsky. Diffraction by a lens of arbitrary aperture. *Trans. Opt. Inst*, 1 (4):1–36, 1919. 37

[33] JA Stratton and LJ Chu. Diffraction theory of electromagnetic waves. *Physical Review*, 56(1):99, 1939. 37

[34] Julius Adams Stratton. *Electromagnetic theory*, volume 33. John Wiley & Sons, 2007. 37

TH-1501_10612103

[35] E. Wolf. Electromagnetic diffraction in optical systems. i. an integral representation of the image field. *Proceedings of the Royal Society of London A: Mathematical, Physical and Engineering Sciences*, 253(1274):349–357, 1959. ISSN 0080-4630. doi: 10.1098/rspa.1959.0199. 37

[36] M. Mansuripur. Certain computational aspects of vector diffraction problems. *J. Opt. Soc. Am. A*, 6(6):786–805, Jun 1989. doi: 10.1364/JOSAA.6.000786. URL `http://josaa.osa.org/abstract.cfm?URI=josaa-6-6-786`. 43

[37] Marcel Leutenegger, Ramachandra Rao, Rainer A. Leitgeb, and Theo Lasser. Fast focus field calculations. *Opt. Express*, 14(23):11277–11291, Nov 2006. doi: 10.1364/OE.14.011277. URL `http://www.opticsexpress.org/abstract.cfm?URI=oe-14-23-11277`. 43

[38] Steven W Smith et al. *The scientist and engineer's guide to digital signal processing*. California Technical Pub. San Diego, 1997. 49

[39] Robert J Noll. Zernike polynomials and atmospheric turbulence. *J. Opt. Soc. Am.*, 66(3):207–211, 1976. 53, 110

[40] Kathleen Youngworth and Thomas Brown. Focusing of high numerical aperture cylindrical-vector beams. *Opt. Express*, 7(2):77–87, Jul 2000. doi: 10.1364/OE.7.000077. URL `http://www.opticsexpress.org/abstract.cfm?URI=oe-7-2-77`. 55

[41] Qiwen Zhan. Cylindrical vector beams: from mathematical concepts to applications. *Adv. Opt. Photon.*, 1(1):1–57, Jan 2009. doi: 10.1364/AOP.1.000001. URL `http://aop.osa.org/abstract.cfm?URI=aop-1-1-1`. 55, 75

[42] Meng He, Ziyang Chen, Shunhong Sun, and Jixiong Pu. Propagation properties and self-reconstruction of azimuthally polarized non-diffracting beams. *Optics Communications*, 294:36–42, 2013. 55

[43] Stefan W Hell and Jan Wichmann. Breaking the diffraction resolution limit by stimulated emission: stimulated-emission-depletion fluorescence microscopy. *Optics letters*, 19(11):780–782, 1994. 55

[44] Svetlana N. Khonina and Ilya Golub. How low can sted go? comparison of different write-erase beam combinations for stimulated emission depletion

TH-1501_10612103

microscopy. *J. Opt. Soc. Am. A*, 29(10):2242–2246, Oct 2012. doi: 10.1364/JOSAA.29.002242. URL http://josaa.osa.org/abstract.cfm?URI=josaa-29-10-2242. 55

[45] Timo A Nieminen, Norman R Heckenberg, and Halina Rubinsztein-Dunlop. Forces in optical tweezers with radially and azimuthally polarized trapping beams. *Optics letters*, 33(2):122–124, 2008. 55, 107

[46] Liu Yong and Chen Jiabi. Effect of primary spherical aberration on focusing field of cylindrical-vector bessel-gaussian beams. *Acta Optica Sinica*, 29(7): 1996–1999, 2009. 55, 91

[47] Rakesh Kumar Singh, P. Senthilkumaran, and Kehar Singh. Structure of a tightly focused vortex beam in the presence of primary coma. *Optics Communications*, 282(8):1501 – 1510, 2009. ISSN 0030-4018. doi: http://dx.doi.org/10.1016/j.optcom.2008.11.085. URL http://www.sciencedirect.com/science/article/pii/S0030401808012376. 55

[48] Yaakov Lumer, Inon Moshe, Avi Meir, Yotam Paiken, Galina Machavariani, and Steven Jackel. Effects of thermally induced aberrations on radially and azimuthally polarized beams. *J. Opt. Soc. Am. B*, 24(9):2279–2286, Sep 2007. doi: 10.1364/JOSAB.24.002279. URL http://josab.osa.org/abstract.cfm?URI=josab-24-9-2279. 56

[49] Yangjian Cai, Qiang Lin, Halil T. Eyyuboglu, and Yahya Baykal. Average irradiance and polarization propertiesof a radially or azimuthally polarized beam in aturbulent atmosphere. *Opt. Express*, 16(11):7665–7673, May 2008. doi: 10.1364/OE.16.007665. URL http://www.opticsexpress.org/abstract.cfm?URI=oe-16-11-7665. 56

[50] Md Gaffar and Bosanta R Boruah. Generation of a boat-shaped beam due to a tightly focused comatically aberrated azimuthally polarized beam. *Journal of Optics*, 16(10):105709, 2014. URL http://stacks.iop.org/2040-8986/16/i=10/a=105709. 64

[51] Nándor Bokor and Nir Davidson. Generation of a hollow dark spherical spot by 4pi focusing of a radially polarized laguerre-gaussian beam. *Opt. Lett.*, 31 (2):149–151, Jan 2006. doi: 10.1364/OL.31.000149. URL http://ol.osa.org/abstract.cfm?URI=ol-31-2-149. 64, 65

TH-1501_10612103

[52] Stefan W. Hell and Jan Wichmann. Breaking the diffraction resolution limit by stimulated emission: stimulated-emission-depletion fluorescence microscopy. *Opt. Lett.*, 19(11):780–782, Jun 1994. doi: 10.1364/OL.19.000780. URL `http://ol.osa.org/abstract.cfm?URI=ol-19-11-780`. 64

[53] K. T. Gahagan and G. A. Swartzlander. Optical vortex trapping of particles. *Opt. Lett.*, 21(11):827–829, Jun 1996. doi: 10.1364/OL.21.000827. URL `http://ol.osa.org/abstract.cfm?URI=ol-21-11-827`. 65

[54] Nndor Bokor and Nir Davidson. A three dimensional dark focal spot uniformly surrounded by light. *Optics Communications*, 279(2):229 – 234, 2007. ISSN 0030-4018. doi: http://dx.doi.org/10.1016/j.optcom.2007.07.014. URL `http://www.sciencedirect.com/science/article/pii/S0030401807007171`. 65

[55] J Arlt and MJ Padgett. Generation of a beam with a dark focus surrounded by regions of higher intensity: the optical bottle beam. *Optics letters*, 25(4): 191–193, 2000. 65

[56] Yi Xue, Cuifang Kuang, Xiang Hao, Zhaotai Gu, and Xu Liu. A method for generating a three-dimensional dark spot using a radially polarized beam. *Journal of Optics*, 13(12):125704, 2011. URL `http://stacks.iop.org/2040-8986/13/i=12/a=125704`. 65

[57] Shuai Li, Cuifang Kuang, Xiang Hao, Zhaotai Gu, and Xu Liu. Generation of a 3d isotropic hollow focal spot for single-objective stimulated emission depletion microscopy. *Journal of Optics*, 14(8):085704, 2012. URL `http://stacks.iop.org/2040-8986/14/i=8/a=085704`. 65

[58] Steve C. Tidwell, Dennis H. Ford, and Wayne D. Kimura. Generating radially polarized beams interferometrically. *Appl. Opt.*, 29(15):2234–2239, May 1990. doi: 10.1364/AO.29.002234. URL `http://ao.osa.org/abstract.cfm?URI=ao-29-15-2234`. 67

[59] Polarization configurations with singular point formed by computer generated holograms. *Optics Communications*, 99(12):13 – 17, 1993. ISSN 0030-4018. doi: http://dx.doi.org/10.1016/0030-4018(93)90697-4. URL `http://www.sciencedirect.com/science/article/pii/0030401893906974`. 67

TH-1501_10612103

[60] M. Stalder and M. Schadt. Linearly polarized light with axial symmetry generated by liquid-crystal polarization converters. *Opt. Lett.*, 21(23):1948–1950, Dec 1996. doi: 10.1364/OL.21.001948. URL `http://ol.osa.org/abstract.cfm?URI=ol-21-23-1948`. 67

[61] Xi-Lin Wang, Jianping Ding, Wei-Jiang Ni, Cheng-Shan Guo, and Hui-Tian Wang. Generation of arbitrary vector beams with a spatial light modulator and a common path interferometric arrangement. *Opt. Lett.*, 32(24):3549–3551, Dec 2007. doi: 10.1364/OL.32.003549. URL `http://ol.osa.org/abstract.cfm?URI=ol-32-24-3549`. 67

[62] Ignacio Moreno, Jeffrey A. Davis, Travis M Hernandez, Don M. Cottrell, and David Sand. Complete polarization control of light from a liquid crystal spatial light modulator. *Opt. Express*, 20(1):364–376, Jan 2012. doi: 10.1364/OE.20.000364. URL `http://www.opticsexpress.org/abstract.cfm?URI=oe-20-1-364`. 67

[63] James H. Clegg and Mark A. A. Neil. Double pass, common path method for arbitrary polarization control using a ferroelectric liquid crystal spatial light modulator. *Opt. Lett.*, 38(7):1043–1045, Apr 2013. doi: 10.1364/OL.38.001043. URL `http://ol.osa.org/abstract.cfm?URI=ol-38-7-1043`. 67

[64] Christian Maurer, Alexander Jesacher, Severin Frhapter, Stefan Bernet, and Monika Ritsch-Marte. Tailoring of arbitrary optical vector beams. *New Journal of Physics*, 9(3):78, 2007. URL `http://stacks.iop.org/1367-2630/9/i=3/a=078`. 67

[65] Rainer J Beck, Jonathan P Parry, William N MacPherson, Andrew Waddie, Nick J Weston, Jonathan D Shephard, and Duncan P Hand. Application of cooled spatial light modulator for high power nanosecond laser micromachining. *Opt. Express*, 18(16):17059–17065, Aug 2010. doi: 10.1364/OE.18.017059. URL `http://www.opticsexpress.org/abstract.cfm?URI=oe-18-16-17059`. 67

[66] Ranjan Kalita, Md. Gaffar, and B. R. Boruah. Generation of arbitrary vector beams using a division of wavefront based setup. *Journal of Optics (IOP)*, Accepted for Publication, 2016. 67

[67] Fai Mok, Joseph Diep, Hua-Kuang Liu, and Demetri Psaltis. Real-time computer-generated hologram by means of liquid-crystal television spatial light

TH-1501_10612103

modulator. *Opt. Lett.*, 11(11):748–750, Nov 1986. doi: 10.1364/OL.11.000748. URL `http://ol.osa.org/abstract.cfm?URI=ol-11-11-748`. 67

[68] M. Reicherter, T. Haist, E. U. Wagemann, and H. J. Tiziani. Optical particle trapping with computer-generated holograms written on a liquid-crystal display. *Opt. Lett.*, 24(9):608–610, May 1999. doi: 10.1364/OL.24.000608. URL `http://ol.osa.org/abstract.cfm?URI=ol-24-9-608`. 67

[69] L.E Helseth. Optical vortices in focal regions. *Optics Communications*, 229 (16):85 – 91, 2004. ISSN 0030-4018. doi: http://dx.doi.org/10.1016/j.optcom.2003.10.043. URL `http://www.sciencedirect.com/science/article/pii/S0030401803021795`. 75

[70] Tingting Wang, Cuifang Kuang, Xiang Hao, and Xu Liu. Focusing properties of cylindrical vector vortex beams with high numerical aperture objective. *Optik - International Journal for Light and Electron Optics*, 124(21): 4762 – 4765, 2013. ISSN 0030-4026. doi: http://dx.doi.org/10.1016/j.ijleo.2013.01.070. URL `http://www.sciencedirect.com/science/article/pii/S0030402613002520`. 75

[71] Xiang Hao, Cuifang Kuang, Tingting Wang, and Xu Liu. Phase encoding for sharper focus of the azimuthally polarized beam. *Optics letters*, 35(23):3928–3930, 2010. 75

[72] Md Gaffar and BR Boruah. Aberration resilience of azimuthally polarized beam with a helical phase mask. *Proc. of SPIE*, pages 92721H–92721H, 2014. 76

[73] G Therese Anita, K Prabakaran, RC Sarasvathi, KB Rajesh, and TVS Pillai. Effect of spherical aberrations in tight focusing of higher order radially polarized beam. *Optik-International Journal for Light and Electron Optics*, 125(10):2378–2382, 2014. 91

[74] David P. Biss and Thomas G. Brown. Aberration modeling of cylindrical vector beams. *Frontiers in Optics*, page ThOO1, 2003. doi: 10.1364/FIO.2003.ThOO1. URL `http://www.opticsinfobase.org/abstract.cfm?URI=FiO-2003-ThOO1`. 91

[75] S N Khonina, A V Ustinov, and E A Pelevina. Analysis of wave aberration influence on reducing focal spot size in a high-aperture focusing system. *Journal*

TH-1501_10612103

of Optics, 13(9):095702, 2011. URL http://stacks.iop.org/2040-8986/13/i=9/a=095702. 91

[76] Chen Jiannong Yu Yongjiang. The effect of primary spherical aberration and aperture on focusing of radially polarized high-order vector bessel-gauss beams [j]. *Acta Optica Sinica*, 9:049, 2010. 91

[77] Md. Gaffar and B. R. Boruah. Effect of higher order aberrations on a radially polarized beam. *Proc. SPIE*, 9272:92720J–92720J–9, 2014. doi: 10.1117/12.2072057. URL http://dx.doi.org/10.1117/12.2072057. 91

[78] Arthur Ashkin. History of optical trapping and manipulation of small-neutral particle, atoms, and molecules. *Selected Topics in Quantum Electronics, IEEE Journal of*, 6(6):841–856, 2000. 107

[79] Ignacio Iglesias and Juan José Sáenz. Light spin forces in optical traps: comment on "trapping metallic rayleigh particles with radial polarization". *Opt. Express*, 20(3):2832–2834, Jan 2012. doi: 10.1364/OE.20.002832. URL http://www.opticsexpress.org/abstract.cfm?URI=oe-20-3-2832. 107

[80] Qiwen Zhan. Trapping metallic rayleigh particles with radial polarization: reply to comment. *Opt. Express*, 20(6):6058–6059, Mar 2012. doi: 10.1364/OE.20.006058. URL http://www.opticsexpress.org/abstract.cfm?URI=oe-20-6-6058. 107

[81] Steven Chu, JE Bjorkholm, A Ashkin, and Alex Cable. Experimental observation of optically trapped atoms. *Physical Review Letters*, 57(3):314, 1986. 107

[82] Keir C. Neuman and Steven M. Block. Optical trapping. *Review of Scientific Instruments*, 75(9), 2004. 107

[83] Qiwen Zhan. Trapping metallic rayleigh particles with radial polarization. *Optics express*, 12(15):3377–3382, 2004. 108

[84] Hikaru Kawauchi, Kazuhiro Yonezawa, Yuichi Kozawa, and Shunichi Sato. Calculation of optical trapping forces on a dielectric sphere in the ray optics regime produced by a radially polarized laser beam. *Optics letters*, 32(13):1839–1841, 2007. 108

TH-1501_10612103

[85] Qiwen Zhan. Radiation forces on a dielectric sphere produced by highly focused cylindrical vector beams. *Journal of Optics A: Pure and Applied Optics*, 5(3): 229, 2003. 108

[86] Lu Huang, Honglian Guo, Jiafang Li, Lin Ling, Baohua Feng, and Zhi-Yuan Li. Optical trapping of gold nanoparticles by cylindrical vector beam. *Optics letters*, 37(10):1694–1696, 2012. 108

[87] Yaoju Zhang and Yuxing Dai. Multifocal optical trapping using counter-propagating radially-polarized beams. *Optics Communications*, 285(5):725–730, 2012. 108

[88] Yiqiong Zhao, Qiwen Zhan, Yanli Zhang, and Yong-Ping Li. Creation of a three-dimensional optical chain for controllable particle delivery. *Opt. Lett.*, 30(8):848–850, Apr 2005. doi: 10.1364/OL.30.000848. URL `http://ol.osa.org/abstract.cfm?URI=ol-30-8-848`. 108

[89] Gaofeng Wu, Fei Wang, and Yangjian Cai. Generation and self-healing of a radially polarized bessel-gauss beam. *Physical Review A*, 89(4):043807, 2014. 108

[90] Kyoko Kitamura, Ting Ting Xu, and Susumu Noda. Investigation of electric field enhancement between metal blocks at the focused field generated by a radially polarized beam. *Optics express*, 21(26):32217–32224, 2013. 108

[91] Hao Chen, Santosh Tripathi, and Kimani C Toussaint. Demonstration of flat-top focusing under radial polarization illumination. *Optics letters*, 39(4):834–837, 2014. 108

[92] Colin J. R. Sheppard and Elijah Y. S. Yew. Performance parameters for focusing of radial polarization. *Opt. Lett.*, 33(5):497–499, Mar 2008. doi: 10.1364/OL.33.000497. URL `http://ol.osa.org/abstract.cfm?URI=ol-33-5-497`. 108

[93] M. Gaffar and Bosanta R. Boruah. Poynting vector profile of a tightly focused radially polarized beam in the presence of primary aberrations. *J. Opt. Soc. Am. A*, 32(4):660–668, Apr 2015. 108

[94] A. Boivin, J. Dow, and E. Wolf. Energy flow in the neighborhood of the focus of a coherent beam∗. *J. Opt. Soc. Am.*, 57(10):1171–1175, Oct 1967. doi:

TH-1501_10612103

10.1364/JOSA.57.001171. URL http://www.osapublishing.org/abstract.cfm?URI=josa-57-10-1171. 109

TH-1501_10612103

TH-1501_10612103

Publications

(a) Journals and Proceedings

1. Md. Gaffar, Ranjan Kalita and Bosanta. R. Boruah, Experimental demonstration of an aberrated azimuthally polarized beam, IJEAR, Vol. 2, No 2, (2015)

2. Md. Gaffar, Ranjan Kalita and Bosanta. R. Boruah, Experimental demonstration of a light beam with superior aberration resilience, (In Progress).

3. Md. Gaffar, Ranjan Kalita and Bosanta. R. Boruah, Experimental observation of the aberration effects on a radially polarized beam, (Communicated).

4. Ranjan kalita, Md. Gaffar and Bosanta. R. Boruah, Generation of arbitrary vector beams using a division of wavefront based setup, Journal of Optics (IOP), 18(7) 075604 (2016).

5. Md. Gaffar and Bosanta. R. Boruah, Poynting vector profile of tightly focused radially polarized beam in the presence of primary aberrations, JOSA A. Vol. 32, No.4, 660-668 (2015).

6. Md. Gaffar and Bosanta. R. Boruah, Generation of a boat- shaped beam due to a tightly focused comatically aberrated azimuthally polarized beam, J. Opt. 16 105709 (2014).

7. Md. Gaffar and Bosanta. R. Boruah, Effect of higher order aberrations on a radially polarized beam, Proc. SPIE. Vol. 9272, 92720J-1(2014).

8. Md. Gaffar and Bosanta. R. Boruah, Aberration resilience of an azimuthally polarized beam with a helical phase mask, Proc. SPIE. Vol. 9272, 92721H-1 (2014).

TH-1501_10612103

(b) Conference Presentation:

1. Effect of aberrations on an azimuthally polarized beam and a circularly polarized vortex beam: A comparative study, ICOP XXXIX symposium of OSI, February 20-22, 2015, University of Calcutta, Kolkata.

2. Effect of primary aberration on focal volume properties of a radially polarized beam, ICOL XXXVIII symposium of OSI, 5-8 march, 2014, IRDE, Dehradun, Uttarakhand.

3. Generation of hollow laser beam from an azimuthally polarized beam profile, XXXVII National symposium of optical society of India, 23-35 Jan 2013, Pondicherry University, Puducherry.

4. Generation of modified normal beam laser from an azimuthally polarized beam, 1st IITG student's chapter workshop on optics, IIT Guwahati, 15-17 November 2012.

5. Generation of boat - shaped beam using a division of wavefront based setup, TE-QIP symposium to celebrate IYL, IIT Guwahati, 31 October 2015.

6. Poynting vector profile of a tightly focused radially polarized beam in the presence of higher order aberrations, South Asian workshop on optics and photonics, IIT Guwahati, 17-18 November 2015.

(c) School/Seminar/Workshop attended:

1. Computational Techniques in Physics, QIP short term course, IIT Guwahati, 1-6 Augast, 2011.

2. National workshop on Labview based graphical system design, Gauhati University, 24 28 September 2012.

3. IEEE Matlab workshop, IIT Guawahti, 2013 (22-23 rd June).

***

TH-1501_10612103